Theoretical Studies of Proton-Coupled Electron Transfer Reactions via the Mixed Quantum-Classical Liouville Approach

by
Farnaz A. Shakib

A thesis submitted in partial fulfillment of the requirements for the degree of

Doctor of Philosophy

Department of Chemistry
University of Alberta

Abstract

The nonadiabatic dynamics of model proton-coupled electron transfer (PCET) reactions were investigated for the first time using a surface-hopping algorithm based on the solution of the mixed quantum-classical Liouville (MQCL) equation. This method provides a rigorous treatment of quantum decoherence effects in the dynamics of mixed quantum-classical systems, which is lacking in Tully's fewest switches surface hopping (FSSH) approach commonly used for simulating PCET reactions. Within the MQCL approach, the transferring proton and electron are treated quantum mechanically while the remainder of the system, including the donor, acceptor, and solvent, is treated classically. The classical degrees of freedom (DOF) are evolved on both single adiabatic potential energy surfaces (PESs) and on coherently coupled pairs of adiabatic PESs, while in FSSH they are evolved only on single adiabatic PESs. To demonstrate the applicability of MQCL approach to the study of PCET, we focused on a reduced model that had been previously studied using FSSH. This model is comprised of three DOF, including a proton, an electron, and a collective solvent coordinate. The proton and electron are allowed to transfer in one dimension between two point charges, representing the donor and the acceptor, which are positioned at a fixed distance from each other. Both concerted and sequential [either proton transfer before electron transfer (i.e., PT-ET) or electron transfer before proton transfer (i.e., ET-PT)] PCET reactions were studied within the context of this model. We studied these mechanisms in detail under various subsystem-bath coupling conditions and gained insights into the dynamical principles underlying these reactions. Notably, an examination of the trajectories which successfully undergo PCET (i.e., both the proton and electron, initially near the donor, transfer to the acceptor) reveals that the system spends the majority of its time on the mean of two coherently coupled adiabatic PESs. While on this mean surface, the classical DOF evolve differently than

on the other surfaces and an observable of interests acquires a phase factor. Fluctuations of the classical coordinates can cause this phase factor to oscillate in time differently for each trajectory and, as a result, averaging over an ensemble of trajectories can lead to destructive interference when calculating an expectation value of an observable. In this way, the MQCL approach is able to incorporate decoherence, which is not captured in the FSSH approach. Due to this fundamental difference between the two methods, the percentages of successful PCET reactions obtained via MQCL drastically differ from those obtained via FSSH.

To gain insight into the differences between the MQCL and FSSH approaches for calculating PCET observables, we calculated the time-dependent populations of the ground, first-excited, and second-excited adiabatic states for the ET-PT mechanism in the same PCET model and compared them to both the exact quantum and FSSH results. We found that the MQCL population profiles show a significant improvement over the FSSH ones, and are in good agreement with the exact quantum results. All of the mean PESs were shown to play a direct role in the dynamics of the state populations. Interestingly, our results showed that the population transfer to the second-excited state can be mediated by the dynamics on the mean of the ground and second-excited state PESs, via a sequence of nonadiabatic transitions that bypasses the first-excited state PES altogether. This is made possible by nonadiabatic transitions between different mean surfaces, which is the manifestation of coherence transfer in MQCL dynamics. We also investigated the effect of the strength of the coupling between the proton/electron and the collective solvent coordinate on the state population dynamics. Drastic changes in the population dynamics are observed, which can be understood in terms of the changes in the PESs and the nonadiabatic couplings. In addition, we investigated the state population dynamics in the PT-ET and concerted versions of the model. The PT-ET results revealed the participation of all of the mean surfaces, albeit in different proportions

compared to the ET-PT reaction, while the concerted results revealed that the mean of the ground and first-excited state PESs only plays a role.

We finally present a derivation of a novel mixed quantum-classical formula for calculating PCET rate constants that starts from the quantum mechanical expression for the time integral of the flux-flux correlation function. The resulting time-dependent rate coefficient has a dynamical part involving MQCL time evolution of the product species operator and an equilibrium part. This formula is general, not requiring any prior assumptions about the parameters of the system. Furthermore, since MQCL dynamics is used to evolve the product species operator, this approach treats decoherence on a more solid footing than the FSSH-based methods. The applicability of this formula is demonstrated on an extended version of the previously studied PCET model, where now the collective solvent coordinate is coupled to a harmonic oscillator bath. Our result for the rate constant is found to be in good agreement with the numerically exact result obtained via the quasi-adiabatic path integral method.

Preface

Chapter 2 of this thesis contains the following published article:

Shakib, F. A. and Hanna, G. An analysis of model proton-coupled electron transfer reactions via the mixed quantum-classical Liouville approach, *J. Chem. Phys.*, **2014**, *141*, 044122-1044122-12.

Chapter 3 of this thesis contains the following published article:

Shakib, F. A. and Hanna, G. New insights into the nonadiabatic state population dynamics of model proton-coupled electron transfer reactions from the mixed quantum-classical Liouville approach, *J. Chem. Phys.*, **2016**, *144*, 024110-1024110-11.

My contribution to these articles included aiding in the selection of an appropriate PCET model, writing computer codes for simulating the dynamics of this model and analyzing data, running the simulations, preparing the draft of the manuscript, and helping my supervisor in bringing the manuscripts to their final forms.

Acknowledgements

I would like to thank the Alberta Innovates Future Technology (AIFT) and Natural Sciences and Engineering Research Council of Canada (NSERC) for financial support over the years. I would also like to thank WestGrid and Compute/Calcul Canada for access to their computational resources over the years.

I am greatly indebted to Prof. Gabriel Hanna for all his time, energy, and patience during the course of my PhD. His thoughtful guidance over the years will always be appreciated. I would also like to thank the members of the Theoretical and Computational Chemistry group in our department for their friendly support and encouragement.

I am also grateful to the members of my examination committee (Profs. Mariusz Klobukowski, Yunji Xu, Frederick West, and Juli Gibbs-Davis) for taking the time to read my thesis and providing thoughtful comments.

Finally, I am grateful to Prof. Thomas F. Miller from the California Institute of Technology for agreeing to be the external referee of this thesis and providing constructive comments/suggestions.

To my everlasting ray of hope, "Mohammad"

Abbreviations

CW	classical Wigner
DOF	degree of freedom
ET	electron transfer
ET-PT	electron transfer followed by proton transfer
FSSH	fewest switches surface hopping
GFSH	global flux surface hopping
HAT	hydrogen-atom transfer
MD	molecular dynamics
MQCD	mixed quantum-classical dynamics
MQCL	mixed quantum-classical Liouville
MS-EPT	multi site electron-proton transfer
OEC	oxygen evolving complex
PCET	proton-coupled electron transfer
PES	potential energy surface
PT	proton transfer
PT-ET	proton transfer followed by electron transfer
QCLE	quantum-classical Liouville equation
RPMD	ring-polymer molecular dynamics
SQUASH	second-quantized surface hopping
SSTP	sequential short-time propagation

Contents

List of Figures

List of Tables

Chapter 1

Introduction

1.1 PCET in biology and chemistry

Proton-coupled electron transfer (PCET), which is a proton transfer coupled to an electron transfer, is at the heart of important biological processes such as photosynthesis, respiration, and DNA repair [3]. To illustrate the role of PCET, let us consider photosynthesis as an example. Photosynthesis is the process by which the solar energy is converted into the chemical energy stored in chemical bonds of carbohydrates. This solar energy is used to split off water's hydrogen from oxygen. Then, hydrogen is combined with carbon dioxide (absorbed from air or water) to form glucose and release oxygen:

$$6\,CO_2 + 6\,H_2O \longrightarrow C_6H_{12}O_6 + 6\,O_2 \tag{1.1}$$

A deep understanding of this ubiquitous reaction may lead to a clean and sustainable solution to the increasing worldwide demand for energy. Thus, we briefly discuss this reaction in more detail.

Photosynthesis begins when light is absorbed by proteins called photosynthetic reaction centers found inside chloroplasts (in green plants). The photosynthetic complex, Photosystem II, is the first protein complex involved in solar energy conversion. It is comprised of at least 99 cofactors: 35 chlorophyll a, 12 beta-carotene, two pheophytin, three plastoquinone, two heme, bicarbonate, 25 lipids, and seven n-dodecyl-beta-D-maltoside detergent molecules,

the six components of the Mn_4Ca cluster (including chloride ion), and one Fe^{2+} and two putative Ca^{2+} ion per monomer [4]. The tetra-manganese cluster is an oxo-bridged cluster (Mn_4O_5Ca) called the oxygen-evolving complex (OEC) [5–9]. This name arises from the fact that it catalyses the splitting of water molecules to produce oxygen when driven by the absorption of four photons (Eq. 1.2, Fig. 1.1):

$$2\,H_2O + 4\,\text{photons} \longrightarrow 4\,H^+ + 4\,e^- + O_2 \tag{1.2}$$

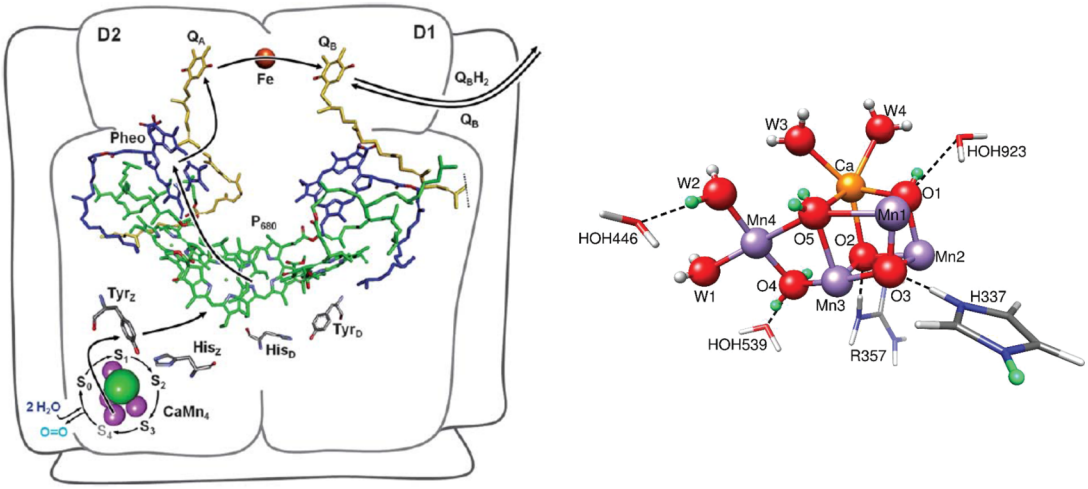

FIGURE 1.1: (a) Different components of Photosystem II, (b) the optimized structure of OEC, reprinted (adapted) with permission from Ref. 1. Copyright (2015) American Chemical Society.

The overall function of OEC is accomplished by cycling through five oxidation states, known as the S_0–S_4 states of the Kok cycle (Fig. 1.2). For each step of the cycle, an electron is transferred from the cluster to a nearby tyrosine (Figs. 1.1 and 1.2). When the cluster reaches the highly reactive S_4 state, oxygen is released and the system returns to the S_0 state. As can be seen from Fig. 1.2, water oxidation relies on a sequence of proton and electron transfer steps in which the release of protons is essential to maintain a redox potential low enough for the next oxidation event to occur.

It is not a stretch to say that photosynthesis depends on PCET, since the Kok cycle involves the transferring of 24 e^- and 24 H^+ driven by 48 photons. This fundamental reaction leads to $\sim 10^{11}$ tons of carbon being stored annually, which represents a massive amount of stored

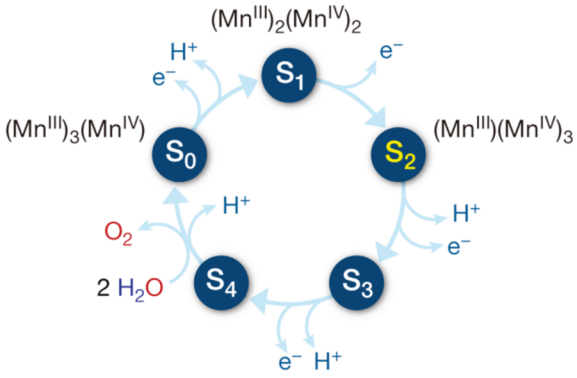

FIGURE 1.2: The Kok cycle representing the four oxidation states of OEC, reprinted (adapted) with permission from Ref. 2. Copyright (2015) American Chemical Society.

energy ($\sim 10^{18}$ kJ), Eq. 1.3 and 1.4 [3].

$$6\,CO_2 + 6\,H_2O + 24\,h\nu -> C_6H_{12}O_6 + 6\,O_2$$
$$\Delta G^\circ = 29.1 \text{ eV} \tag{1.3}$$

$$C_6H_{12}O_6 + 6\,O_2 + 38\,ADP + 38\,P_i \longrightarrow 6\,H_2O + 6\,CO_2 + 38\,ATP$$
$$\Delta G^\circ = 12 \text{ eV} \tag{1.4}$$

where P_i denotes an inorganic phosphate. The half reactions of photosynthesis , i.e. oxidation of water and reduction of hydrogen, involve multi-electron/multi-proton PCETs, whose complex mechanisms are comprised of different elementary steps, which are introduced in the next section.

1.2 Elementary steps of PCET

Different elementary steps can contribute to PCET reactions including electron transfer (ET), proton transfer (PT), concerted electron-proton transfer (EPT), multi-site electron-proton transfer (MS-EPT), hydrogen-atom transfer (HAT), and simultaneous transfer of $2\,e^-/1\,H^+$ (i.e., hydride transfer). In general, PCET reactions can occur via more than one multistep mechanism since there may be a competition between mechanisms depending on the temperature, pH, etc. PT and ET, for example, can combine together to form sequential

PCET mechanisms, where either ET precedes PT (i.e., ET-PT) or PT precedes ET (i.e, PT-ET).

Among these steps, normally EPT is the one that follows reaction pathways that avoid high-energy intermediates. One should know that EPT is different from HAT, though in some cases this difference can be very subtle. In EPT, electrons and protons transfer from different orbitals on the donor to different orbitals on the acceptor. An example of EPT is illustrated in step 2 of the comproportionation reaction in Fig. 1.3. In this step, a concerted transfer occurs with the electron transferring from a metal-based dπ orbital at $Ru^{II}-OH_2^{2+}$ to a dπ acceptor orbital at $Ru^{IV}=O^{2+}$. Proton transfer occurs from a σ(O−H) orbital at Ru(II) to an O-based lone-pair orbital at $Ru^{IV}=O^{2+}$ [10, 11].

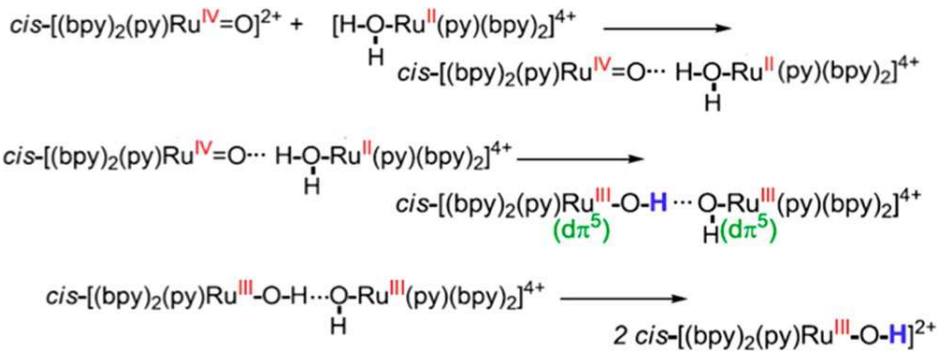

FIGURE 1.3: An example of a concerted electron-proton transfer (EPT), reprinted (adapted) with permission from Ref. 3. Copyright (2015) American Chemical Society.

In EPT, the e^-/H^+ donor orbitals and e^-/H^+ acceptor orbitals must interact electronically, enabling simultaneous transfer. Normally formation of a hydrogen-bond is the first step for making such an interaction possible, e.g. step 1 in Fig. 1.3. At last, the simultaneous transfer of an electron and proton occurs if this motion is faster than the periods of the coupled vibrations (tens of femtoseconds) and solvent modes (∼1 ps) [12].

On the other hand, in HAT, both the transferring electron and proton come from the same orbital in one of the reactants. Figure 1.4 represents an example of HAT in the oxidation of benzaldeyde by $Ru^{IV}(bpy)_2(py)(O)^{2+}$. The transferring electron and proton both come from the same σ(C−H) bond of the benzaldehyde.

MS-EPT refers to either transferring of an electron and proton from a donor species to different acceptors or from different donors to one acceptor species. As an example, one

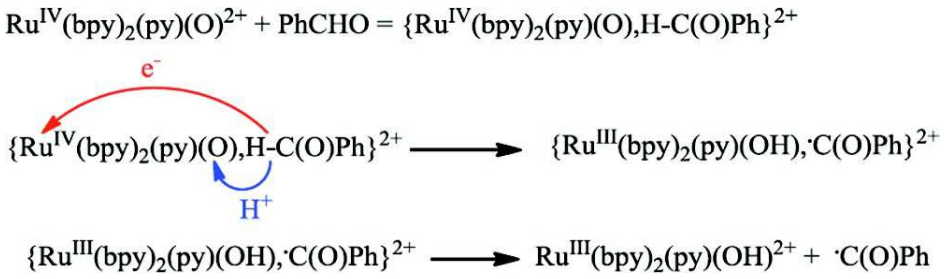

FIGURE 1.4: An example of hydrogen atom transfer, reprinted (adapted) with permission from Ref. 3. Copyright (2015) American Chemical Society.

can refer to the quenching of triplet C_{60} and tetracene fluorescence by phenols which is strongly enhanced through addition of pyridines [13]. Based on kinetic measurements and independent spectroscopic data, the quenching is the result of a trimolecular transition state in which an electron transfer occurs from the phenol to the excited molecule while a proton transfers from the phenolic OH to the pyridine nitrogen.

It should be noted that the nomenclature used to describe concerted electron-proton transfer, i.e. EPT, has not been standardized and other terms are being used in the literature to describe the same elementary step, including concerted proton-electron transfer (CPET) [14], electron transfer proton transfer (ET-PT) [15], concerted electron-proton transfer (CEP) [16], and concerted proton-coupled electron transfer (concerted PCET) [17]. The last term is what we use in this thesis to differentiate the concerted mechanism of the transfer of a proton and electron from the sequential mechanisms. A schematic representation of the reactions studied in this thesis are depicted in Fig. 1.5.

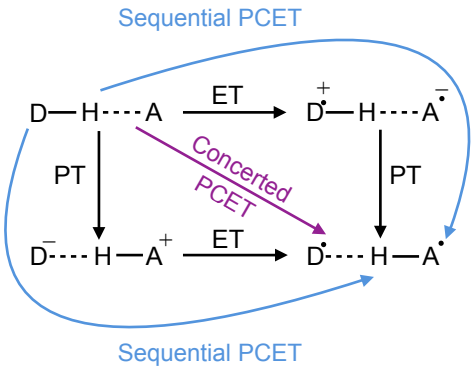

FIGURE 1.5: A schematic representation of concerted and sequential PCET reactions. D represents the donor and A represents the acceptor species.

1.3 Theoretical challenges

Due to the importance of PCET in chemical and biological reactions, it is not surprising that this phenomenon has been the subject of numerous experimental [3, 14, 18–23] and theoretical [18, 24–30] studies over the past two decades. A deep understanding of the mechanisms of PCET reactions, however, is complicated by both the quantum mechanical nature of the transferring protons and electrons and the size and complexity of the environments in which they occur. Ideally, a full quantum dynamical treatment should be used to study these reactions, but the large number of degrees of freedom in the surrounding environment renders such a treatment impossible. To circumvent this problem, simplified models of complex systems may be studied to gain qualitative insights into the PCET mechanisms and/or mixed quantum-classical schemes, which treat the transferring protons and electrons quantum mechanically and the environmental degrees of freedom classically, may be used to gain quantitative information about PCET reaction rates.

Another theoretical challenge in the study of PCET reactions is related to the different timescales of motions encountered in these systems. There are three distinct timescales in PCET. Electrons move on the fastest timescale, protons move on an intermediate timescale, and the solvent and heavy atoms of the solute move on the slowest timescale[31]. Hence, it is convenient to treat the transferring electrons and protons quantum mechanically, to include effects such as zero point energy and tunnelling, while the heavy particles may be treated classically. If a distinct separation of timescales exists, then one could invoke two adiabatic approximations for PCET, namely that the electrons respond instantaneously to the proton and solvent motion and, likewise, the protons respond instantaneously to the solvent motion. However, this is not always a valid approximation for PCET reactions since electron transfer reactions in solution are often nonadiabatic with respect to the solvent motion [32–34]. When the electrons do not respond instantaneously to the solvent motion then most likely they will not respond instantaneously to the proton motion either, which is typically faster than the solvent motion. A similar behaviour is expected for proton motion compared to the solvent motion. This is due to the presence of long hydrogen bonds, which results in weak couplings between electron donors and acceptors. Thus, an accurate mixed quantum-classical description of PCET reactions should take all the nonadiabatic couplings in the system into account.

1.4 Mixed quantum-classical dynamics (MQCD)

Mixed quantum-classical dynamics (MQCD) approaches treat a few degrees of freedom (DOF) in a subsystem of interest quantum mechanically, while the remaining DOFs in the environment are treated classically. The last few decades have witnessed the emergence of various mixed quantum-classical approaches for simulating nonadiabatic dynamics of chemical and biological systems. The most well-known of these methods is Fewest Switches Surface Hopping (FSSH), introduced by Tully and Preston in 1971 [35, 36] and later improved in the early 90s [37, 38]. In this approach, an ensemble of classical trajectories is evolved on single adiabatic potential energy surfaces with stochastic nonadiabatic transitions between surfaces. Over the years, improved versions of FSSH have been introduced, including second-quantized surface hopping (SQUASH) [39] and global flux surface hopping (GFSH) [40, 41] to name a few. Other MQCD approaches include mixed quantum-classical Liouville (MQCL) dynamics [56, 58] and mixed quantum-classical Bohmian dynamics [59–61].

Semi-classical approaches have also been introduced, which treat the subsystem and environmental DOF on an equal footing. Such approximate schemes include the classical Wigner (CW) approximation [42–44], centroid molecular dynamics [45], and ring-polymer molecular dynamics (RPMD) [46].

Quantum mechanics/molecular mechanics (QM/MM) [47–51] has also proved useful in simulating large and complex systems. It provides a feasible way for addressing the electronic structure problem, while the aforementioned methods address the molecular dynamics problem.

1.4.0.1 Fewest switches surface hopping (FSSH)

Tully's FSSH is one of the most widely used mixed quantum-classical methods for simulating the nonadiabatic dynamics of quantum processes in condensed phase systems. Compared to other MQCD methods, it is more computationally efficient, making simulations of large systems feasible. It is also conceptually simple, representing a quantum wave packet in terms of an ensemble of independent trajectories. The multiple steps in an FSSH simulation can be summarized as follows:

1. The time-independent Schrödinger equation, $\hat{h}|\alpha;Q\rangle = E_\alpha(Q)|\alpha;Q\rangle$, for the quantum subsystem is solved for a fixed configuration of the classical DOF, Q, to obtain the adiabatic energies, $E_\alpha(Q)$, and the corresponding adiabatic states, $|\alpha;Q\rangle$.

2. A time-dependent wave function is defined as $|\Phi(t)\rangle = \sum_k C_k(t)|\alpha;Q\rangle$, where $C_k(t)$ are complex-valued expansion coefficients.

3. Substitute this wavefunction into the time-dependent Schrödinger equation to obtain

$$i\hbar\dot{C}_k = \sum_j C_j(V_{kj} - i\hbar\dot{Q}\cdot d_{kj}) \tag{1.5}$$

where the coupling potential between two states is given by

$$V_{kj} = \langle\alpha_k;Q|\hat{h}(Q)|\alpha_j;Q\rangle \tag{1.6}$$

and the nonadiabatic coupling vector between the two states is defined as

$$d_{kj}(Q) = \langle\alpha_k;Q|\nabla_Q|\alpha_j;Q\rangle \tag{1.7}$$

Equation 1.5 is integrated numerically as the trajectory of the classical DOF is propagated on the single state k in order to obtain the amplitudes C_k of each quantum mechanical state at a given time t.

4. Hellmann-Feynman forces, the forces on each classical DOF due to the quantum subsystem, are calculated as follows

$$F_{\alpha_k}(Q) \quad = \quad -\langle\alpha_k;Q|\frac{\partial\hat{h}}{\partial Q}|\alpha_k;Q\rangle \tag{1.8}$$

These forces along with the remaining classical forces are used to update the positions and velocities of the classical DOF via Newton's equations of motion.

5. The "fewest switches" algorithm apportions trajectories among states according to the quantum probabilities $|C_k(t)|^2$ with the minimum required number of quantum transitions. According to this algorithm, the probability of switching from the current state k to all other

states j during the time interval between t and $t + \Delta$ is

$$g_{kj} = \frac{b_{jk}(t + \Delta)\Delta}{a_{kk}(t + \Delta)} \tag{1.9}$$

where $a_{kk} = C_k C_k^*$ is the population of state k and $b_{jk} = 2\hbar^{-1}\mathrm{Im}(\alpha_{jk}^* V_{jk}) - 2\mathrm{Re}(\alpha_{jk}^* \dot{Q} \cdot d_{kj})$. Whether or not a switch to any state j occurs is determined by comparing g_{kj} to a randomly generated number between 0 and 1. The transition occurs, or is accepted, if the probability of transition is greater than the random number. This switching procedure ensures that, for a large ensemble of trajectories, the fraction of trajectories assigned to any state k at any time t will equal the quantum probability $|C_k(t)|^2$.

6. If the transition is accepted, then the velocities of the classical DOFs are shifted to conserve energy. If the transition is rejected, then the classical DOFs continue to evolve on the adiabatic PESs corresponding to the current state.

7. Steps 1 to 6 are repeated for each time step of the MD simulation.

FSSH has been widely used to study the dynamics and rates of charge transfer reactions including PCET [28, 62–65]; however, there have been some issues with the accuracy of the method [66–69]. To represent a wave packet, one needs to satisfy conservation of the total energy of the ensemble of the trajectories, while allowing energy exchange between individual trajectories. Although each trajectory conserves energy in FSSH, the decoupled classical trajectories do not exchange energy and hence cannot properly represent a quantum-mechanical wave packet. As a result, FSSH suffers from neglecting decoherence which is the collapse of the quantum superposition when coupled to a classical environment. FSSH evolves the wave function coherently and although there were attempts to add corrections to account for decoherence, they were ad hoc in nature [70, 71]. It has been shown that in the case of the spin-boson model, FSSH yields time-reversible dynamics only with zero friction and for certain initial energies. However, under other conditions, the value of the electronic wave function is not periodic and FSSH is unable to recover the correct Marcus' golden rule scaling unless decoherence added to the algorithm [72, 73].

1.4.0.2 Mixed quantum-classical Liouville (MQCL) approach

The mixed quantum-classical Liouville (MQCL) surface-hopping algorithm is based on the numerical solution of the quantum-classical Liouville equation (QCLE) [74–85], which rigorously accounts for quantum coherence/decoherence effects in mixed quantum-classical dynamics. In the MQCL approach, the classical DOF are evolved either on single adiabatic potential energy surfaces or on the mean of two adiabatic surfaces corresponding to two coherently coupled states [83, 84], as opposed to just on single adiabatic surfaces as in FSSH. To illustrate the differences between these two approaches for calculating condensed phase charge transfer rates, it has been found [87] that the MQCL approach yields a proton transfer rate constant for the Azzouz-Borgis model [86] of a proton transfer reaction in a phenol trimethylamine complex dissolved in CH_3Cl that is approximately twice as large as that given by FSSH [88]. Owing to its more rigorous treatment of coherence/decoherence effects, the MQCL approach is expected to yield more accurate rate constants for condensed phase PCET reactions and may also shed new light on their underlying mechanisms.

As in all MQCD approaches, one considers a quantum subsystem that is coupled to a classical environment, whose Hamiltonian is given by

$$\begin{aligned} \hat{H}\left(Q,P\right) &= \frac{P^2}{2M} + V_e(Q) + \frac{\hat{p}^2}{2m} + \hat{V}_s(\hat{q}) + \hat{V}_c(\hat{q},Q) \\ &\equiv H_e(Q,P) + \hat{h}_s(\hat{q},\hat{p}) + \hat{V}_c(\hat{q},Q) \\ &\equiv H_e(Q,P) + \hat{h}(Q), \end{aligned} \tag{1.10}$$

where m, $\hat{q}$, and $\hat{p}$ are the vectors of masses, positions, and momenta of the n quantum DOF, respectively; M, Q, and P are the vectors of masses, positions, and momenta of the N classical DOF, respectively; $H_e = \frac{P^2}{2M} + V_e$ and $\hat{h}_s = \frac{\hat{p}^2}{2m} + \hat{V}_s$ are the environment and subsystem Hamiltonians, respectively; $\hat{V}_c$ is the subystem-environment coupling potential energy and $\hat{h} = \hat{h}_s + \hat{V}_c$ [throughout this text, operators are capped (e.g., $\hat{A}$)]. The state of this mixed quantum-classical system can be represented in terms of the partial Wigner transform [89] of the density operator, $\hat{\rho}$, over the environmental DOF:

$$\hat{\rho}_W(X,t) = \left(\frac{1}{2\pi\hbar}\right)^N \int dZ e^{iP\cdot Z/\hbar} \langle Q - Z/2|\hat{\rho}(t)|Q + Z/2\rangle, \tag{1.11}$$

where $X = (Q, P)$. When $m/M \ll 1$, the dynamics of $\hat{\rho}_W(X,t)$ can be accurately described by the QCLE [58, 79]:

$$\begin{aligned}\frac{\partial}{\partial t}\hat{\rho}_W(X,t) &= -\frac{i}{\hbar}\left[\hat{H}_W\left(X,t\right),\hat{\rho}_W\left(X,t\right)\right] \\ &\quad +\frac{1}{2}\left(\left\{\hat{H}_W\left(X,t\right),\hat{\rho}_W\left(X,t\right)\right\}-\left\{\hat{\rho}_W\left(X,t\right),\hat{H}_W\left(X,t\right)\right\}\right), \end{aligned} \tag{1.12}$$

where $[\cdots]$ is the commutator and the Poisson bracket $\{\cdots\}$ is defined as

$$\left\{\hat{A}_W\left(X,t\right),\hat{B}_W\left(X,t\right)\right\} = \hat{A}_W\left(X,t\right)\left(\overleftarrow{\nabla}_P\overrightarrow{\nabla}_Q-\overleftarrow{\nabla}_Q\overrightarrow{\nabla}_P\right)\hat{B}_W\left(X,t\right). \tag{1.13}$$

Here, $\overrightarrow{\nabla}_{Q/P}$ and $\overleftarrow{\nabla}_{Q/P}$ are gradient operators with respect to Q/P which act on the term to the right and left of them, respectively.

The quantum subsystem may be represented in terms of an adiabatic basis, $|\alpha;Q\rangle$, which are the solutions of $\hat{h}(Q)|\alpha;Q\rangle = E_\alpha(Q)|\alpha;Q\rangle$. In this representation, the QCLE is given by [79]

$$\frac{\partial\rho_W^{\alpha\alpha'}(X,t)}{\partial t} = -i\sum_{\beta\beta'}\mathcal{L}_{\alpha\alpha',\beta\beta'}\rho_W^{\beta\beta'}(X,t), \tag{1.14}$$

where the evolution operator is defined as

$$i\mathcal{L}_{\alpha\alpha',\beta\beta'} \equiv (i\omega_{\alpha\alpha'}+iL_{\alpha\alpha'})\delta_{\alpha\beta}\delta_{\alpha'\beta'}-\mathcal{J}_{\alpha\alpha',\beta\beta'}. \tag{1.15}$$

In the above equation, the classical Liouville operator, $iL_{\alpha\alpha'}$, is given by

$$iL_{\alpha\alpha'} = \frac{P}{M}\cdot\frac{\partial}{\partial Q}+\frac{1}{2}\left(F_W^{\alpha}+F_W^{\alpha'}\right)\cdot\frac{\partial}{\partial P}. \tag{1.16}$$

When the quantum state indices are equal (i.e., $\alpha = \alpha'$), the classical evolution is carried out subject to the Hellmann-Feynman forces, $F_W^\alpha = -\langle\alpha;Q|\frac{\partial\hat{V}_c(\hat{q},Q)}{\partial Q}|\alpha;Q\rangle$, on a single adiabatic surface $E_\alpha(Q)$. However, when the quantum state indices are different (i.e., $\alpha \neq \alpha'$), the classical evolution is carried out on the mean of two adiabatic surfaces, $[E_\alpha(Q)+E'_\alpha(Q)]/2$, accompanied by quantum phase oscillations of frequency $\omega_{\alpha\alpha'} = (E_\alpha - E_{\alpha'})/\hbar$. The term responsible for nonadiabatic transitions and the associated changes in the bath momentum

(to conserve energy) is given by

$$\begin{aligned}\mathcal{J}_{\alpha\alpha',\beta\beta'}(t) &= -\frac{P}{M}\cdot d_{\alpha\beta}\left(1+\frac{1}{2}S_{\alpha\beta}\cdot\frac{\partial}{\partial P}\right)\delta_{\alpha'\beta'} \\ &- \frac{P}{M}\cdot d^*_{\alpha'\beta'}\left(1+\frac{1}{2}S^*_{\alpha'\beta'}\cdot\frac{\partial}{\partial P}\right)\delta_{\alpha\beta},\end{aligned} \tag{1.17}$$

where $S_{\alpha\beta} = F^{\alpha}_{W}\delta_{\alpha\beta} - F^{\alpha\beta}_{W}(\frac{P}{M}\cdot d_{\alpha\beta})^{-1} = E_{\alpha\beta}d_{\alpha\beta}(\frac{P}{M}\cdot d_{\alpha\beta})^{-1}$, $d_{\alpha\beta} = \langle\alpha;Q|\frac{\partial}{\partial Q}|\beta;Q\rangle$ is the nonadiabatic coupling vector matrix element, and $F^{\alpha\beta}_{W}$ is the off-diagonal matrix element of the force.

Formally, the solution of the QCLE for $\rho^{\alpha\alpha'}_{W}(X,t)$ can be written as

$$\rho^{\alpha\alpha'}_{W}(X,t) = \sum_{\beta\beta'}\left(e^{-i\hat{\mathcal{L}}t}\right)_{\alpha\alpha',\beta\beta'}\rho^{\beta\beta'}_{W}(X)\,. \tag{1.18}$$

A numerical solution may be obtained using the sequential short-time propagation (SSTP) algorithm [83], which is based on a decomposition of the propagator into short-time segments. Dividing the time interval t into S segments such that the j^{th} segment has length $\Delta t_j = t_j - t_{j-1} = \Delta t$ (where Δt is the time step), gives

$$\rho^{\alpha_0\alpha'_0}_{W}(X,t) = \sum_{(\alpha_1\alpha'_1)\ldots(\alpha_S\alpha'_S)}\Big[\prod_{j=1}^{S}(e^{-i\hat{\mathcal{L}}\Delta t_j})_{\alpha_{j-1}\alpha'_{j-1},\alpha_j\alpha'_j}\Big]\rho^{\alpha_S\alpha'_S}_{W}(X), \tag{1.19}$$

where the short-time propagator is approximated by

$$\begin{aligned}(e^{-i\hat{\mathcal{L}}\Delta t_j})_{\alpha_{j-1}\alpha'_{j-1},\alpha_j\alpha'_j} &\approx \mathcal{W}_{\alpha_{j-1}\alpha'_{j-1}}(t_{j-1},t_j)e^{-iL_{\alpha_{j-1}\alpha'_{j-1}}\Delta t_j} \\ &\times \left(\delta_{\alpha_{j-1}\alpha_j}\delta_{\alpha'_{j-1}\alpha'_j} + \Delta t\mathcal{J}_{\alpha_{j-1}\alpha'_{j-1},\alpha_j\alpha'_j}\right)\end{aligned} \tag{1.20}$$

and $\mathcal{W}_{\alpha_{j-1}\alpha'_{j-1}}(t_{j-1},t_j) = e^{-i\omega_{\alpha_{j-1}\alpha'_{j-1}}\Delta t_j}$ is the phase factor for that segment. In the SSTP algorithm, Monte Carlo sampling is used to evaluate the multi-dimensional sums over quantum indices in Equation 1.19. A typical surface-hopping trajectory generated by this algorithm is composed of segments in which the classical DOF evolve on a single adiabatic surface (when $\alpha_j = \alpha'_j$) and on the mean of two surfaces (when $\alpha_j \neq \alpha'_j$), as governed by the first term in Equation 1.20. These segments are interrupted by nonadiabatic transitions, as governed by the second term in Equation 1.20, which cause the classical DOF to hop to a new surface (or mean surface), followed by evolution on this surface. The details for

propagating a system starting from an initial condition $\{X, \alpha_0, \alpha_0'\}$ via the SSTP algorithm are provided in Refs. 83 and 84.

1.4.0.3 FSSH vs. MQCL

In this section, we point out the advantages of the MQCL approach over FSSH:

1) FSSH was not derived from the quantum Liouville equation, but instead has been justified on empirical grounds. On the other hand, the MQCL equation was rigorously derived from the quantum Liouville equation in the limit of $\frac{m}{M} << 1$, where m and M are the masses of quantum and classical DOFs, respectively.

2) The time evolution of FSSH classical trajectories occurs on single adiabatic potential energy surfaces (PESs), while in MQCL, the evolution occurs not only on single PESs but also on the average of these PESs.

3) FSSH is incapable of treating decoherence, which as mentioned previously stems from the lack of energy exchange between independent trajectories. In MQCL, while a trajectory evolves on a mean surface the observable in question acquires a phase factor [83, 84]. Fluctuations of the classical coordinates can cause this phase factor to oscillate in time differently for each trajectory, so averaging over an ensemble of trajectories can lead to destructive interference in the expectation value of an observable. In this sense, MQCL is able to treat decoherence.

4) FSSH is also incapable of treating recoherence properly while owing to the mean surface evolution, MQCL is capable of capturing recoherence.

1.5 Outline of thesis

Motivated by the need to properly incorporate all nonadiabatic couplings involved in a PCET reaction and to properly treat coherence/decoherence effects, our method of choice in this thesis is MQCL dynamics. In Chapter 2, we apply MQCL dynamics to the study of a reduced model of a PCET reaction. Since this work constitutes the first application of the MQCL approach to PCET, the model is chosen to be the same as that in Refs. 90, 91, and 92

(which is based on a charge transfer model developed in Ref. 93). By varying the parameters in the model Hamiltonian, PCET can either occur concertedly or sequentially between two positively charged ions. In Chapter 3, we use MQCL dynamics to calculate the adiabatic state populations for the same model. The results in this chapter will show a novel picture of nonadiabatic PCET reactions, thanks to MQCL dynamics. In Chapter 4, we derive a general, MQCL-based expression for the time-dependent rate coefficient of a PCET reaction and apply it to an improved version of the previously studied model to calculate the rate constant of a concerted PCET reaction. This rate constant is compared to the exact one for this model to assess the validity of our expression. Conclusions and future work are described in Chapter 5. Since atomic units are used commonly in this thesis, Table I contains several useful conversions from atomic units to SI and common units.

TABLE 1.1: Some useful unit conversions.

One atomic unit (a.u.)	SI units	Common units
Length	5.29×10^{-11} m	5.29 Å
Energy	4.36×10^{-18} J	627.5 kcal/mol
Time	2.42×10^{-17} J	0.0242 fs
Velocity	2.19×10^{6} m/s	

Chapter 2

An Analysis of Model Proton-Coupled Electron Transfer Reactions via the Mixed Quantum-Classical Liouville Approach

2.1 Introduction

A deep understanding of the mechanisms of PCET reactions is complicated by both the quantum mechanical nature of the transferring protons and electrons and the size and complexity of the environments in which they occur. To circumvent this problem, simplified models of complex systems may be studied to gain qualitative insights into the PCET mechanisms and/or mixed quantum-classical schemes may be used to gain quantitative information about PCET reaction rates.

Tully's FSSH [37] is one of the most widely used mixed quantum-classical methods for simulating the nonadiabatic dynamics of quantum processes in condensed phase systems. This method was applied to PCET for the first time in 1997 by Fang and Hammes-Schiffer [90].

They studied a simple model containing three coupled degrees of freedom, which represent a proton, an electron, and a solvent mode. The proton and electron were treated quantum mechanically, while the solvent mode was treated classically. By varying the model parameters, the authors investigated the nonadiabatic dynamics of both sequential (viz., ET followed by PT and PT followed by ET) and concerted PCET mechanisms. In a subsequent study [91], several different methods for incorporating decoherence into FSSH (which, on its own, evolves the wave function coherently) were applied to a similar model exhibiting a large number of avoided curve crossings. It was found that the agreement between the FSSH and exact quantum results for the adiabatic state populations was excellent at very short times (up to 19 fs), but at longer times, the results begin to differ and remain significantly different for the duration of the time (i.e., 168 fs). This deviation is most likely due to an improper treatment of decoherence.

In this Chapter, we employ for the first time a surface-hopping algorithm based on the numerical solution of the quantum-classical Liouville equation which is called MQCL [74–85] to study PCET. Since the MQCL inherently and rigorously accounts for quantum coherence/decoherence effects in mixed quantum-classical systems, it is expected to yield more accurate rate constants for condensed phase PCET reactions and may also shed new light on their underlying mechanisms. In fact, for the Azzouz-Borgis model of a proton transfer reaction in a phenol trimethylamine complex dissolved in CH_3Cl [86], it was found that the MQCL gives a proton transfer rate constant that is approximately twice as large [87] as that given by FSSH [88], thereby highlighting the differences between the two approaches for treating condensed phase charge transfer reactions.

Since this work constitutes the first application of the MQCL approach to PCET, we chose to study the same model as in Refs. 90, 91, and 92 (based on a charge transfer model developed in Ref. 93) to (1) demonstrate the applicability of this method to PCET reactions, (2) compare and contrast, wherever possible, with the results of the standard FSSH approach in Ref. 90, and (3) investigate the role played by mean surface evolution in the concerted and sequential mechanisms for a range of subsystem-bath couplings. This chapter is organized as follows: The three PCET models studied in this work are presented in Section 2. Section 3 summarizes the simulation details for generating nonadiabatic quantum-classical dynamics.

Section 4 presents and discusses the results for the model PCET reactions and concluding remarks are made in Section 5.

2.2 PCET model

The reduced model of a PCET reaction considered in this work contains three coupled degrees of freedom, representing a proton, an electron, and a solvent mode. The PCET reaction occurs between two positively charged ions, referred to as the donor (D) and acceptor (A), which are separated by a fixed distance d_{DA}. The coordinates of the proton and electron, denoted by q_p and q_e, respectively, are measured relative to D and they move from D to A only in one dimension, along the D–A axis (see Fig. 2.1).

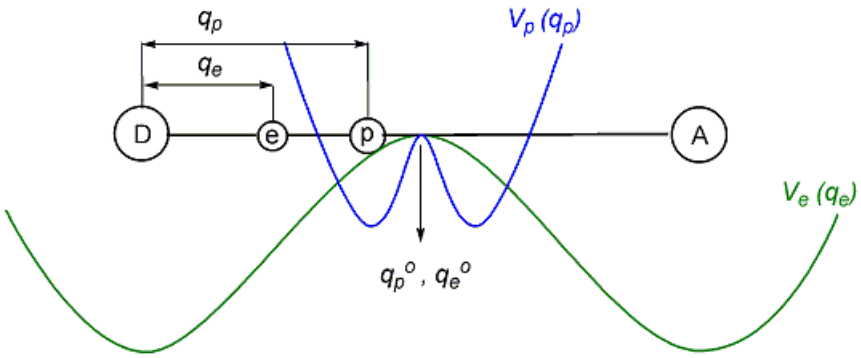

FIGURE 2.1: Schematic representation of the one-dimensional PCET model studied in this work. The protonic and electronic potentials (V_p and V_e, respectively) are superimposed onto the donor(D)−acceptor(A) axis. The protonic and electronic coordinates (q_p and q_e, respectively) are defined relative to the donor.

The coordinate of the collective solvent mode to which the proton and electron are coupled, is denoted by Q. Within our approach, the proton and electron are treated quantum mechanically, whereas the solvent mode is treated classically. The Hamiltonian of this mixed quantum-classical system is given by

$$\begin{aligned} \hat{H} &= \hat{K}_p + \hat{K}_e + K_s + \hat{V}_p(q_p) + \hat{V}_e(q_e) + \hat{V}_{pe}(q_p, q_e) + \hat{V}_{pes}(q_p, q_e, Q) + V_s(Q) \\ &\equiv \hat{h} + K_s. \end{aligned} \tag{2.1}$$

Here, $\hat{K}_p$ and $\hat{K}_e$ denote the kinetic energy operators of the proton and electron, respectively, K_s is the kinetic energy of the solvent mode, and $\hat{h} = \hat{H} - K_s$. The protonic potential energy

operator $\hat{V}_p$, as can be inferred from Fig. 2.1, is a double-well potential given by

$$\begin{aligned}\hat{V}_p(q_p) &= \frac{12\Delta E}{(a_2-a_1)^3(2a_3-a_1-a_2)}\left[\frac{q_p^4}{4}-(a_1+a_2+a_3)\frac{q_p^3}{3}\right.\\ &+ (a_1a_2+a_1a_3+a_2a_3)\frac{q_p^2}{2}-(a_1a_2a_3)q_p\\ &+ \left.\frac{a_2^2(a_2^2-2a_2(a_1+a_3)+6a_1a_3)}{12}\right],\end{aligned} \tag{2.2}$$

where a_1 and a_3 correspond to the positions of the two minima, where proton is near the donor or acceptor, respectively. a_2 corresponds to the position of the maximum between a_1 and a_3 and ΔE is the energy difference between the minimum at a_1 and a_2. The electronic potential energy operator, $\hat{V}_e$, corresponding to the Coulombic interactions between the electron and the donor and acceptor charges, is given by

$$\hat{V}_e(q_e) = -\frac{C_eC_D\mathrm{erf}(q_{eD}/\xi_{eD})}{q_{eD}} - \frac{C_eC_A\mathrm{erf}(q_{eA}/\xi_{eA})}{q_{eA}} + e^{-5.0(q_e+5.0)} + e^{-5.0(d_{DA}-q_e+5.0)}, \tag{2.3}$$

where C_e, C_D, and C_A are the partial charges of the electron, donor, and acceptor, respectively, and q_{eD} and q_{eA} are the distances between the electron and the donor and acceptor, respectively. In this work, both ξ_{eD} and ξ_{eA} are chosen to be equal to 1. The two last terms are added for numerical stability, they are repulsive terms that prevent the electron from travelling too far beyond the donor and acceptor. The potential energy operator corresponding to the Coulombic interaction between the proton and electron is given by

$$\hat{V}_{pe}(q_p,q_e) = -\frac{C_pC_e\mathrm{erf}(q_{pe}/\xi_{pe})}{q_{pe}}, \tag{2.4}$$

where $q_{pe} = |q_p - q_e|$ is the distance between the proton and electron. The coupling between the solvent coordinate and the proton and electron is bilinear in form and is given by the following operator:

$$\hat{V}_{pes}(q_p,q_e,Q) = -C_{sp}(Q-Q_p^o)(q_p-q_p^o) - C_{se}(Q-Q_e^o)(q_e-q_e^o), \tag{2.5}$$

where C_{sp} and C_{se} are the coupling parameters of the proton and electron to the solvent, respectively, and Q_p^o, Q_e^o, q_p^o, and q_e^o are free parameters. When $Q < Q_{p/e}^o$ and $q < q_{p/e}^o$, the proton/electron is stabilized near the donor. Conversely, if $Q > Q_{p/e}^o$ and $q > q_{p/e}^o$, the

proton/electron is stabilized near the acceptor. Finally, the dynamics of the classical solvent mode is governed by a harmonic potential of the form

$$V_s(Q) = \frac{1}{2} m_s {\omega_s}^2 (Q - Q_o)^2, \tag{2.6}$$

where m_s and ω_s are the mass and frequency, respectively, of the collective solvent mode. It should be noted that for Hamiltonians with bath terms that are harmonic and subsystem-bath coupling terms that are linear in the bath coordinates, MQCL dynamics is exact. The only approximation made in the sequential short-time propagation (SSTP) solution of the MQCL equation is the momentum-jump approximation, which has been shown numerous times to be a very good approximation.

By varying the parameters in the Hamiltonian, one can generate systems in which the proton and electron transfer take place in a concerted fashion and systems in which the transfer is sequential, i.e., PT before ET (i.e., PT-ET) and vice versa (i.e., ET-PT). The parameter values used to investigate the concerted, sequential PT-ET, and sequential ET-PT mechanisms are presented in Table 1. The main differences between the three sets of parameter values are as follows: The partial charges on the proton and electron are chosen to be higher (i.e., ± 0.32) in the concerted case than in the sequential cases (i.e., ± 0.15) since the attraction between the proton and electron should be higher for them to transfer together. In order for the proton and electron to transfer in a concerted fashion, they should also be similarly coupled to the solvent and therefore their respective couplings are chosen to be equal (i.e., $C_{sp} = C_{se}$). In contrast, in the case of sequential transfer, the proton and electron should experience different degrees of coupling to the solvent. In addition to the differences in the couplings to the solvent, the parameters Q_p^o, Q_e^o, and Q_o are different for each mechanism. Namely, $Q_p^o = Q_e^o = Q_o$ in the case of concerted PCET, $Q_p^o < Q_o$ and $Q_e^o > Q_o$ for PT-ET, and $Q_e^o < Q_o$ and $Q_p^o > Q_o$ for ET-PT. In all cases, the midpoint of the donor−acceptor distance coincides with the barrier tops of the protonic and electronic potentials (i.e., $q_p^o = q_e^o = d_{DA}/2$).

The validity of these parameters is confirmed by examining the 2D potential energy surfaces (PESs) as a function of q_p and q_e in Fig. 2.2. For example, if one examines the 2D PES of concerted PCET, top row in Fig. 2.2, at $Q = -0.4$ a.u., which is before the midpoint of the D–A distance or the barrier tops of the protonic and electronic potentials, the well at

TABLE 2.1: Parameters values (in atomic units) for the concerted PCET (top), sequential PT-ET (middle), and ET-PT (bottom) reactions.

$m_s = 22000.0$	$Q_o = 0.0$	$\omega_s = 3.72 \times 10^{-4}$	
$a_1 = 2.5$	$a_2 = 3.0$	$a_3 = 3.5$	$\Delta E = 1.2 \times 10^{-2}$
$d_{DA} = 6.0$	$C_D = 0.6$	$C_A = 0.6$	
$C_p = 0.32$	$C_e = 0.32$	$q_p^o = 3.0$	$q_e^o = 3.0$
$Q_p^o = 0.0$	$Q_e^o = 0.0$	$C_{sp} = 2.0 \times 10^{-3}$	$C_{se} = 2.0 \times 10^{-3}$
$m_s = 22000.0$	$Q_o = -0.4$	$\omega_s = 4.0 \times 10^{-4}$	
$a_1 = 3.5$	$a_2 = 4.0$	$a_3 = 4.55$	$\Delta E = 1.2 \times 10^{-2}$
$d_{DA} = 8.0$	$C_D = 0.6$	$C_A = 0.6$	
$C_p = 0.15$	$C_e = 0.15$	$q_p^o = 4.0$	$q_e^o = 4.0$
$Q_p^o = -0.6$	$Q_e^o = 0.0$	$C_{sp} = 1.0 \times 10^{-2}$	$C_{se} = 2.0 \times 10^{-3}$
$m_s = 22000.0$	$Q_o = -0.3$	$\omega_s = 4.0 \times 10^{-4}$	
$a_1 = 3.5$	$a_2 = 4.0$	$a_3 = 4.5$	$\Delta E = 1.2 \times 10^{-2}$
$d_{DA} = 8.0$	$C_D = 0.55$	$C_A = 0.55$	
$C_p = 0.15$	$C_e = 0.15$	$q_p^o = 4.0$	$q_e^o = 4.0$
$Q_p^o = 0.0$	$Q_e^o = -0.6$	$C_{sp} = 3.0 \times 10^{-2}$	$C_{se} = 4.0 \times 10^{-3}$

$q_p = 2.5$ a.u./$q_e = 0.0$ a.u. has the lowest depth. It means that both proton and electron are near the donor. On the other hand, at $Q = +0.4$ a.u., which is after the barrier tops of the protonic and electronic potentials, the well at $q_p = 3.5$ a.u./$q_e = 6.0$ a.u. has the lowest depth. It means that both proton and electron are near the acceptor. At $Q = 0.0$ a.u., which coincides with the barrier tops of the potentials, both of these wells show the same depth, i.e. both proton and electron are at the midpoint between the donor and the acceptor.

2.3 Simulation details

To carry out the SSTP algorithm, one needs to solve the time-independent Schrödinger equation at each step of the simulation:

$$\hat{h}|\alpha; Q\rangle = E_\alpha(Q)|\alpha; Q\rangle, \tag{2.7}$$

where $\hat{h}$ is the model Hamiltonian given in Eq. 2.1. This involves expanding the adiabatic wave function $|\alpha; Q\rangle$ in an orthonormal set of two-particle basis functions as

$$|\alpha; Q\rangle = \sum_{m,n} c_{mn}^{\alpha} |\phi_{p(m)}\rangle |\phi_{e(n)}\rangle, \tag{2.8}$$

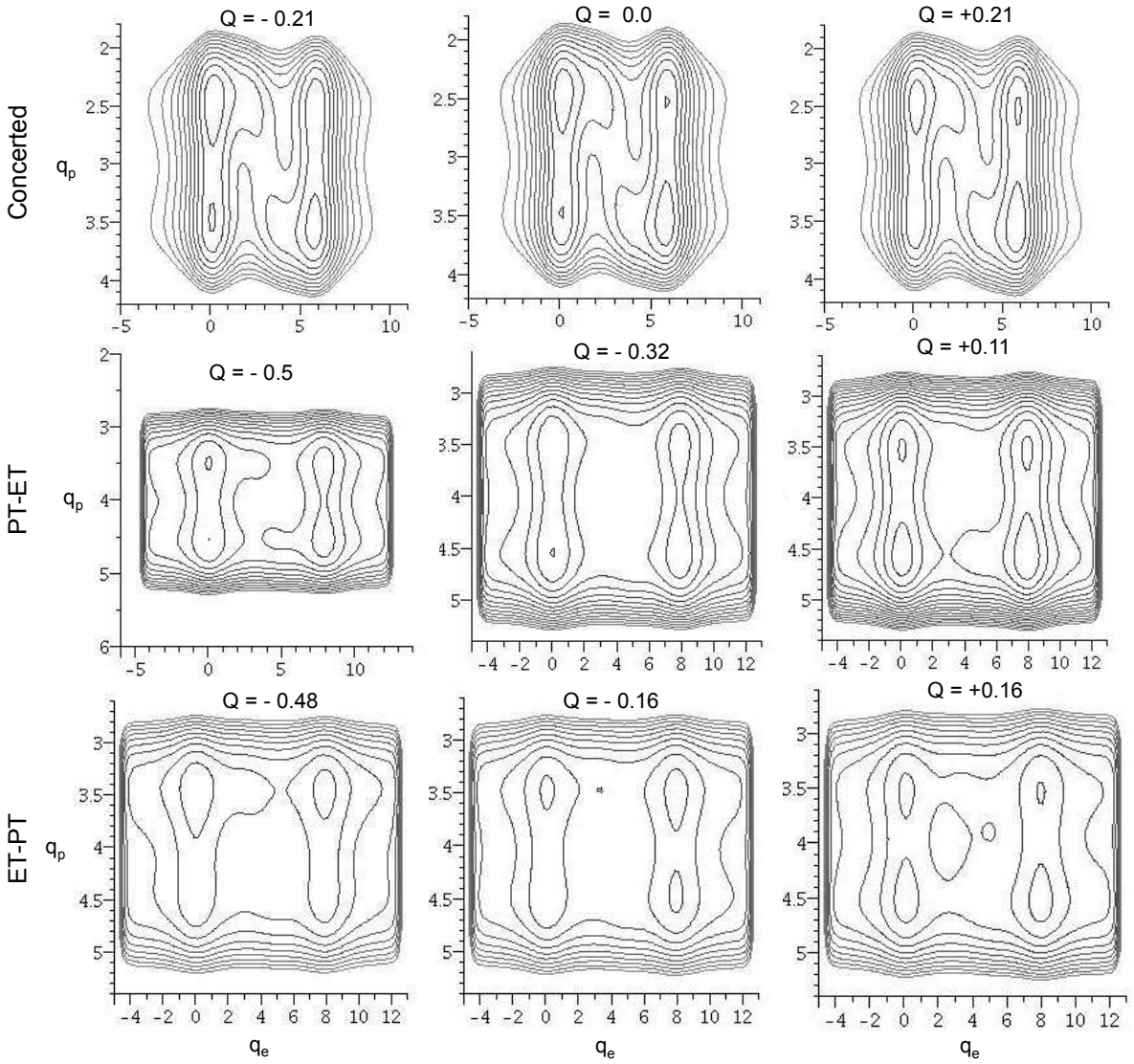

FIGURE 2.2: The 2D PESs as a function of q_p and q_e at different solvent configurations for concerted PCET (top row), sequential PT-ET (middle row), and the sequential ET-PT (bottom row) mechanisms. Q values are in Å but q_p and q_e values in this figure are given in a.u.

where $|\phi_{p(m)}\rangle$ and $|\phi_{e(n)}\rangle$ are one-particle basis functions and are chosen to be the solutions of the quantum harmonic oscillator for a proton and an electron, respectively, i.e.,

$$\phi_{p(m)}(q_p) = \langle q_p|\phi_{p(m)}\rangle = (2^m m!\sqrt{\pi})^{-1/2}\alpha_p^{1/2}e^{-\alpha_p^2(q_p-q_p^o)/2}H_m(\alpha_p(q_p-q_p^o)), \tag{2.9}$$

and

$$\phi_{e(n)}(q_e) = \langle q_e|\phi_{e(n)}\rangle = (2^n n!\sqrt{\pi})^{-1/2}\alpha_e^{1/2}e^{-\alpha_e^2(q_e-q_e^o)/2}H_n(\alpha_e(q_e-q_e^o)), \tag{2.10}$$

where m and n are integers and $H_m(q)$ is a Hermite polynomial. For convergence, we used a total of 625 two-particle basis functions in the expansion in Eq. 2.8, i.e., $0 < \{m, n\} < 24$. The one-particle protonic and electronic functions are centred at q_p^o and q_e^o, respectively, and $\alpha_p = 3.97$ Å^{-1} and $\alpha_e = 0.32$ Å^{-1}. We solve the eigenvalue problem, $hc = cE$, at each molecular dynamics step to obtain $\{c_{mn}^{\alpha}\}$ and $\{E_\alpha\}$, where h is the 625×625 Hamiltonian with matrix elements $h_{\{ij\}\{kl\}} = \langle \phi_{p(i)}\phi_{e(j)}|\hat{h}(Q)|\phi_{p(k)}\phi_{e(l)}\rangle$. The matrix elements $h_{\{ij\}\{kl\}}$ are calculated using the trapezoid rule with 100 points evenly spaced over the range $q_p = 1.06/1.59$ Å to $q_p = 2.12/2.65$ Å for the protonic integrals in the case of the concerted/sequential mechanisms and 700 points over the range $q_e = -3.17$ Å to $q_e = 6.35$ Å for the electronic integrals in the case of all mechanisms.

The nonadiabatic coupling matrix element, $d_{\alpha\beta}$, for this model is given by:

$$\begin{aligned} d_{\alpha\beta} &= \frac{-1}{\Delta E_{\alpha\beta}} \langle \alpha; Q | \frac{\partial \hat{h}}{\partial Q} | \beta; Q \rangle \\ &= \frac{1}{\Delta E_{\alpha\beta}} \sum_{mnkl} c_{mn}^{\alpha} c_{kl}^{\beta} [C_{sp} \langle \phi_{p(m)} | (q_p - q_p^o) | \phi_{p(k)} \rangle \delta_{nl} + C_{se} \langle \phi_{e(n)} | (q_e - q_e^o) | \phi_{e(l)} \rangle \delta_{mk}], \end{aligned} \tag{2.11}$$

and the Hellmann-Feynman forces, F_W^{α}, are given by:

$$\begin{aligned} F_W^{\alpha} &= -\langle \alpha; Q | \frac{\partial \hat{h}(Q)}{\partial Q} | \alpha; Q \rangle \\ &= \sum_{mnkl} c_{mn}^{\alpha} c_{kl}^{\alpha} [C_{sp} \langle \phi_{p(m)} | (q_p - q_p^o) | \phi_{p(k)} \rangle \delta_{nl} + C_{se} \langle \phi_{e(n)} | (q_e - q_e^o) | \phi_{e(l)} \rangle \delta_{mk}]. \end{aligned} \tag{2.12}$$

After summing the Hellmann-Feynman forces and the classical forces, the classical degrees of freedom are propagated using the velocity-Verlet algorithm with a time step of 2.4 fs.

2.4 Results

2.4.1 Adiabatic potential energy surfaces and nonadiabatic couplings

The ground (1,1) and first-excited (2,2) state adiabatic potential energy surfaces (and the corresponding mean surfaces [(1,2) or (2,1)]) as a function of the solvent coordinate for the concerted, sequential PT-ET, and sequential ET-PT mechanisms are shown in Fig. 2.3.

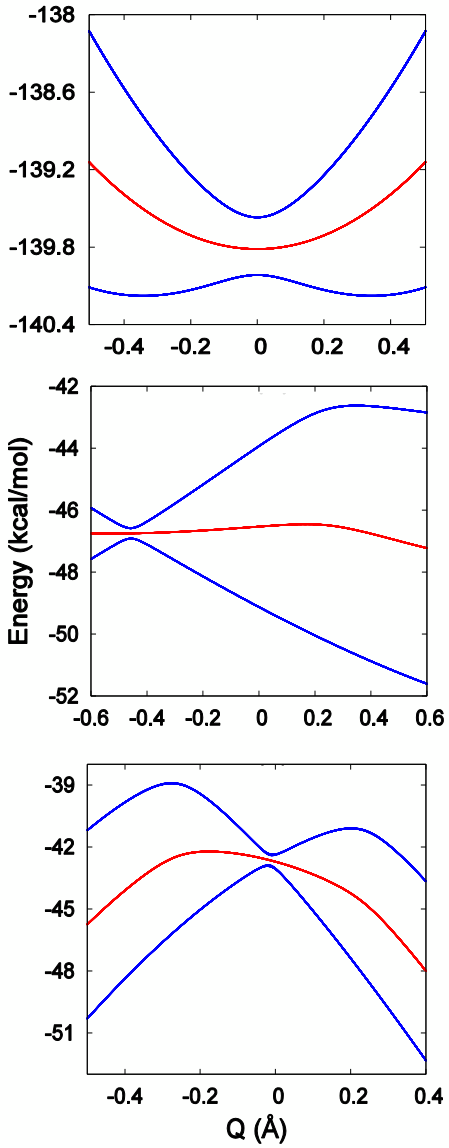

FIGURE 2.3: Adiabatic potential energy surfaces as a function of the solvent coordinate, Q, for the concerted (top), PT-ET (middle), and ET-PT (bottom) reactions. The blue curves correspond to the ground and first excited state surfaces, while the red curves correspond to the mean surfaces.

In this work, the dynamics is restricted to the two lowest states since based on our preliminary calculations, which are also confirmed by Ref. 90, the higher excited states are rarely populated for the range of initial momenta considered here. For concerted PCET (top panel of Fig. 2.3), both the ground and first excited state surfaces are symmetric about $Q = 0$ Å. The minimum energy gap of 0.44 kcal/mol between the surfaces occurs at the barrier top of the ground state surface (i.e., at $Q = 0$ Å). The ground state surface exhibits two minima,

one at $Q = -0.4$ Å and the other at $Q = 0.4$ Å, corresponding to stable solvent configurations in which the proton and electron are near the donor and acceptor, respectively. We have confirmed this by examining the ground state adiabatic wavefunction in Fig. 2.4 where at a negative value of Q, i.e. to the left of the energy barrier, the wavefunction is centred at the donor site but for a positive value of Q, i.e. to the right of the barrier, it is centred at the acceptor site. At $Q = 0.0$ Å the wave function has spread towards both the donor and the acceptor sites, note that both contours in the middle panel of the ground state in Fig. 2.4 have positive signs.

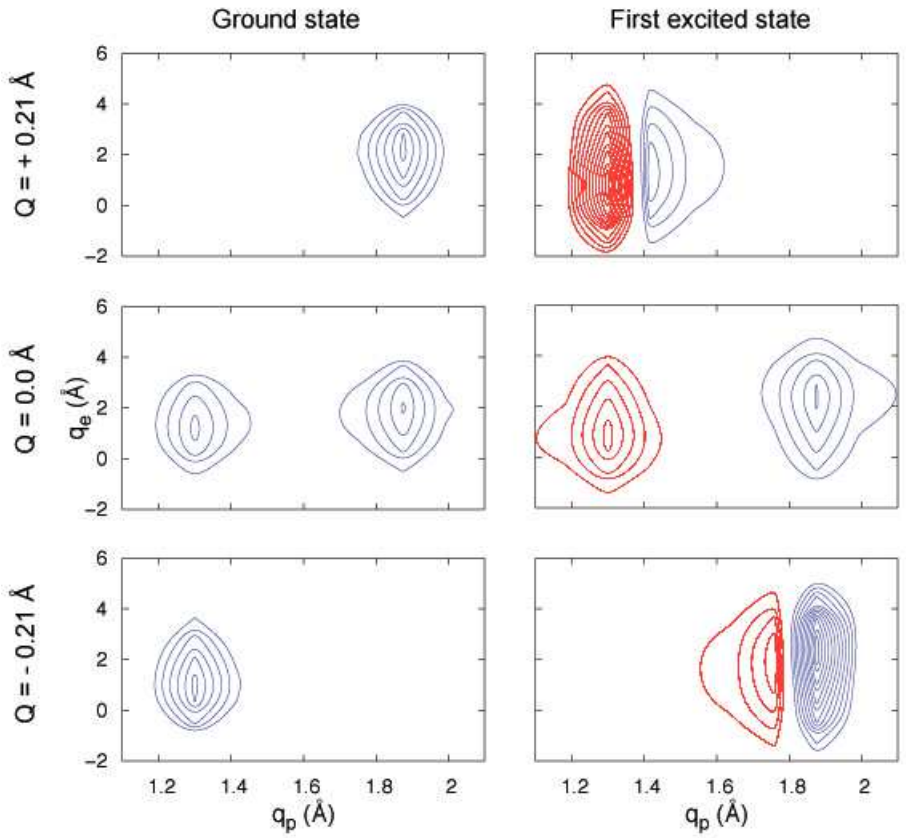

FIGURE 2.4: The ground and the first excited state wave functions for the concerted PCET as a function of the solvent configuration.

In contrast to the ground state surface, the excited state surface exhibits a single minimum at $Q = 0.0$ Å. An examination of the excited state wave functions reveals that for $Q = -0.21$ Å, the proton and electron are near the acceptor, while for $Q = +0.21$ Å they are near the donor. Note that the two contours in all the excited state panels in Fig. 2.4 have opposite signs showing the presence of a node in the first excited state wavefunction. The mean surface exhibits a shallow well, whose minimum occurs at $Q = 0.0$ Å. In the concerted case,

a PCET reaction takes place when the system starts at the donor site on the ground state surface (i.e., at $Q < 0.21$ Å) and moves to the acceptor site on the ground state surface (i.e., at $Q > 0.21$ Å).

In the case of sequential PCET, the ground and first excited state surfaces are asymmetric about the ground state barrier tops, see Fig. 2.3 for close-ups on the barrier top regions and Fig. 2.5 for the full surfaces. For PT-ET, the ground state surface has a barrier top centered

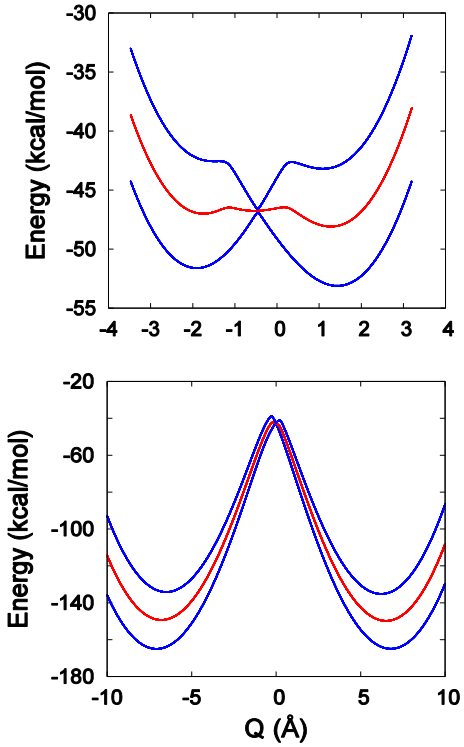

FIGURE 2.5: Potential energy surfaces of PT-ET (top), and ET-PT (bottom) mechanisms as a function of solvent configuration.

at $Q = -0.46$ Å, the excited state surface exhibits one main well (with two shallow wells flanking it), and the mean surface exhibits a relatively flat region centered at $Q = -0.46$ Å (with two shallow wells flanking it). The minimum energy gap between the ground and first exited states is 0.33 kcal/mol. For ET-PT, the ground and first excited state surfaces are more asymmetric about the ground state barrier top than the PT-ET surfaces, and the mean surface exhibits a broad barrier top. The minimum energy gap is 0.46 kcal/mol at $Q = -0.02$ Å. The characters of the ground state wave functions at different solvent configurations are shown in Fig. 2.6 for both sequential mechanisms.

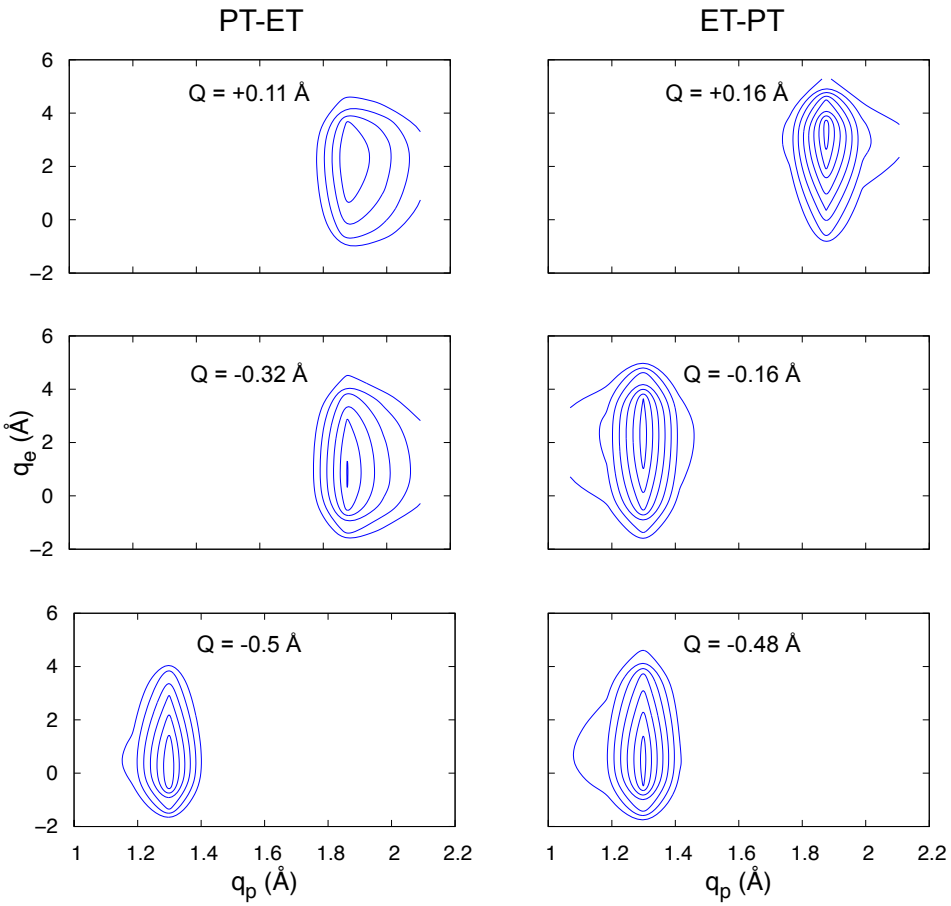

FIGURE 2.6: The ground state wave functions for the sequential PCET mechanisms as a function of the solvent configuration.

For PT-ET, the ground state wave function reveals that at $Q = -0.5$ Å (i.e., to the left of the barrier top), both the proton and electron are near the donor, while at $Q = -0.32$ Å the proton transfers to the acceptor but the electron remains at the donor. However, at $Q = 0.11$ Å, both the proton and electron are located near the acceptor. Hence, once the proton has transferred to the acceptor, there is no barrier associated with the motion of the solvent as the electron transfers to the acceptor. For ET-PT, the situation is reversed. The ground state wave function reveals that at $Q = -0.48$ Å (i.e., to the left of the barrier top), both the proton and electron are near the donor, while at $Q = -0.16$ Å (i.e., to the left of the barrier top) the electron transfers to the acceptor but the proton remains at the donor. However, at $Q = 0.16$ Å, both the proton and electron are located near the acceptor. Examination of the first excited state wave functions for PT-ET and ET-PT reveals that at Q equal to 0.42 Å and 0.45 Å, respectively, the proton and electron are near the acceptor. Therefore, a successful reaction takes place when the system starts at the donor site on the ground state

surface (viz., at $Q < -0.6$ Å and -0.2 Å for PT-ET and ET-PT, respectively) and moves to the acceptor site on either the ground or excited state surfaces (viz., at $Q > 0.11$ Å and 0.42 Å for the ground and first excited states, respectively, of PT-ET and $Q > 0.2$ Å and 0.4 Å for the ground and first excited states, respectively, of ET-PT).

To gain insight into the strength of the nonadiabatic coupling between the adiabatic surfaces and, hence, into the regions where nonadiabatic transitions are likely to occur, we calculated $|d_{12}|$ as a function of the solvent configuration Q for the various PCET mechanisms. In the right-hand panels of Fig. 2.7, we show $|d_{12}|$ vs. Q for concerted PCET (top panel), PT-ET (middle panel), and ET-PT (bottom panel). As expected, $|d_{12}|$ is peaked at the Q values corresponding to the ground state barrier top where the energy gap between the ground and first excited state surfaces is the smallest. We also see that $|d_{12}|$ attains higher values in ET-PT than in PT-ET than in concerted PCET. This is a reflection of the differences in the energy gaps and relative curvatures of the ground and first excited state surfaces between the mechanisms. When we zoom in on the section of the PT-ET graph corresponding to lower $|d_{12}|$ values (see insets of Fig. 2.7), we see "bumps" on either side of the barrier top, which stretch over a relatively wide range of solvent configurations, and are due to the presence of wells on the excited state surface (see Fig. 2.5). Therefore, outside of the barrier top region, one can still expect some nonadiabatic transitions to occur (albeit to a much lesser extent than in the barrier top region).

In the following section, we describe the nature of the nonadiabatic dynamics observed in the concerted, sequential PT-ET, and sequential ET-PT mechanisms. In each case, we initialized trajectories with several different momenta, P_i, but with the same value of the solvent coordinate, Q_i.

2.4.2 Nonadiabatic dynamics

2.4.2.1 Concerted PCET mechanism

We generated an ensemble of 1000 trajectories, starting from $Q_i = -0.24$ Å on the ground state for the following values of the initial momentum: P_i =4.0, 7.0, 10.0, and 15.0 a.u. Each trajectory is terminated when it reaches a donor or acceptor configuration in the reactant or product well (i.e., $|Q| > 0.21$ Å) on the ground state surface. For this ensemble of trajectories,

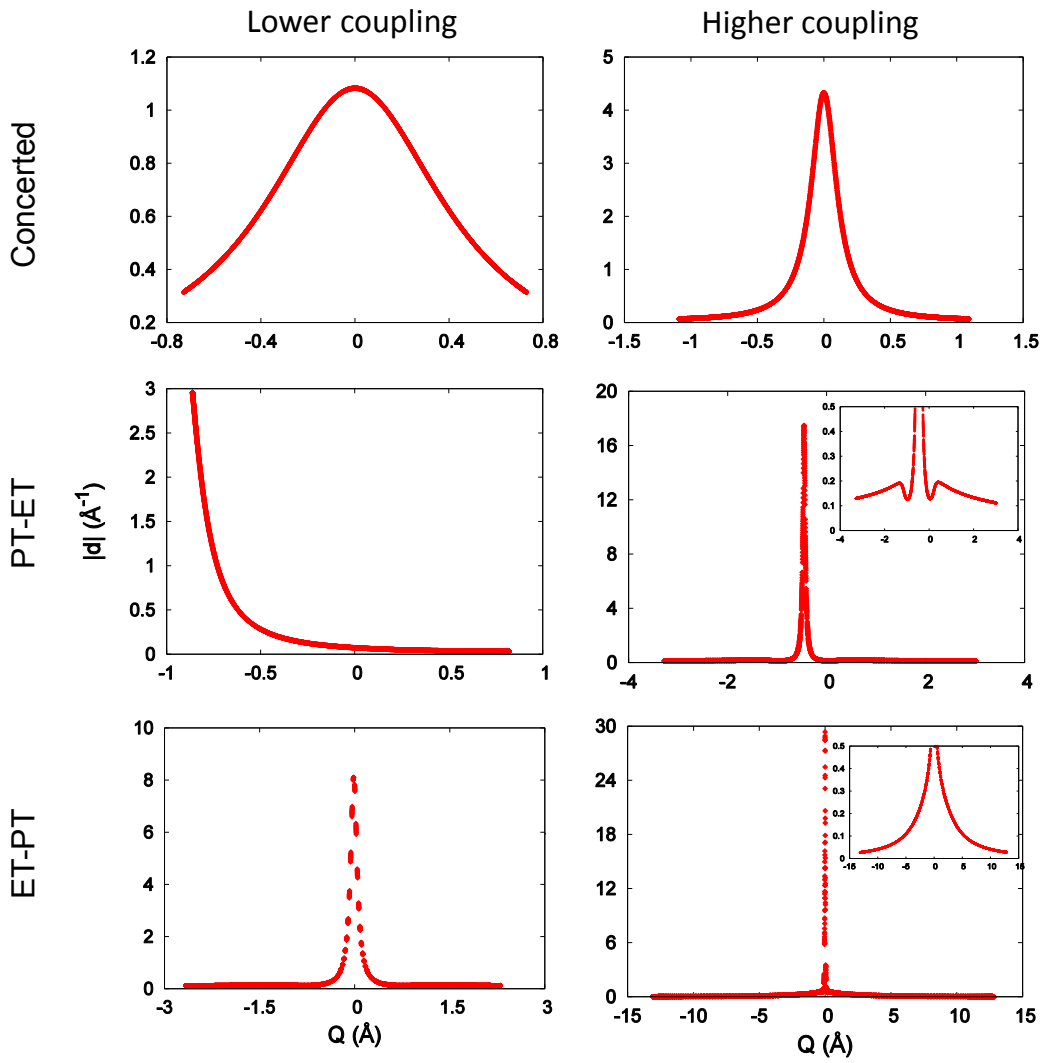

FIGURE 2.7: Nonadiabatic coupling strength, $|d_{12}|$, as a function of the solvent coordinate, Q, computed for concerted PCET (top panels), PT-ET (middle panels), and ET-PT (bottom panels). The insets zoom in on the sections corresponding to lower $|d_{12}|$ values. *Left panels*: Lower proton/electron-solvent coupling. The coupling constants for concerted PCET, PT-ET, and ET-PT are $C_{sp} = C_{se} = 5 \times 10^{-4}$, $C_{sp}/C_{se} = 2.5 \times 10^{-3}/5 \times 10^{-4}$, and $C_{sp}/C_{se} = 7.5 \times 10^{-3}/1 \times 10^{-3}$, respectively. *Right panels*: Higher proton/electron-solvent coupling. The coupling constants for concerted PCET, PT-ET, and ET-PT are $C_{sp} = C_{se} = 2 \times 10^{-3}$, $C_{sp}/C_{se} = 1 \times 10^{-2}/2 \times 10^{-3}$, and $C_{sp}/C_{se} = 3 \times 10^{-2}/4 \times 10^{-3}$, respectively.

we started by examining the percentage of trajectories, % PCET, which successfully go from the reactant well on the ground state to the product well on the ground state, whether adiabatically or nonadiabatically. The top panel of Fig. 2.8 illustrates % PCET as a function of the initial momentum. After an initial decrease from 100% to 71% in going from $P_i = 4.0$ a.u. to $P_i = 7.0$ a.u., % PCET remains relatively constant with increasing P_i. This should be contrasted with the results in Ref. 90, where substantial decreases in % PCET are observed

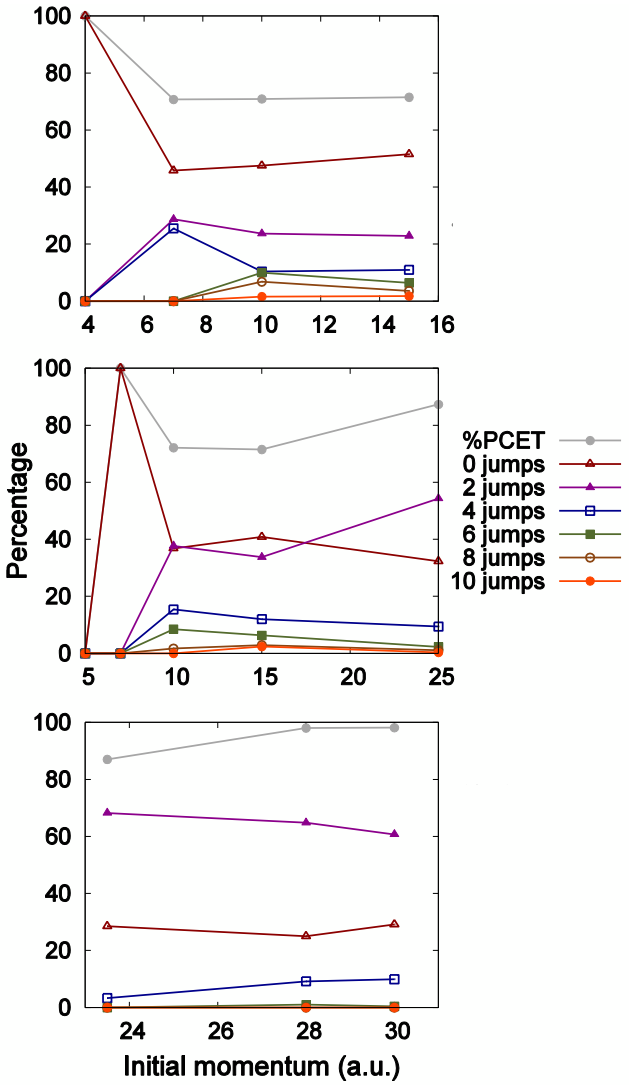

FIGURE 2.8: Percentage of trajectories which successfully undergo a PCET reaction (denoted by % PCET) and the percentage of these trajectories which contain 0, 2, 4, 6, 8, and 10 nonadiabatic transitions (denoted by 0 jumps, 2, jumps, etc.) as a function of the initial momentum for the concerted (top), PT-ET (middle), and ET-PT (bottom) reactions.

with increasing P_i. This difference is due to the fact that our dynamics can occur on the mean surface, whose shallow well can facilitate the PCET. Also shown in the top panel of Fig. 2.8 are the percentages of the sub-ensemble of trajectories that successfully underwent PCET with 0 (i.e., adiabatic), 2, 4, 6, 8, and 10 nonadiabatic transitions. It should be noted that only even numbers of jumps were considered since successful PCETs cannot terminate on the mean surfaces. At $P_i = 4.0$ a.u., 100% of PCETs occur adiabatically, but when P_i increases to 7.0 a.u., there is a large drop in the percentage of adiabatic PCETs to 46% due to the onset of nonadiabatic transitions. For $P_i \geq 10.0$ a.u., we see that the percentages of reactive

trajectories undergoing any number of jumps do not change significantly with increasing P_i, with $\sim 50\%$ of PCETs occurring adiabatically, $\sim 23\%$ nonadiabatically via two nonadiabatic transitions, and $\sim 27\%$ nonadiabatically via four or more nonadiabatic transitions. This means that beyond $P_i = 7.0$ a.u., approximately 0.50×72%=36% of the entire ensemble of trajectories undergo PCET adiabatically, 0.23×72%=17% undergo PCET via two jumps, and 0.27×72%=19% undergo PCET via four or more jumps. As can be seen, the majority of reactive, nonadiabatic trajectories follow the $(1,1) \rightarrow (1,2)/(2,1) \rightarrow (1,1)$ pathway, and a smaller percentage follow the $(1,1) \rightarrow (1,2)/(2,1) \rightarrow (2,2) \rightarrow (1,2)/(2,1) \rightarrow (1,1)$ pathway.

The top panel of Fig. 2.9 presents the percentage of time spent on the various surfaces over the ensemble of 1000 trajectories. We see that for $P_i = 4.0$ a.u., 100% of the time is spent on the (1,1) surface. For this initial momentum, the system is unable to make any jumps. However, as P_i is increased, we see a large initial drop in the time spent on the (1,1) surface to 19% (and eventually to 7% for $P_i = 15.0$ a.u.), an increase in the time spent on the (1,2) and (2,1) surfaces to 70%, and a gradual increase in the time spent on the (2,2) surface to 26% for $P_i = 15.0$ a.u. The increases in the (1,2)/(2,1) and (2,2) percentages take place since the system has sufficient momentum to frequently enter into the strong nonadiabatic coupling region. It should be noted that in the limit of a sufficiently large ensemble, the (1,2) and (2,1) percentages should be equal. Overall, these results underscore the importance of mean surface evolution in the ensemble.

2.4.2.2 Sequential PT-ET mechanism

We generated ensembles of 1000 trajectories, starting from $Q_i = -0.58$ Å on the ground state for the following values of the initial momentum: P_i =5.0, 7.0, 10.0, 15.0, and 25.0 a.u. Each trajectory is terminated when it reaches an acceptor configuration on either the ground or first excited state (i.e., $Q > 0.11$ Å and $Q > 0.42$ Å, respectively) or returns to a donor configuration (i.e., $Q < -0.6$ Å) on the ground state. % PCET varies from 0% to 100% to 72% to 72% to 87% in going from $P_i = 5.0$ a.u. to $P_i = 25.0$ a.u., not exhibiting any noticeable trend beyond $P_i = 7.0$ a.u. (see middle panel of Fig. 2.8). The minimum momentum, i.e., $P_i = 7.0$ a.u., at which trajectories begin to undergo PCET reactions is somewhat higher than that in the concerted case, i.e., $P_i = 4.0$ a.u. This is a reflection of the longer distance between the donor and acceptor for PT-ET than for concerted PCET (see

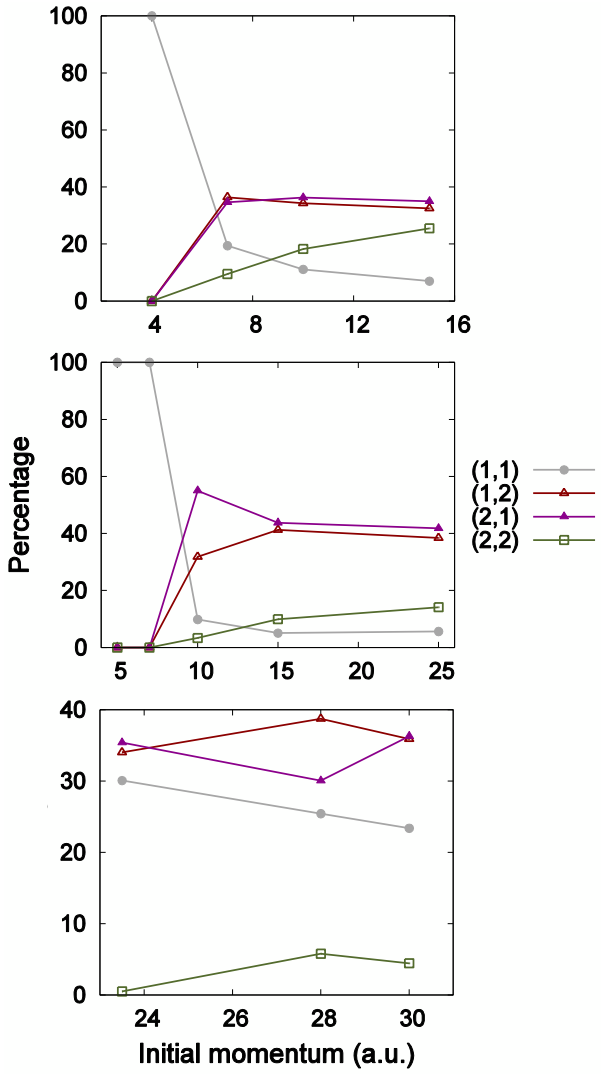

FIGURE 2.9: Percentage of time (out of the entire ensemble) spent on the ground state (1,1), mean [(1,2) and (2,1)], and first excited state (2,2) surfaces as a function of the initial momentum for the concerted (top), PT-ET (middle), and ET-PT (bottom) mechanisms.

Table 1), which leads to a higher ground state barrier for PT-ET than for concerted PCET (see Fig. 2.3). Increasing the initial solvent momentum beyond $P_i = 15.0$ a.u. leads to a higher % PCET since the probability of nonadiabatic transitions from the (1,2)/(2,1) to the (1,1) and (2,2) surfaces becomes high enough such that more jumps to these surfaces occur outside of the barrier top region. This should be contrasted with what was found in Ref. 90, where % PCET starts at 9%, fluctuates, and ultimately reaches its maximum value (83%) at the highest P_i value of 25 a.u. In this case, the absence of mean surface evolution would prevent the possibility for % PCET to dramatically increase for the intermediate values of the initial momentum.

The middle panel of Fig. 2.8 shows the percentages of the sub-ensemble of trajectories that successfully underwent PCET with 0, 2, 4, 6, 8, and 10 nonadiabatic transitions. For P_i = 10.0 a.u., in contrast to the concerted case, we see that the percentages of 2- and 4-jump trajectories is significantly higher, viz., 38% and 15%, respectively (at the expense of 0-jump trajectories). When P_i is increased from 10.0 a.u. to 25 a.u., the percentages change, with each profile exhibiting a different behaviour. The 0-jump contribution increases to a maximum (41% at P_i = 15 a.u.) and then decreases; the 2-jump contribution decreases to a minimum (34% at P_i = 15 a.u.) and then increases dramatically; the 4- and 6-jump contributions decrease gradually (while the higher jump contributions become negligible).

The trends of the percentages of time spent on each surface are very similar to those of concerted PCET, but the magnitudes are somewhat different (see middle panel of Fig. 2.9). Of particular note, we see that less time is spent on the (2,2) surface and more time on the mean surfaces than in concerted PCET, for all initial momenta in common. In going from P_i = 15.0 a.u. to P_i = 25.0 a.u., we see that the percentages of time spent on the mean surfaces exhibit very slight decreases, while the percentage of time spent on the (2,2) surface increases slightly. Again, we see that evolution on the mean surfaces plays an important role in the ensemble ($\sim$ 80% for $P_i \geq$ 10.0).

2.4.2.3 Sequential ET-PT mechanism

We generated ensembles of 1000 trajectories, starting from $Q_i = -0.5$ Å on the ground state for the following (relatively high) values of the initial momentum: P_i =23.5, 28.0, and 30.0 a.u. Each trajectory is terminated when it reaches a donor or acceptor configuration on either the ground or excited state surface (viz., $|Q| > 0.2$ Å or $|Q| > 0.4$ Å, respectively). From the bottom panel of Fig. 2.8, we see that % PCET increases from 87% to 98% as P_i is increased. This is in stark contrast to what was found in Ref. 90, where % PCET ranges from 8% to 74% in going from P_i =23.5 to 30.0 a.u. This difference is due to the fact that our dynamics can occur on the mean surface, whose convex shape can strongly enhance the PCET.

The bottom panel of Fig. 2.8 also shows the percentages of the sub-ensemble of trajectories that successfully underwent PCET with 0, 2, 4, 6, 8, and 10 nonadiabatic transitions. As

P_i increases from 23.5 to 30.0 a.u., the percentages of 0- and 2-jump trajectories do not change significantly, while the percentage of 4-jump trajectories increases substantially (from 3% to 10%). In contrast to the case of PT-ET, for similarly high values of the momenta (viz., $P_i = 23.5$ a.u. of ET-PT vs. $P_i = 25.0$ a.u. of PT-ET), there is a smaller percentage of adiabatic trajectories (29% for ET-PT vs. 32% for PT-ET), a larger percentage of 2-jump trajectories (68% for ET-PT vs. 54% for PT-ET), and a smaller percentage of 4-jump trajectories (3% for ET-PT vs. 9% for PT-ET).

As in the concerted and PT-ET cases, the trajectories spend much of their time ($\sim 70\%$) on the (1,2) and (2,1) surfaces for all initial momenta. However, it is interesting to note that for these relatively high values of P_i, we see a substantial percentage ($23 - 30\%$) of time spent on the (1,1) surface, in contrast to the concerted and PT-ET cases. This is likely due to an increase in the percentages of 2-jump trajectories (relative to the concerted and PT-ET cases) that take the system away from the (1,2) and (2,1) surfaces and back to the (1,1) surface.

2.4.2.4 Role of phase factor

A unique feature of the MQCL surface-hopping algorithm is the phase factor from Eq. 1.20, $\mathcal{W}_{\alpha_{j-1}\alpha'_{j-1}}(t_{j-1}, t_j) = e^{-i\omega_{\alpha_{j-1}\alpha'_{j-1}}\Delta t_j}$, which enters into the evolution of an observable [83, 84]. Fluctuations of the classical coordinates can cause this phase factor to oscillate in time differently for each trajectory and, therefore, averaging over an ensemble of trajectories can lead to destructive interference in the expectation value of an observable. Therefore, one way to gauge the *decohering* effect of the environment on the quantum subsystem is to compute the average of the real part of $\mathcal{W}(t)$, $\langle \mathrm{Re}[\mathcal{W}(t)] \rangle$, over an ensemble of trajectories starting from a given Q_i and a distribution of momenta centred around a given P_i (corresponding to a temperature of 300 K). In Fig. 2.10, we see that $\langle \mathrm{Re}[\mathcal{W}(t)] \rangle$ (averaged over 1000 trajectories) exhibits a different decay time and profile for each PCET mechanism considered.

In the case of concerted PCET, PT-ET, and ET-PT, $\langle \mathrm{Re}[\mathcal{W}(t)] \rangle$ decays to zero in $50 - 150$ fs, $75 - 100$ fs, and 75 fs, respectively. Although the initial decay rates are different for each mechanism, in general, the initial decay rate increases as P_i is increased. These results suggest

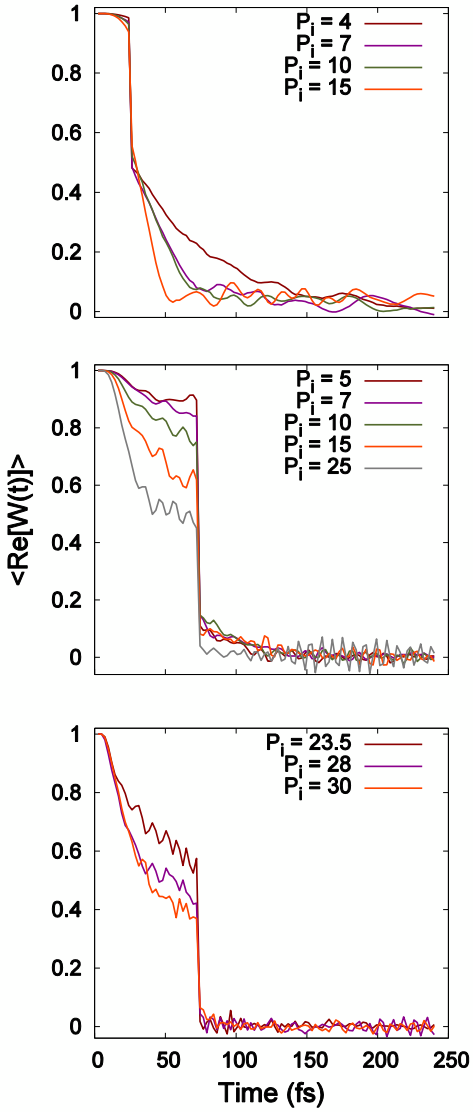

FIGURE 2.10: Average of the real part of $\mathcal{W}(t)$, $\langle \mathrm{Re}[\mathcal{W}(t)] \rangle$, over an ensemble of trajectories starting from Q_i =-0.24, -0.58, and -0.5 Å and initial momentum distributions (corresponding to a temperature of 300 K) centred around different P_i, for the concerted (top), PT-ET (middle), and ET-PT (bottom) reactions, respectively.

that phase effects are important when studying PCET processes on ultrafast timescales, and will differ depending on the mechanism in question.

2.4.3 Effect of proton/electron-solvent coupling strength

We investigated the effect of varying the coupling strength between the proton/electron and the solvent on the nonadiabatic coupling, $|d_{12}|$, in order to gain insight into how this

will affect the nonadiabatic dynamics. The results for the original coupling strength are contrasted with those for a lower coupling strength in Fig. 2.7. For concerted PCET, as the coupling strength increases, we see that the overall distribution of $|d_{12}|$ values becomes narrower and grows in height. This is mainly due to the change in the relative curvatures of the ground and excited state surfaces. Therefore, as the coupling strength increases, the probability of nonadiabatic transitions becomes very high at the barrier top and drops off quickly outside of this region. That being said, at lower coupling strengths, the probability of nonadiabatic transitions is higher outside of the barrier top region. For PT-ET, increasing the coupling not only causes an increase in the central peak height of the distribution, but also a shift in the peak position to larger Q values. Therefore, as the coupling strength increases, the region where the probability of nonadiabatic transitions is highest shifts to larger Q values. For ET-PT, increasing the coupling also causes an increase in the central peak height. Thus, in all three cases, increasing the coupling will significantly affect the nonadiabatic dynamics, but not necessarily in the same way.

In Fig. 2.11, we show the effect of varying the coupling strength between the proton/electron and the solvent on % PCET (based on ensembles of 1000 trajectories) for each value of the initial momentum. For each mechanism, the seven different sets of coupling constants studied are listed in Table 2 in order of increasing coupling strength (note that the original ratio of C_{sp} to C_{se} is maintained for each mechanism).

TABLE 2.2: Seven sets of proton/electron-solvent coupling constants (i.e., $\{C_{sp}, C_{se}\}$) considered in this study for the three PCET mechanisms, ranging from low (1) to high (7) coupling. All values are in atomic units.

		Coupling constants						
		1	2	3	4	5	6	7
Concerted	C_{sp}	1×10^{-4}	5×10^{-4}	1×10^{-3}	2×10^{-3}	3×10^{-3}	4×10^{-3}	8×10^{-3}
	C_{se}	1×10^{-4}	5×10^{-4}	1×10^{-3}	2×10^{-3}	3×10^{-3}	4×10^{-3}	8×10^{-3}
PT-ET	C_{sp}	5×10^{-4}	2.5×10^{-3}	5×10^{-3}	1×10^{-2}	1.5×10^{-2}	2×10^{-2}	4×10^{-2}
	C_{se}	1×10^{-4}	5×10^{-4}	1×10^{-3}	2×10^{-3}	3×10^{-3}	4×10^{-3}	8×10^{-3}
ET-PT	C_{sp}	3.75×10^{-3}	7.5×10^{-3}	1.5×10^{-2}	3×10^{-2}	6×10^{-2}	1.2×10^{-1}	2.4×10^{-1}
	C_{se}	5×10^{-4}	1×10^{-3}	2×10^{-3}	4×10^{-3}	8×10^{-3}	1.6×10^{-2}	3.2×10^{-2}

In the concerted case (see top panel of Fig. 2.11), as the coupling strength is increased for $P_i = 4.0$ and 7.0 a.u., % PCET first decreases, then increases to 100%, and, beyond a certain threshold coupling strength, drops to zero since the barrier becomes too high for reactions to occur, see Fig. 2.12. This behaviour is likely due to the fact that for coupling strengths lower than the threshold coupling strength, trajectories traversing towards the

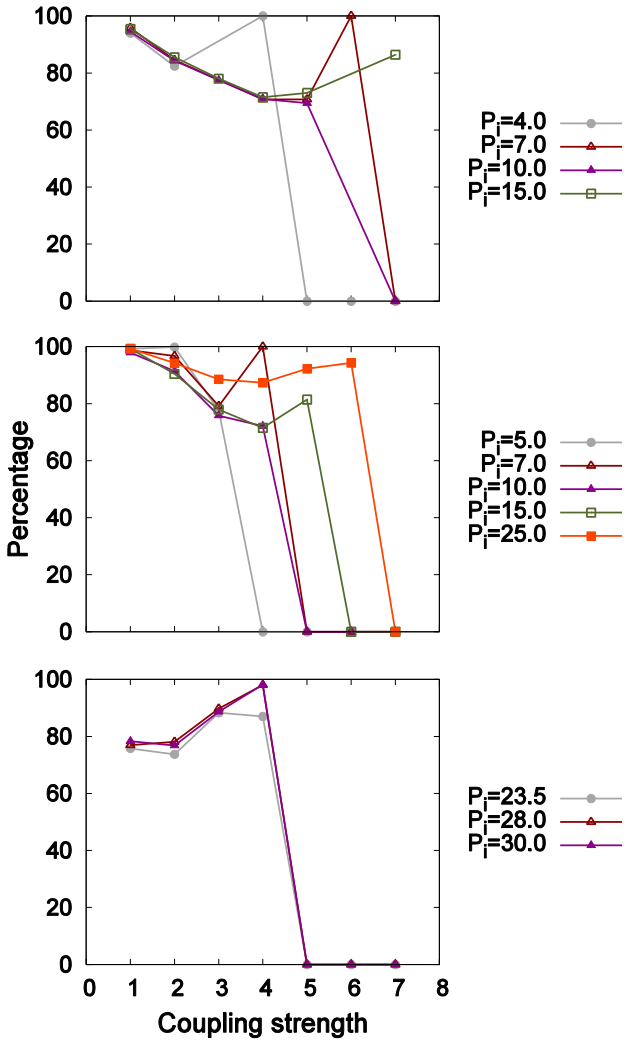

FIGURE 2.11: Percentage of trajectories which successfully undergo a PCET reaction as a function of the coupling strength between the proton/electron and the solvent for various initial momenta, P_i, for the concerted (top), PT-ET (middle), and ET-PT (bottom) reactions. The x-axis labels, $1-7$, represent seven sets of coupling constants $\{C_{sp}, C_{se}\}$ (values given in Table 2), listed in order of increasing strength.

acceptor configuration may return to the donor side via the mean surface, while at the threshold coupling strength the energy gaps are sufficiently high to inhibit nonadiabatic transitions, but the barrier is low enough to allow all of the trajectories to reach the stable acceptor configuration. For $P_i = 10.0$ a.u., % PCET decreases gradually and then suddenly drops to zero, whereas for $P_i = 15.0$ a.u., % PCET decreases gradually up to a certain intermediate coupling strength, but then increases. In this case, there is no sudden drop to zero, since for $P_i = 15.0$ a.u. the system has sufficient kinetic energy to overcome the barrier. It should be noted that several points were omitted from the top panel of Fig. 2.11,

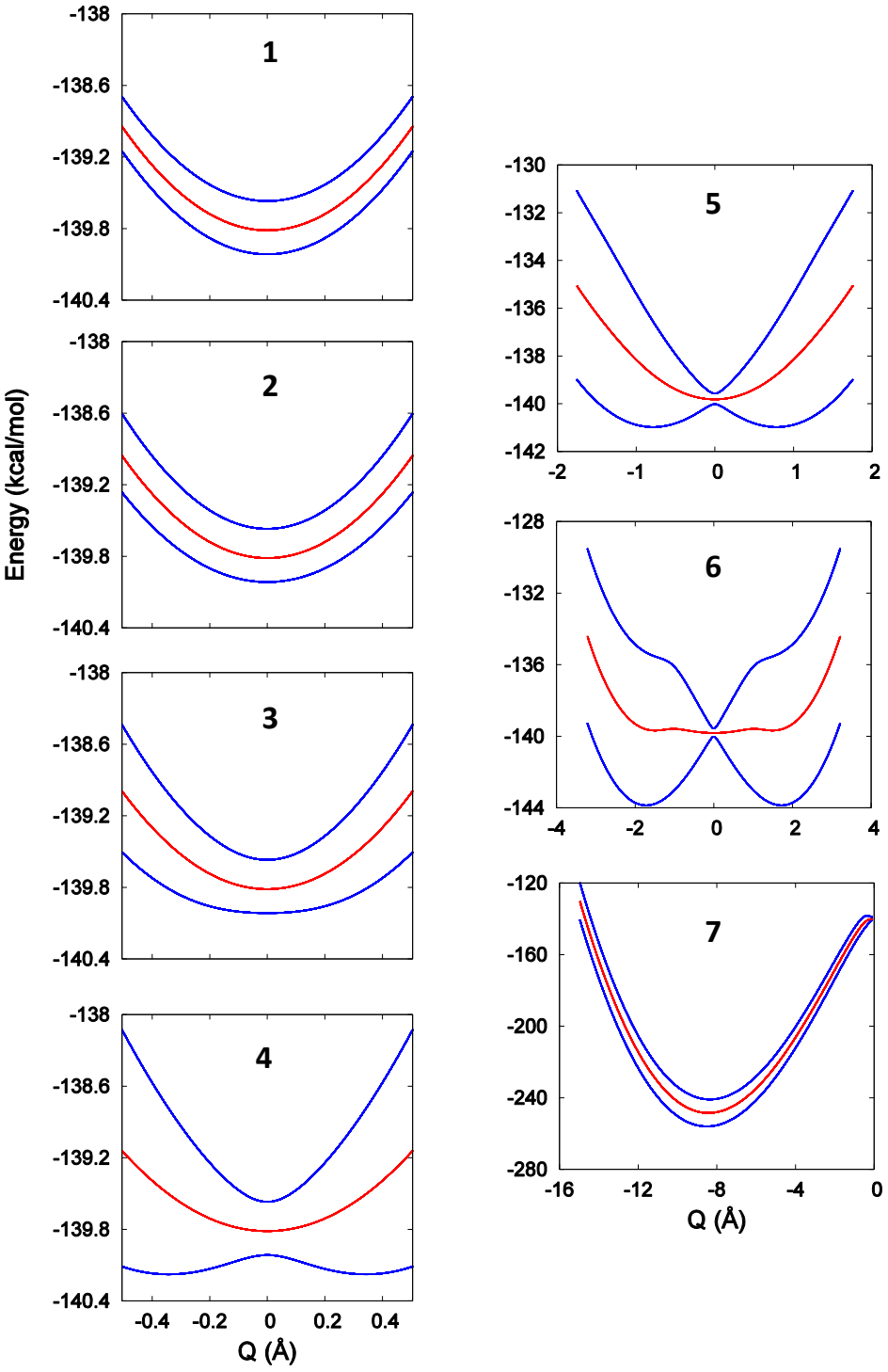

FIGURE 2.12: Adiabatic potential energy surfaces for the seven different proton/electron-solvent coupling strengths (listed in order of increasing strength from 1 to 7), computed for the concerted mechanism with $P_i = 10.0$ a.u. Note that for coupling strength 7, the reaction barrier is sufficiently high that the system remains in the donor state for this P_i.

since for these particular combinations of P_i and coupling strength the system gets "stuck" on the mean surface for a long time and, as a result, these trajectories could not terminate within a reasonable amount of time (for P_i =4.0 a.u./strength=3, 7.0 a.u./strength=3, 10.0 a.u./strength=6, and 15.0 a.u./strength=6, 374, 733, 711, and 957 trajectories terminated, respectively). In contrast, the percentage of successful adiabatic PCETs (see top panel of Fig. 2.13) is lower than % PCET for intermediate and high coupling strengths (except for the coupling strengths where the $P_i = 4.0$ and 7.0 a.u. percentages spike to 100% before dropping to zero). Therefore, the fact that % PCET is larger than the percentage of successful

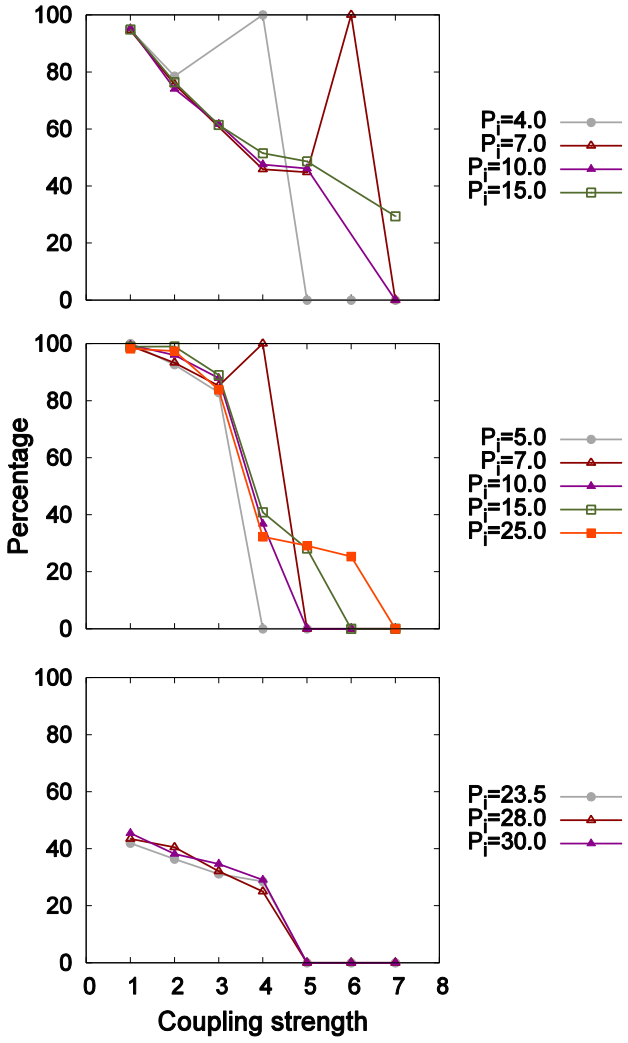

FIGURE 2.13: The percentage of trajectories which undergo adiabatic reaction as a function of the coupling strength between the proton/electron and the solvent for various initial momenta, P_i, for the concerted (top), sequential PT-ET (middle), and ET-PT (bottom) reactions. The $x-$axis labels $1-7$ denote seven sets of coupling constants $\{C_{sp}, C_{se}\}$, in order of increasing strength. The results were obtained using the MQCL surface-hopping method.

adiabatic PCETs is directly due to nonadiabatic transitions. Similar trends are observed in the case of PT-ET (see middle panel of Fig. 2.11). Here, we see that % PCET drops to zero for all initial momenta and the coupling strength at which the drop occurs increases with increasing initial momenta. The percentage of successful adiabatic PCETs is higher than % PCET for some low coupling strengths, but lower than % PCET for intermediate and higher coupling strengths (see middle panel of Fig. 2.13) than in the case of % PCET. This indicates that nonadiabatic transitions can play a dual role, inhibiting PCETs under low coupling conditions and enhancing them under higher ones. In the case of ET-PT (see bottom panel of Fig. 2.11), % PCET increases to a maximum value at a coupling strength of 4, followed by sudden drops to zero for all initial momenta considered. In stark contrast, the magnitudes of the percentages of successful adiabatic PCETs are much lower and gradually decrease as the coupling strength is increased for all values of the initial momentum considered (see bottom panel of Fig. 2.13). Thus, for this mechanism, these initial momenta, and these coupling strengths, nonadiabatic dynamics on the mean and excited state surfaces leads to a dramatic change in the reaction dynamics.

The effect of varying the coupling strength between the proton/electron and the solvent on $\langle \mathrm{Re}[\mathcal{W}(t)] \rangle$ (with the average calculated in the same fashion as in the previous subsection) is shown in Fig. 2.14. In all three mechanisms, higher coupling to the solvent leads to a faster initial decay of $\langle \mathrm{Re}[\mathcal{W}(t)] \rangle$, as expected, with a faster decay occurring for concerted PCET compared to the sequential PCETs. However, the rates and profiles of the decays are mechanism-dependent. For example, under low coupling conditions, a long-lived lower-frequency oscillation in $\langle \mathrm{Re}[\mathcal{W}(t)] \rangle$ is observed in the case of concerted PCET, while short-lived high-frequency oscillations are observed in the sequential PCETs. These plots demonstrate the sensitivity of the phase factor to the solvent dynamics in the various mechanisms and, hence, emphasize the importance of including this phase factor for a proper treatment of the decoherence in a wide range of ultrafast PCET reactions.

2.5 Concluding remarks

In this Chapter, we presented the first application of quantum-classical Liouville dynamics to the study of PCET. A minimal model of a condensed phase PCET reaction consisting

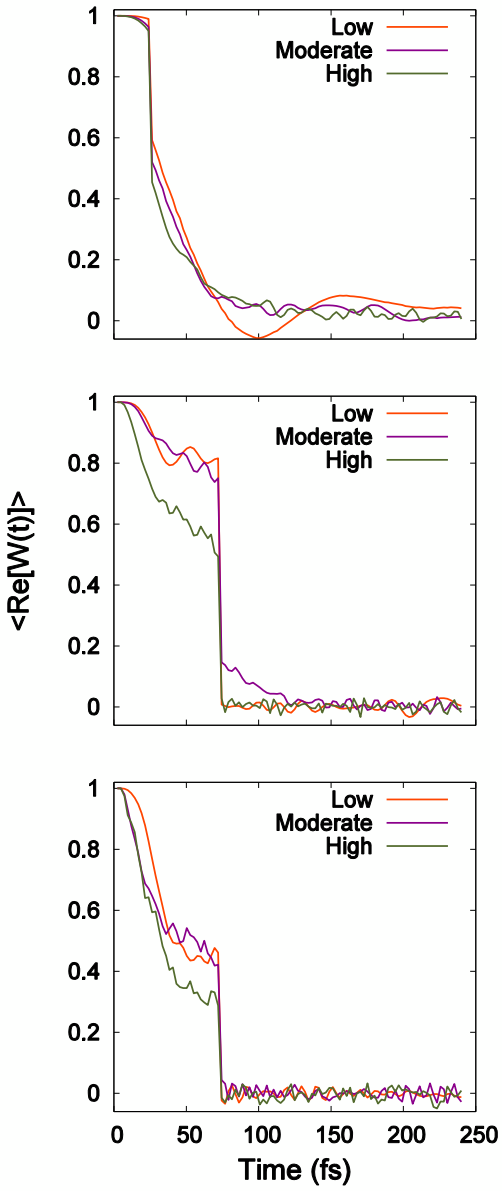

FIGURE 2.14: Average of the real part of $\mathcal{W}(t)$, $\langle \mathrm{Re}[\mathcal{W}(t)] \rangle$, over an ensemble of trajectories starting from Q_i =-0.24, -0.58, and -0.5 Å and an initial momentum distribution (corresponding to a temperature of 300 K) centred around $P_i = 10$, 10, and 28 a.u. for the concerted (top), PT-ET (middle), and ET-PT (bottom) reactions, respectively, calculated for three different sets of proton/electron-solvent coupling strengths.

of a proton, an electron, and a solvent coordinate was studied, which had been investigated previously using the FSSH method [90]. Varying the model's parameters allowed us to study both concerted and sequential PCET mechanisms under a wide range of subsystem-bath couplings. For each mechanism, we generated an ensemble of 1000 trajectories, starting from the same position of the solvent on the ground adiabatic state (corresponding to the

donor configuration) but different values of the momentum, to study the effect of increasing the momentum on the nonadiabatic dynamics. Successful PCETs end in the acceptor configuration (on the ground state in the case of concerted PCET and either the ground or excited state in the case of the sequential PCETs), occurring either adiabatically on the ground state or nonadiabatically after transitions between states.

In the case of concerted PCET, as the initial momentum is increased, the percentage of successful PCET reactions displays an initial decrease but then remains relatively constant. Except for the lowest initial momentum (viz., $P_i = 4.0$ a.u.), approximately half of these PCETs occur adiabatically and the other half nonadiabatically via primarily the following pathway: (1,1)→(1,2)/(2,1)→(1,1). Interestingly, for $P_i = 7.0$ a.u., the percentage of 4-jump trajectories is higher than for any other value of the initial momentum in any mechanism. In the case of PT-ET, increasing the initial solvent momentum beyond $P_i = 15.0$ a.u. leads to a higher % PCET since more nonadiabatic transitions from the (1,2)/(2,1) to the (1,1) and (2,2) surfaces occur outside of the barrier top region. As in the case of concerted PCET, the 0- and 2-jump reactive trajectories are the two main contributors. In the case of ET-PT, increasing the initial solvent momentum over the range of high initial momenta considered leads to an increase in the percentage of successful PCET reactions (to almost 100%). It also substantially increases the percentage of 4-jump reactions, at the expense of the adiabatic and 2-jump reactions. Overall, our results for % PCET drastically differ from those in Ref. 90 due to the fact that, regardless of the mechanism, large amounts of time are spent on the mean surface for all initial momenta. This underscores the importance of including the mean surface, (α, α'), in the nonadiabatic dynamics, especially when it is significantly different in character from the (α, α) and (α', α') surfaces. While on the mean surface, the observable in question (e.g., a rate constant) acquires a phase, which can lead to either constructive or destructive interference upon averaging over an ensemble of trajectories. For each PCET mechanism considered, we observed a different decay profile for the average of the real part of the phase factor, $\langle \mathrm{Re}[\mathcal{W}(t)] \rangle$, suggesting that coherence/decoherence effects may be important when studying ultrafast PCET processes and may vary from mechanism to mechanism.

We also investigated the effects of varying the coupling strength between the proton/electron and the solvent on % PCET and on $\langle \mathrm{Re}[\mathcal{W}(t)] \rangle$ for all three mechanisms. In the case of %

PCET, we found that both the weight and nature of the role played by nonadiabatic dynamics depends on the coupling strength, initial momentum, and the mechanism considered. For all mechanisms studied, % PCET suddenly drops to zero at high coupling strengths due to the emergence of high reaction barriers. In addition, in most cases, nonadiabatic transitions to the various surfaces facilitate PCETs, but in some cases they can inhibit PCETs. In the case of the phase factor, an increase in the coupling strength leads to a faster decay of $\langle \mathrm{Re}[\mathcal{W}(t)] \rangle$, with faster initial decays observed in concerted PCET than in the sequential ones. We also found that the rates and profiles of these decays are mechanism-dependent.

Given the more rigorous basis of the MQCL surface-hopping approach and the fact that it yields significantly different results than the FSSH approach for the minimal model considered in this study, the MQCL method could provide new insight into the nonadiabatic dynamics of a wide range of PCET reactions and, therefore, form the basis for future investigations of PCET reactions in more complex systems.

Chapter 3

New Insights into the Nonadiabatic State Population Dynamics of Model Proton-Coupled Electron Transfer Reactions from the Mixed Quantum-Classical Liouville Approach

3.1 Introduction

Over the years, experimental studies have focused on the thermodynamic and mechanistic aspects of PCET [3, 14, 18–23, 94–99]. Using stop-flow and flash-quench techniques combined with fluorescence, absorption, or EPR spectroscopies, reduction potentials under various pHs and solvent kinetic isotopes effect may be measured to determine the Gibbs free energy changes, rate constants, and equilibrium constants of these reactions. To gain theoretical insight into such quantities, on the other hand, the quantum nature of the transferring proton(s) and electron(s) and their interactions with the atoms and molecules in

their environment must be properly taken into account. Owing to the mass scale separation between these two sets of degrees of freedom (DOF), a mixed quantum-classical treatment of the reaction dynamics is appropriate. However, a proper treatment of the nonadiabatic effects in such systems is important for accurate calculations of PCET observables.

Hammes-Schiffer and co-workers have simulated PCET dynamics extensively [25–28] using the Fewest-Switches Surface Hopping (FSSH) method [100]. However, FSSH has been shown to yield inaccurate results due to its inability to treat decoherence [69, 72, 101]. This issue becomes especially pronounced under strong subsystem-bath coupling conditions [101]. Several improvements to FSSH have been made over the years, but they are ad hoc in nature [40, 41, 70, 71, 102–104]. In the second chapter of this thesis we developed an MQCL algorithm to study a model PCET reaction based on the fact that MQCL rigorously treats quantum coherence/decoherence effects. We showed that MQCL can yield qualitatively different results than FSSH for this model, under a variety of conditions. These differences were attributed to the fact that the MQCL trajectories spend the majority of their time on the mean surfaces. In light of this, we believe that the MQCL method will allow us to more accurately compute PCET rate constants and investigate ways of controlling PCET reactions.

Herein, we use MQCL-based surface hopping dynamics to calculate adiabatic state populations under different proton/electron−solvent coupling conditions for the same three-dimensional model studied in the second chapter of this thesis. A detailed description of the model, including the Hamiltonian and the necessary parameter values, were presented in the last chapter. The MQCL dynamics of an observable is presented in the next section, as well as the the details of the corresponding simulations in section 3. In section 4 of this chapter, which includes results and discussions, we first present the MQCL results for the time-dependent adiabatic state populations in a sequential version of the model, the ET-PT mechanism, and compare them to the available exact quantum and FSSH results [92]. Based on the agreement between MQCL and exact results, we then present the population results for the concerted PCET and sequential PT-ET versions of the model.[1] Finally, the concluding remarks will be made in section 5.

[1]The exact quantum and FSSH results are not available for these cases.

3.2 MQCL dynamics of an observable

The Hamiltonian of a mixed quantum-classical system, which is comprised of a quantum subsystem coupled to a classical environment, is given by

$$\hat{H}\left(Q,P\right) \;=\; \frac{P^2}{2M} + V_e(Q) + \frac{\hat{p}^2}{2m} + \hat{V}_s(\hat{q}) + \hat{V}_c(\hat{q},Q), \tag{3.1}$$

where m, $\hat{q}$, and $\hat{p}$ are the vectors of masses, positions, and momenta of the n quantum DOF, respectively; M, Q, and P are the vectors of masses, positions, and momenta of the N classical DOF, respectively; $\frac{P^2}{2M} + V_e$ is the environmental Hamiltonian and $\frac{\hat{p}^2}{2m} + \hat{V}_s$ is the subsystem Hamiltonian; and $\hat{V}_c$ is the subystem-environment coupling potential energy.

Quantum operators may be represented in an adiabatic basis, $\{|\alpha;Q\rangle\}$, which are the solutions of $\hat{h}(Q)|\alpha;Q\rangle = E_\alpha(Q)|\alpha;Q\rangle$, where $\hat{h} = \frac{\hat{p}^2}{2m} + \hat{V}_s + \hat{V}_c$. In this basis, the MQCL equation for the evolution of an observable $\hat{A}$ is [79]

$$\frac{\partial A_W^{\alpha\alpha'}(X,t)}{\partial t} = i\sum_{\beta\beta'} \mathcal{L}_{\alpha\alpha',\beta\beta'} A_W^{\beta\beta'}(X,t), \tag{3.2}$$

where $A_W^{\alpha\alpha'}(X,t)$ is the partial Wigner transform [89] of an observable $\hat{A}$, $X = (Q,P)$, and the QCL super-operator is given by

$$i\mathcal{L}_{\alpha\alpha',\beta\beta'} = (i\omega_{\alpha\alpha'} + iL_{\alpha\alpha'})\delta_{\alpha\beta}\delta_{\alpha'\beta'} - \mathcal{J}_{\alpha\alpha',\beta\beta'}. \tag{3.3}$$

In the above equation, $iL_{\alpha\alpha'}$ is the classical Liouville operator:

$$iL_{\alpha\alpha'} = \frac{P}{M}\cdot\frac{\partial}{\partial Q} + \frac{1}{2}\left(F_W^{\alpha} + F_W^{\alpha'}\right)\cdot\frac{\partial}{\partial P}. \tag{3.4}$$

When the quantum state indices are equal (i.e., $\alpha = \alpha'$), the classical evolution is carried out on a single adiabatic surface, $E_\alpha(Q)$, whereas when the quantum state indices are different (i.e., $\alpha \neq \alpha'$), the classical evolution is carried out on the mean of two adiabatic surfaces, $[E_\alpha(Q) + E_{\alpha'}(Q)]/2$, accompanied by quantum mechanical phase oscillations with frequency $\omega_{\alpha\alpha'} = (E_\alpha - E_{\alpha'})/\hbar$. The term $\mathcal{J}_{\alpha\alpha',\beta\beta'}$ is responsible for nonadiabatic transitions and the

associated changes in the momenta of the classical DOF, and is defined as

$$\mathcal{J}_{\alpha\alpha',\beta\beta'}(t) = -\frac{P}{M}\cdot d_{\alpha\beta}\left(1+\frac{1}{2}S_{\alpha\beta}\cdot\frac{\partial}{\partial P}\right)\delta_{\alpha'\beta'} - \frac{P}{M}\cdot d^{*}_{\alpha'\beta'}\left(1+\frac{1}{2}S^{*}_{\alpha'\beta'}\cdot\frac{\partial}{\partial P}\right)\delta_{\alpha\beta}, \tag{3.5}$$

where $S_{\alpha\beta} = F_W^{\alpha}\delta_{\alpha\beta} - F_W^{\alpha\beta}(\frac{P}{M}\cdot d_{\alpha\beta})^{-1} = E_{\alpha\beta}d_{\alpha\beta}(\frac{P}{M}\cdot d_{\alpha\beta})^{-1}$, where $F_W^{\alpha\beta}$ is the off-diagonal matrix element of the force and $d_{\alpha\beta} = \langle\alpha;Q|\frac{\partial}{\partial Q}|\beta;Q\rangle$ is the nonadiabatic coupling matrix element.

Within the MQCL formalism, the expectation value of an observable $\hat{A}(t)$ is given by

$$\overline{A(t)} = \sum_{\alpha\alpha'}\int dX A_W^{\alpha\alpha'}(X,t)\rho_W^{\alpha'\alpha}(X), \tag{3.6}$$

where $\rho_W^{\alpha'\alpha}(X)$ is the Wigner transform of the density operator. $\overline{A(t)}$ may be calculated using the sequential short-time propagation (SSTP) algorithm, which provides a numerical solution of the MQCL equation [83, 84]. This algorithm generates an ensemble of surface-hopping trajectories, containing segments in which the classical DOF evolve either on single adiabatic surfaces (α,α) or on the mean of two surfaces (α,α') [where $\alpha \neq \alpha'$]. These segments are interspersed with nonadiabatic transitions, which cause the classical DOF to hop to a new surface (or mean surface), followed by evolution on this surface. We note that, according to the algorithm, only one state index in the pair (α,α') changes in any given nonadiabatic transition.

3.3 Simulation details

The general form of the PCET model Hamiltonian considered in this study is given by

$$\begin{aligned}\hat{H} &= \hat{K}_p + \hat{K}_e + K_s + \hat{V}_p(\hat{q}_p) + \hat{V}_e(\hat{q}_e) + \hat{V}_{pe}(\hat{q}_p,\hat{q}_e) + \hat{V}_{pes}(\hat{q}_p,\hat{q}_e,Q) + V_s(Q)\\ &\equiv \hat{h} + K_s + V_s(Q),\end{aligned} \tag{3.7}$$

where $\hat{V}_p$ and $\hat{V}_e$ denote the protonic and electronic potential energy operators, respectively, $\hat{V}_{pe}$ is the potential energy operator corresponding to the Coulombic interaction between the proton and electron, $V_s(Q)$ is a harmonic potential corresponding to the classical solvent

coordinate, $\hat{V}_{pes}$ is a bilinear potential corresponding to the coupling between the solvent coordinate and the proton-electron subsystem, $\hat{K}_p$ and $\hat{K}_e$ denote the kinetic energy operators of the proton and electron, respectively, K_s is the kinetic energy of the solvent coordinate, and $\hat{h} = \hat{H} - K_s - V_s$. The detailed forms of the potential energy terms may be found in the second chapter of this thesis as well as Refs. 17 and 90.

In this study, we adopt a substantially more efficient approach for solving the time-independent Schrödinger equation, $\hat{h}|\alpha;Q\rangle = E_\alpha(Q)|\alpha;Q\rangle$, than in our first study [17]. For the first time step of the simulation, the equation is solved by expanding an adiabatic wave function $|\alpha;Q\rangle$ in an orthonormal set of two-particle basis functions:

$$|\alpha;Q\rangle = \sum_{m,n} c^{\alpha}_{mn}|\phi_{p(m)}\rangle|\phi_{e(n)}\rangle, \tag{3.8}$$

where $|\phi_{p(m)}\rangle$ and $|\phi_{e(n)}\rangle$ are one-particle basis functions that are taken to be the solutions of the quantum harmonic oscillator for a proton and an electron, respectively, i.e.,

$$\phi_{p(m)}(q_p) = \langle q_p|\phi_{p(m)}\rangle = (2^m m!\sqrt{\pi})^{-1/2}\alpha_p^{1/2}e^{-\alpha_p^2(q_p-q_p^o)/2}H_m(\alpha_p(q_p-q_p^o)), \tag{3.9}$$

and

$$\phi_{e(n)}(q_e) = \langle q_e|\phi_{e(n)}\rangle = (2^n n!\sqrt{\pi})^{-1/2}\alpha_e^{1/2}e^{-\alpha_e^2(q_e-q_e^o)/2}H_n(\alpha_e(q_e-q_e^o)), \tag{3.10}$$

where q_p and q_e are the protonic and electronic coordinates, respectively, m and n are integers and $H_m(q)$ is the m^{th} Hermite polynomial. We have found that the range $0 < \{m,n\} < 24$ (which gives rise to 625 two-particle basis functions) is sufficient for convergence, with the one-particle protonic and electronic functions centred at q_p^o and q_e^o (which are both equal to 1.58 Å for the concerted mechanism and to 2.12 Å for the sequential mechanisms), and $\alpha_p = 3.97$ Å^{-1} and $\alpha_e = 0.32$ Å^{-1}. The $hc = cE$ eigenvalue problem is solved for the $\{c^{\alpha}_{mn}\}$ and $\{E_\alpha\}$ by diagonalizing the 625×625 Hamiltonian with matrix elements $h_{\{ij\}\{kl\}} = \langle\phi_{p(i)}\phi_{e(j)}|\hat{h}(Q)|\phi_{p(k)}\phi_{e(l)}\rangle$. The matrix elements $h_{\{ij\}\{kl\}}$ are calculated using the trapezoid rule with 100 points evenly spaced over the range $q_p = 1.06/1.59$ Å to $q_p = 2.12/2.65$ Å for the protonic integrals in the case of the concerted/sequential mechanisms and 700 points over the range $q_e = -3.17$ Å to $q_e = 6.35$ Å for the electronic integrals in the case of all mechanisms. For the next time step, the 17 lowest-energy adiabatic states are used as the

basis functions, while at each subsequent time step, the 17 updated adiabatic states are used as the basis functions. We have performed tests to ensure that this smaller basis set is sufficient for convergence.

The quantum subsystem is initially in the ground state and the initial positions and momenta of the classical solvent coordinate are sampled from the following Wigner distribution:

$$\rho_W(X) \propto \exp\left[-2\alpha(Q-Q_o)^2 - \frac{(P-P_o)^2}{2\hbar^2\alpha}\right], \tag{3.11}$$

where $\alpha = 25$ a.u. was used for all simulations in this study to allow for a direct comparison with the FSSH and exact results in Ref. 92. This corresponds to Gaussian distributions with standard deviations $\sigma_Q = (4\alpha)^{-\frac{1}{2}}$ and $\sigma_P = (\alpha\hbar^2)^{\frac{1}{2}}$. For the ET-PT, PT-ET, and concerted PCET mechanisms, ensembles of 2×10^7, 5×10^6, and 2×10^6 trajectories, respectively, were propagated from these initial conditions. For the first time step, the nonadiabatic coupling matrix elements of this model are calculated according to

$$\begin{aligned} d_{\alpha\beta} &= \frac{-1}{\Delta E_{\alpha\beta}}\langle\alpha;Q|\frac{\partial\hat{h}}{\partial Q}|\beta;Q\rangle \\ &= \frac{1}{\Delta E_{\alpha\beta}}\sum_{mnkl} c^{\alpha}_{mn}c^{\beta}_{kl}[C_{sp}\langle\phi_{p(m)}|(q_p-q_p^o)|\phi_{p(k)}\rangle\delta_{nl} + C_{se}\langle\phi_{e(n)}|(q_e-q_e^o)|\phi_{e(l)}\rangle\delta_{mk}], \end{aligned} \tag{3.12}$$

and the Hellmann-Feynman forces, F^{α}_W, are calculated using

$$\begin{aligned} F^{\alpha}_W &= -\langle\alpha;Q|\frac{\partial\hat{h}(Q)}{\partial Q}|\alpha;Q\rangle \\ &= \sum_{mnkl} c^{\alpha}_{mn}c^{\alpha}_{kl}[C_{sp}\langle\phi_{p(m)}|(q_p-q_p^o)|\phi_{p(k)}\rangle\delta_{nl} + C_{se}\langle\phi_{e(n)}|(q_e-q_e^o)|\phi_{e(l)}\rangle\delta_{mk}]. \end{aligned} \tag{3.13}$$

For each subsequent time step, the $|\phi_p\rangle$'s and $|\phi_e\rangle$'s in Eqs. 3.12 and 3.13 are replaced with the 17 lowest-energy adiabatic states from the previous time step. The classical solvent coordinate is propagated using the velocity-Verlet algorithm with a time step of 2.4 fs.

In this study, we calculate the time-dependent adiabatic state populations and coherences between two different adiabatic states α and α'. Therefore, the operators of interest are the projection operator corresponding to adiabatic state α,

$$\hat{P}_{\alpha}(t) = |\alpha;Q\rangle\langle\alpha;Q|, \tag{3.14}$$

and the off-diagonal operator

$$\hat{C}_{\alpha\alpha'}(t) = |\alpha; Q\rangle\langle\alpha'; Q|, \tag{3.15}$$

respectively. The expectation values of the various $\hat{P}_\alpha(t)$'s and $\hat{C}_{\alpha\alpha'}(t)$'s are calculated according to Eq. 3.6 using the SSTP algorithm, with $\hat{A}(t) = \hat{P}_\alpha(t)$ and $\hat{A}(t) = \hat{C}_{\alpha\alpha'}(t)$, respectively. To facilitate the convergence of the expectation values, we restrict the occurrence of nonadiabatic transitions to regions where the nonadiabatic coupling matrix elements have relatively large values. In addition, preliminary calculations have shown that the fourth adiabatic state is rarely populated, so we restrict our simulations to the three lowest states. For the ET-PT calculations, we apply an observable-cutting filter [84] to reduce the statistical fluctuations.

In the case of the ET-PT mechanism, we also investigate the dynamical effects of varying the strength of the coupling between the solvent coordinate and the proton/electron, which has a bilinear form given by

$$V_{pes}(q_p, q_e, Q) = -C_{sp}(Q - Q_p^o)(q_p - q_p^o) - C_{se}(Q - Q_e^o)(q_e - q_e^o), \tag{3.16}$$

where C_{sp}/C_{se} are the parameters representing the strength of the coupling between the proton/electron and the solvent coordinate. Specifically, we consider three different sets of $\{C_{sp}, C_{se}\}$ values, which are listed in Table I in increasing order of strength from I to III.

TABLE 3.1: Three sets of proton/electron-solvent coupling constants (i.e., $\{C_{sp}, C_{se}\}$) for the ET-PT mechanism. All values are in atomic units.

	I	II	III
C_{sp}	1.5×10^{-2}	2.2×10^{-2}	3×10^{-2}
C_{se}	2×10^{-3}	3×10^{-3}	4×10^{-3}

3.4 Results and discussion

3.4.1 Sequential ET-PT mechanism

3.4.1.1 Potential energy surfaces and nonadiabatic couplings

The upper panel of Fig. 3.1 illustrates the ground (1,1), first excited (2,2), and second excited (3,3) state adiabatic potential energy surfaces (PESs) and the corresponding mean surfaces [(1,2) or (2,1)], [(1,3) or (3,1)], and [(2,3) or (3,2)] as a function of the solvent coordinate for the sequential ET-PT mechanism and the set III coupling constants. For the sake of brevity, we refer to the mean surfaces as (1,2), (1,3), and (2,3), respectively, within the text. The minimum energy gap between the (1,1) and (2,2) surfaces is 0.46 kcal/mol, occurring

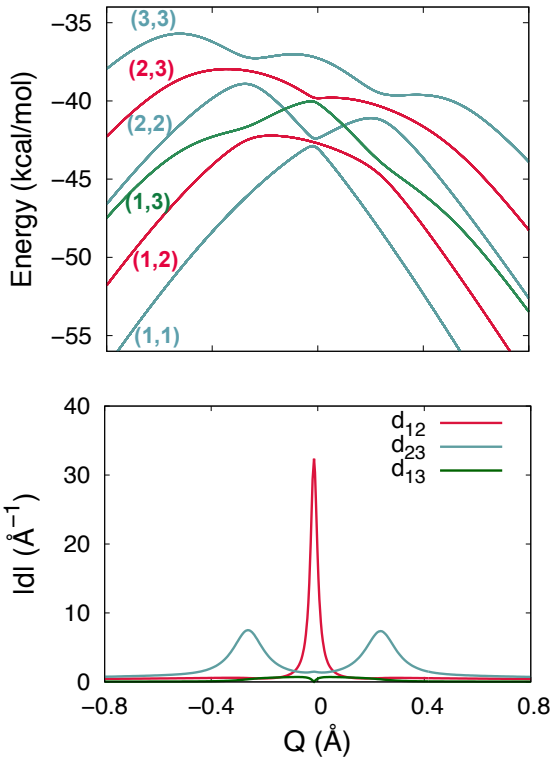

FIGURE 3.1: Top panel: Ground (1,1), first excited (2,2), and second excited (3,3) state adiabatic PESs as a function of the solvent coordinate, Q, for the ET-PT model. The blue curves correspond to these surfaces, the red curves correspond to the mean surfaces between adjacent surfaces, and the green curve corresponds to the mean surface between the ground and second excited state surfaces. Bottom panel: Absolute values of the nonadiabatic coupling matrix elements, $|d_{12}|$, $|d_{23}|$, and $|d_{13}|$ as a function of the solvent coordinate, Q.

at $Q = -0.02$ Å. The minimum energy gaps between the (2,2) and (3,3) surfaces are 1.72

and 1.62 kcal/mol, occurring at $Q = -0.26$ Å and $Q = 0.24$ Å, respectively. These three gaps correspond to regions where nonadiabatic transitions are most probable, as confirmed by the plots of the nonadiabatic coupling matrix elements versus the solvent coordinate in the lower panel of Fig. 3.1. As seen in this figure, the absolute value of the nonadiabatic coupling between the (1,1) and (2,2) states, $|d_{12}|$, is peaked at the Q value corresponding to the ground state barrier top where the energy gap between the (1,1) and (2,2) surfaces is the smallest. Similarly, the absolute value of the nonadiabatic coupling between the (2,2) and (3,3) states, $|d_{23}|$, contains two peaks that flank the $|d_{12}|$ peak (albeit with lower intensities) at the Q values corresponding to the minimum energy gaps between the (2,2) and (3,3) surfaces. The (1,1) and (3,3) surfaces are well-separated in energy for all solvent configurations, resulting in small values of $|d_{13}|$ (see lower panel of Fig. 3.1). However, due to the relatively large $|d_{12}|$ and $|d_{23}|$ values at $Q = -0.02$ Å and $Q = -0.26/0.24$ Å, respectively, the dynamics on the (1,3) surface is expected to facilitate the population transfer between the ground and second excited states through the following sequence of nonadiabatic transitions: (1,1)→(1,2)→(1,3)→(2,3)→(3,3). By construction, the mean surfaces exhibit features of the adiabatic PESs comprising them. The (1,2) mean surface has a broad, asymmetric barrier top which slants downwards towards product configurations. By contrast, the (2,3) surface has two humps, located at the minimum energy gaps between the (2,2) and (3,3) surfaces, separated by a shallow well at $Q = -0.02$ Å. The (1,3) mean surface (depicted in green) has a barrier top at $Q = -0.02$ Å, with two shallow depressions on either side of it.

3.4.1.2 Time-dependent state populations and coherences

To calculate the time-dependent state populations using Eqs. 3.6 and 3.14, an ensemble of 2×10^7 trajectories was generated using the set III coupling constants, starting from initial conditions sampled from the Wigner distribution in Eq. 3.11 with $Q_o = -0.5$ Å and $P_o = 23.5$ a.u. The time evolution of the populations of the three lowest adiabatic states out to 7000 a.u., calculated via the MQCL method (red), is shown in Fig. 3.2. For comparison, the FSSH (green) and fully quantum (blue) results from Ref. 92 are also shown in this figure. As can be seen, the agreement between the MQCL and fully quantum results for all states is almost perfect till ∼1500 a.u. Between ∼1500 a.u. and ∼3500 a.u., the MQCL and fully quantum results are in good (but not perfect) agreement, while for the remainder of the

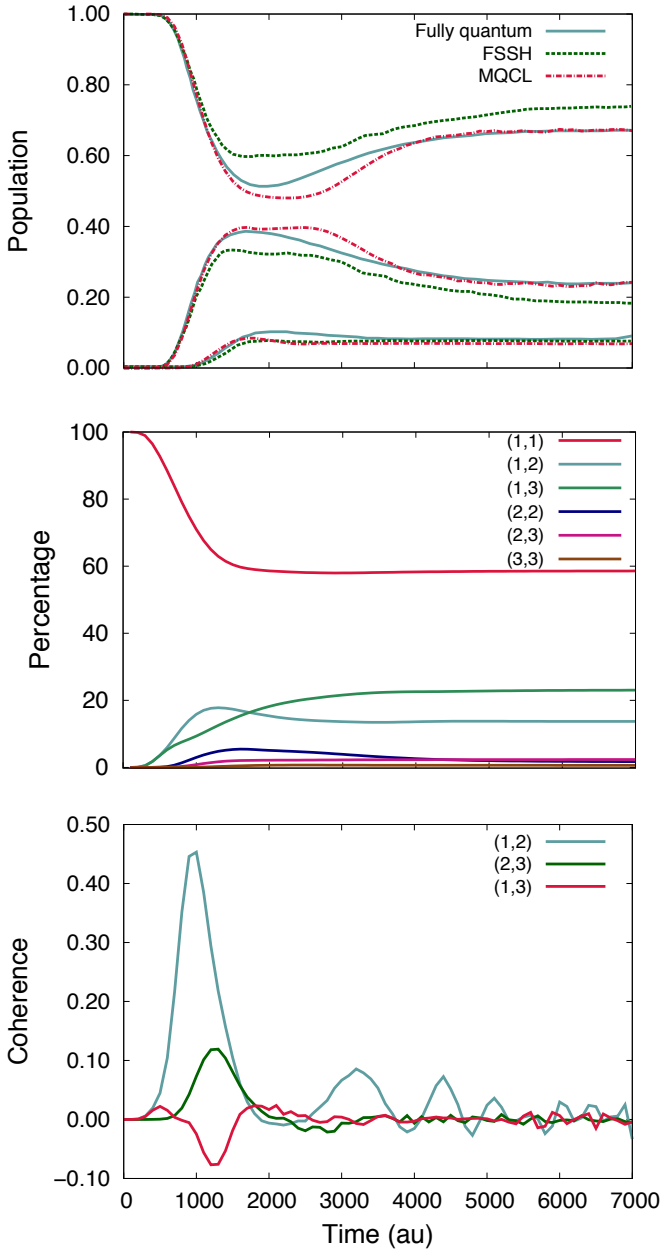

FIGURE 3.2: Top panel: Time evolutions of the populations of the ground (1,1), first-excited (2,2), and second-excited (3,3) adiabatic states for the ET-PT model, calculated via MQCL, FSSH, and exact quantum dynamics. Middle panel: The percentage of trajectories on each surface as a function of time. Bottom panel: Time evolutions of the (1,2), (2,3), and (1,3) coherences, calculated via MQCL.

time, the agreement is almost perfect again. The slight deviation between the MQCL and fully quantum results in the range of $1500 - 3500$ a.u. may stem from the fact that the solvent often resides in the region of strong nonadiabatic coupling between the ground and first excited state (around $Q = -0.02$ Å) during this period, thereby making it difficult for

MQCL to generate the exact values. As seen in Fig. 3.2, many trajectories evolve on the (1,2) and (1,3) mean surfaces during this period, which causes the observable to acquire a phase $\mathcal{W}(t) = e^{i\int_0^t \omega_{12}(t')dt'}$ in time. As can be seen, MQCL shows a significant overall improvement over FSSH in capturing the exact population dynamics in this PCET model. Given the high level of agreement between the MQCL and exact quantum results, we later present and discuss the results of the time-dependent populations for models exhibiting sequential PT-ET and concerted PCET mechanisms.

To gain insight into the participation of the various surfaces in the population dynamics, we present the percentage of trajectories in the ensemble on each surface as a function of time. The results out to 7000 a.u. are shown in the middle panel of Fig. 3.2. Starting from the (1,1) surface, the trajectories begin to hop to the (1,2) and (1,3) mean surfaces within ∼250 a.u. At ∼600 a.u., the increasing percentages of trajectories on these surfaces begin to deviate as some trajectories hop to the (2,2) and (2,3) surfaces. Ultimately, the majority of trajectories end up on the (1,1), (1,2), and (1,3) surfaces, giving rise to plateaus at 59%, 13%, and 22%, respectively. Interestingly, *coherence transfer* is observed as the (2,3) percentage increases at the expense of the (1,3) percentage (at ∼600 a.u.) and the (1,2) percentage decreases at the gain of the (1,3) percentage (at ∼1500 a.u.). The percentage of trajectories on the (2,2) surface reaches its maximum at ∼1500 a.u., followed by a gradual decrease for the remainder of the time. This is likely due to downward nonadiabatic transitions from (2,2) to (1,2), which in turn leads to a larger number of downward transitions from (1,2) to (1,1) relative to upward ones from (1,1) to (1,2) and thereby increase/decrease the (1,1)/(2,2) population. Overall, these results underscore the importance of mean surface dynamics in the evolution of the state populations.

Using the same ensemble, we also calculated the time-dependent (1,2), (1,3), and (2,3) coherences using Eqs. 3.6 and 3.15. As can be seen in the bottom panel of Fig. 3.2, the (1,2) coherence exhibits the largest magnitude and is the most long-lived, exhibiting pronounced oscillations over the whole time period considered. The smaller (1,3) and (2,3) coherences decay to zero in ∼3000 a.u. These results underscore the importance of coherent dynamics in the calculations of observables on sub-picosecond timescales.

3.4.1.3 Effect of proton/electron-solvent coupling strength

The effect of reducing the subsystem-solvent coupling strength on the ground, first excited, and second excited state PESs (and their corresponding mean surfaces) is shown in Fig. 3.3. Two different sets of the coupling constants are considered: $C_{sp} = 1.5\times10^{-2}/C_{se} = 2.0\times10^{-3}$ (i.e. weakest) and $C_{sp} = 2.2 \times 10^{-2}/C_{se} = 3.0 \times 10^{-3}$ (i.e. intermediate). For comparison, we also show the results for the strongest coupling case considered in the previous sections. In the strongest coupling case, highly stable reactant and product wells exist on all surfaces, with energy barriers exceeding 100 kcal/mol (see top left panel of Fig. 3.3). Upon decreasing the coupling constants to the intermediate values, we see a drastic destabilization of the reactant and product wells on all surfaces (see middle left panel of Fig. 3.3). In the weakest coupling case, this destabilization is even more pronounced, such that the reactant and product wells on the (2,3) and (3,3) surfaces disappear (see bottom left panel of Fig. 3.3). In the right-hand panels of Fig. 3.3, we zoom in on the regions of the surfaces around $Q = 0$ Å. Notably, in going from the strongest to the weakest coupling case, the (1,2) surface becomes flatter, the distance between the locations of the minimum energy gaps between the (2,2) and (3,3) surfaces increases, and there is an overall compression of the surfaces. Thus, given the drastic changes in the shapes of surfaces upon decreasing the coupling constants, we expect the nonadiabatic population dynamics to vary drastically.

The effect of varying the subsystem-solvent coupling strength on the nonadiabatic coupling matrix elements is shown in Fig. 3.4. As can be seen, the peak heights and widths of all three matrix elements decrease and increase, respectively, as the subsystem-solvent coupling strength decreases. Moreover, in the case of $|d_{23}|$, the inter-peak distance increases with decreasing coupling strength. Therefore, decreasing the coupling strength decreases the probability of nonadiabatic transitions for solvent configurations giving rise to the minimum energy gaps between adiabatic PESs. However, the range of solvent configurations over which nonadiabatic transitions have non-negligible transition probabilities becomes wider with decreasing coupling strength.

The time evolution of the populations of the three lowest adiabatic states, calculated via the MQCL method, for the three subsystem-solvent cases are shown in Fig. 3.5. In going from strongest to intermediate coupling, we see a drastic increase in the (2,2) population at the expense of the (1,1) population, despite the decrease in $|d_{12}|$ at the barrier top.

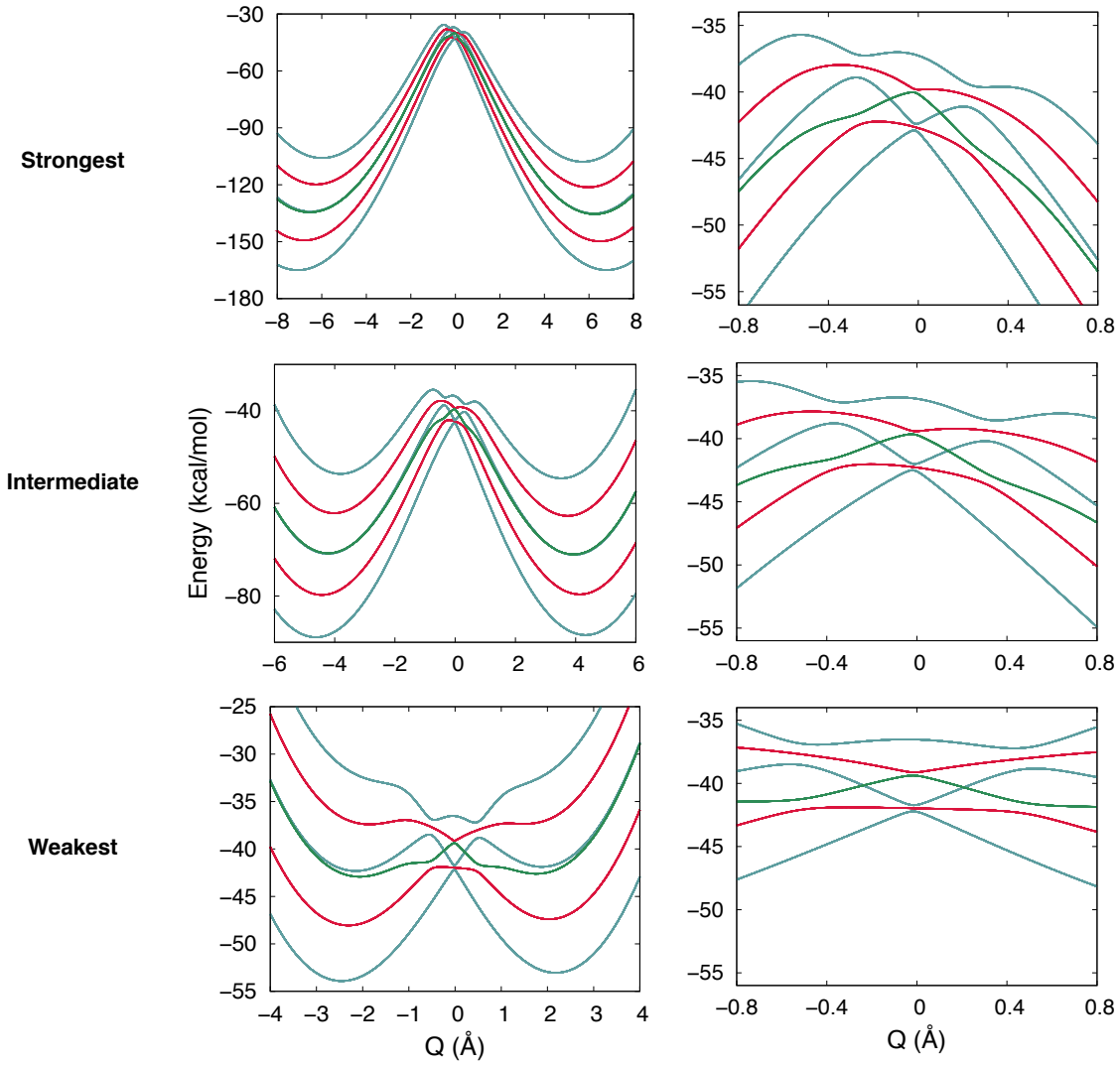

FIGURE 3.3: Left panels: Ground (1,1), first excited (2,2), and second excited (3,3) state adiabatic PESs as a function of the solvent coordinate, Q, for the ET-PT model, corresponding to different proton/electron-solvent coupling strengths: $C_{sp} = 1.5 \times 10^{-2}/C_{se} = 2.0 \times 10^{-3}$ (weakest), $C_{sp} = 2.2 \times 10^{-2}/C_{se} = 3.0 \times 10^{-3}$ (intermediate), and $C_{sp} = 3.0 \times 10^{-2}/C_{se} = 4.0 \times 10^{-3}$ (strongest). The blue curves correspond to the (1,1), (2,2), and (3,3) surfaces, the red curves correspond to the mean surfaces between adjacent surfaces, and the green curve corresponds to the mean surface between the ground and second excited state surfaces. Right panels: Close-ups of the surfaces around $Q = 0$ Å.

However, as mentioned previously, the range of reactant solvent configurations over which nonadiabatic transitions have non-negligible transition probabilities becomes wider than in the strongest coupling case, which leads to an increased number of nonadiabatic transitions to the (2,2) surface through the (1,2) surface. In addition, due to the wider and flatter nature of the (1,2) surface, the solvent coordinate can spend more time on this surface resulting in more pronounced phase oscillations in the (2,2) population than in the strongest

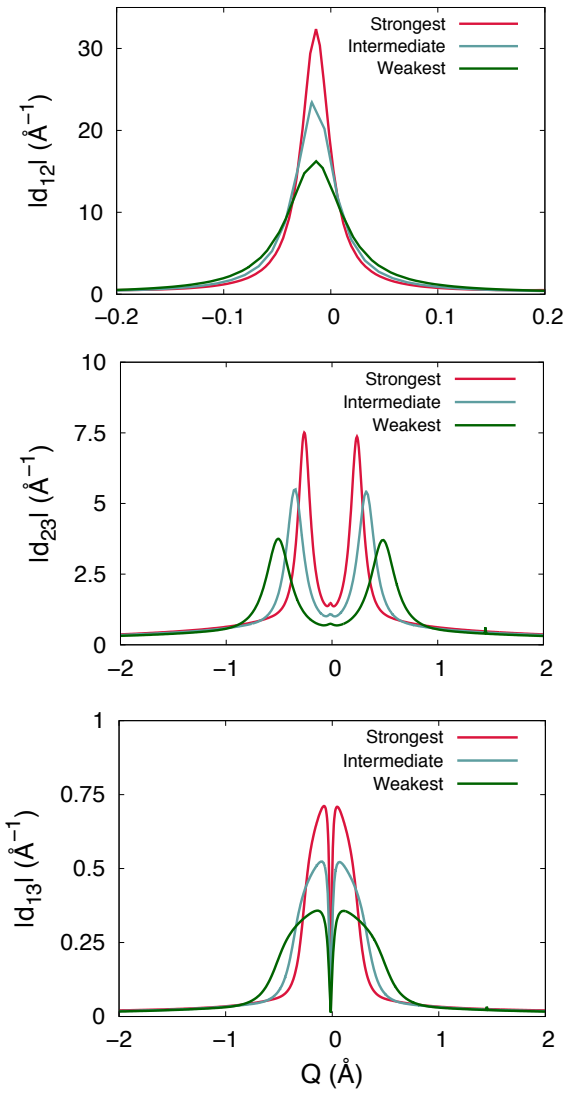

FIGURE 3.4: Absolute values of the nonadiabatic coupling matrix elements $|d_{12}|$ (top panel), $|d_{23}|$ (middle panel), and $|d_{13}|$ (bottom panel), as a function of the solvent coordinate, Q, for the ET-PT model, corresponding to different proton/electron-solvent coupling strengths: $C_{sp} = 1.5 \times 10^{-2}/C_{se} = 2.0 \times 10^{-3}$ (weakest), $C_{sp} = 2.2 \times 10^{-2}/C_{se} = 3.0 \times 10^{-3}$ (intermediate), and $C_{sp} = 3.0 \times 10^{-2}/C_{se} = 4.0 \times 10^{-3}$ (strongest).

coupling case. Eventually, these oscillations dampen out due to decoherence. At ∼3100 a.u., the (2,2) population begins to decrease at the expense of an increasing (1,1) population, decreasing more than in the strongest coupling case due to the wider $|d_{12}|$ profile. In the lowest coupling case, there is an almost complete population reversal between the ground and first excited state within ∼1500 a.u. due to a further increase in the range of reactant solvent configurations over which nonadiabatic transitions have non-negligible $1 \rightarrow 2$ transition probabilities. Finally, despite the major differences in the (1,1) and (2,2) populations, the

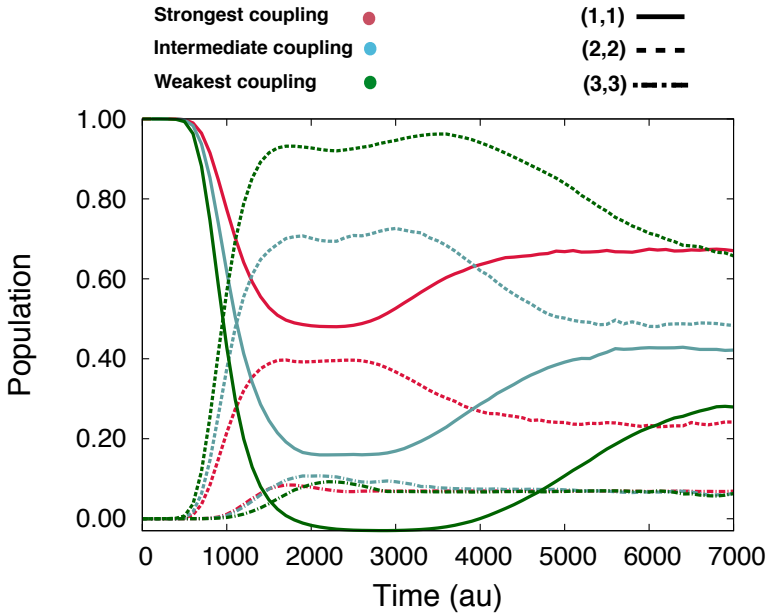

FIGURE 3.5: Time evolutions of the populations of the ground (1,1), first excited (2,2), and second excited (3,3) adiabatic states for the ET-PT model, calculated via MQCL, corresponding to different proton/electron-solvent coupling strengths: $C_{sp} = 1.5 \times 10^{-2}/C_{se} = 2.0 \times 10^{-3}$ (weakest), $C_{sp} = 2.2 \times 10^{-2}/C_{se} = 3.0 \times 10^{-3}$ (intermediate), and $C_{sp} = 3.0 \times 10^{-2}/C_{se} = 4.0 \times 10^{-3}$ (strongest).

differences between the (3,3) populations in the three cases are quite minor.

3.4.2 Sequential PT-ET mechanism

3.4.2.1 Potential energy surfaces and nonadiabatic couplings

We next consider the sequential PT-ET mechanism with coupling constants $C_{sp} = 1 \times 10^{-2}$ and $C_{se} = 2 \times 10^{-3}$, which are the same as those used in Refs. 17 and 90 for studying PT-ET and are very similar to the set I coupling constants used herein for ET-PT. The corresponding PESs are shown in the top panel of Fig. 3.6. Owing to the similarity of the coupling constants to those of the set I ET-PT case, the corresponding PESs have similar overall profiles, although there are differences in the relative heights of the energy barriers on the various surfaces and the values of the solvent coordinate corresponding to the wells. For example, the ground state reaction barrier is only ∼4 kcal/mol, compared to ∼11 kcal/mol in the ET-PT case, and is not centered at the midpoint between the donor and the acceptor as in the ET-PT case (i.e. at $Q = 0.0$ Å), but rather at $Q = -0.46$ Å. There is a well on the (2,2) surface centered at $Q = -0.46$ Å, giving rise to a minimum energy gap of 0.33 kcal/mol

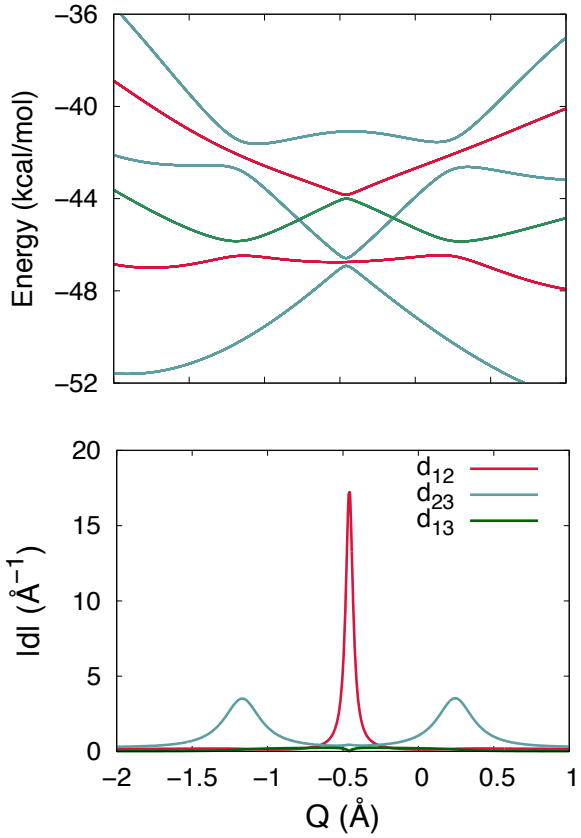

FIGURE 3.6: Top panel: Ground (1,1), first excited (2,2), and second excited (3,3) state adiabatic PESs as a function of the solvent coordinate, Q, for the PT-ET model. The blue curves correspond to these surfaces, the red curves correspond to the mean surfaces between adjacent surfaces, and the green curve corresponds to the mean surface between the ground and second excited state surfaces. Bottom panel: Absolute values of the nonadiabatic coupling matrix elements, $|d_{12}|$, $|d_{23}|$, and $|d_{13}|$ as a function of the solvent coordinate, Q.

with the (1,1) surface. At $Q = -1.16$ and 0.25 Å, there are two minimum energy gaps between the (2,2) and (3,3) surfaces of ∼1.25 kcal/mol. The (1,2) surface is rather flat over the range of solvent configurations depicted, while the (2,3) surface has a parabolic shape. However, in contrast to the set I ET-PT case, the (1,2) surface possesses a very shallow well, which can trap the solvent coordinate in the barrier top region while on this surface and thereby increase the incidence of (2,2)→(1,2)→(1,1) transitions with respect to the ET-PT case. Similar to in ET-PT, the (1,3) surface bridges the (1,2) and (2,3) surfaces, creating a pathway for nonadiabatic transitions to the second excited state.

The nonadiabatic coupling matrix elements as a function of the solvent coordinate are presented in the bottom panel of Fig. 3.6. They are similar in shape and magnitude to what is observed in the ET-PT (weakest coupling) case, including a large $|d_{12}|$ peak, two smaller

$|d_{23}|$ peaks, and two very small $|d_{13}|$ peaks. As expected, the main difference is in the locations of the peak maxima. Therefore, for this set of coupling constants, one can expect state population profiles for PT-ET that are qualitatively similar to those seen in the weakest coupling case of ET-PT.

3.4.2.2 Time-dependent state populations and coherences

The time-dependent populations of the three lowest adiabatic states are shown in the top panel of Fig. 3.7. They were calculated using an ensemble of 5×10^6 trajectories starting from initial conditions sampled from the Wigner distribution in Eq. 3.11 with $Q_o = -0.58$ Å and $P_o = 15$ a.u. As can be seen, the (1,1) population drops abruptly (within ∼1200 a.u.) to ∼10%, while the (2,2) population rises to ∼90% during this time. However, at ∼2500 a.u., the (1,1)/(2,2) population begins to increase/decrease due to nonadiabatic transitions back down to the ground state. By the end of the simulation, the (1,1) population is substantially higher than the (2,2) population (75% vs. 20%, respectively). The (3,3) population begins to rise at ∼1500 a.u., but remains very small (∼3%). These populations should be contrasted with those in the ET-PT (weakest coupling) case, which exhibit a similar population reversal initially but, at later times, the (1,1) population is substantially lower than the (2,2) population (28% vs. 67%, respectively). This difference is likely due to the fact that, in the PT-ET case, the (1,2) surface possesses a very shallow well, which can lead to a larger number of (2,2)→(1,2)→(1,1) transitions compared to the ET-PT case.

In the middle panel of Fig. 3.7, we plot the percentage of trajectories in the ensemble on each surface as a function of time. We see that the percentage of trajectories on (1,1) immediately starts to decrease (since the solvent coordinate is initialized in a strong nonadiabatic coupling region), dropping to ∼35% in ∼1200 a.u, and continues to grow slightly over the remaining time. The percentage of trajectories on (1,2) increases to ∼44% during the first ∼800 a.u., exceeding the percentage of trajectories on (1,1) and the percentage of trajectories on (1,2) in the ET-PT case, and continues to grow slightly over the remaining time. This should be contrasted with the set I ET-PT case, in which the percentage of trajectories on (1,1) decreases to ∼26% in ∼1800 a.u., and the percentage of trajectories on (1,2) increases to ∼32% during the first ∼1200 a.u. (see Fig. 3.8 for the set I ET-PT percentages). This difference in the times is mainly due to the fact that $Q_0 = -0.58$Å (which is close to the value

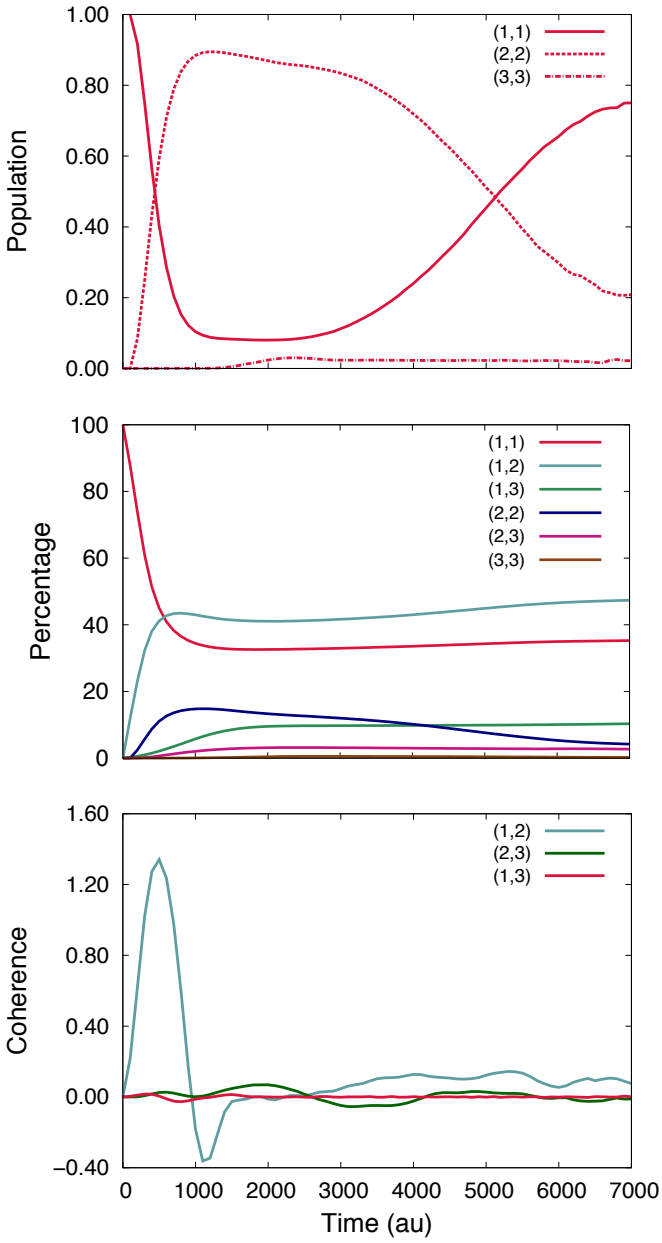

FIGURE 3.7: Top panel: Time evolutions of the populations of the ground (1,1), first excited (2,2), and second excited (3,3) adiabatic states for the PT-ET model, calculated via MQCL. Middle panel: The percentage of trajectories on each surface as a function of time. Bottom panel: Time evolutions of the (1,2), (2,3), and (1,3) coherences, calculated via MQCL.

of the solvent coordinate at the barrier top) in the PT-ET case, while $Q_0 = -0.5$Å (which is substantially less than the value of the solvent coordinate at the barrier top) in the ET-PT case. The percentage of trajectories on (2,2) increases to ∼15% in the first ∼1000 a.u. (c.f. ∼11% in the weakest coupling case of ET-PT), followed by a gradual decrease to ∼5% over the remaining time. A major difference between the PT-ET and set I ET-PT

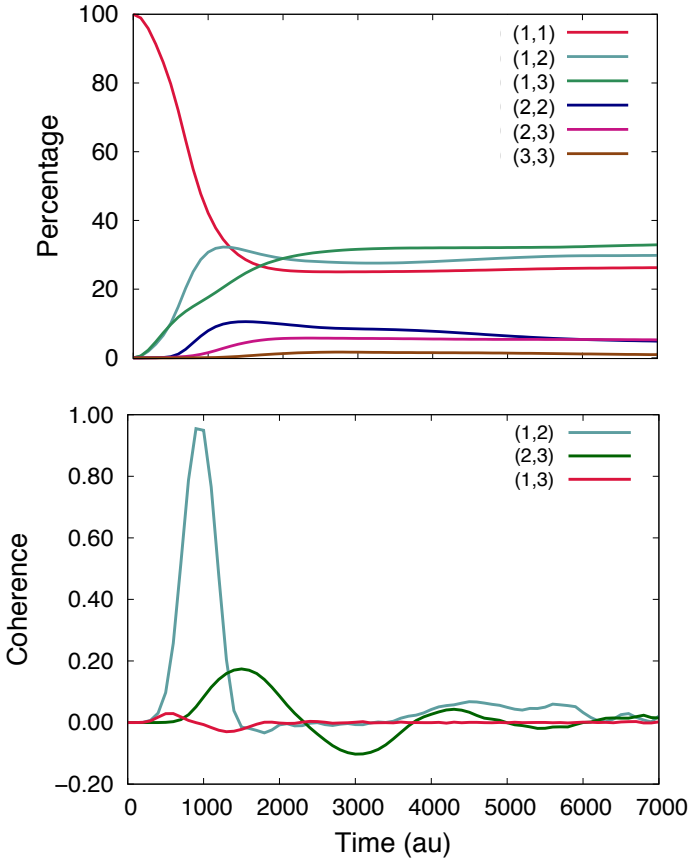

FIGURE 3.8: The percentage of trajectories on each surface as a function of time (top panel) and the time evolutions of the (1,2), (2,3), and (1,3) coherences (bottom panel) for the ET-PT model under the weakest proton/electron-solvent coupling conditions (i.e. $C_{sp} = 1.5 \times 10^{-2}/C_{se} = 2.0 \times 10^{-3}$).

results is seen in the percentage of trajectories on the (1,3) surface. In the PT-ET case, this percentage rises only to ∼11%, while in the ET-PT case it reaches ∼33%. The percentage of trajectories on the (2,3) surface is slightly higher in the ET-PT case than in the PT-ET case, i.e. 5% and 3%, respectively. These two results collectively explain the higher population of the (3,3) state in the set I ET-PT case than in the PT-ET case (i.e. 8% and 3%, respectively) and underscore the important role played by the (1,3) surface in populating the (3,3) state in the ET-PT case. There is some evidence of coherence transfer, as the (1,2) percentage decreases at the slight gain of the (1,3) percentage between $1000 - 2000$ a.u.

Examining the time-dependent coherences in the bottom panel of Fig. 3.7, we see further evidence of the important dynamical role of the (1,2) mean surface, as the (1,2) coherence rises to 1.38 (c.f. 0.95 in the weakest coupling case of ET-PT) and remains non-zero over the time period considered. This is consistent with the large percentage of trajectories on

(1,2) and its gradual increase over the time period considered (see middle panel of Fig. 3.7). Interestingly, the large rise and fall of the (1,2) coherence up to ∼1000 a.u. coincides exactly with the large rise in the (2,2) population, suggesting that this highly coherent dynamics enhances the pumping of population to the first excited state. The (1,3) coherence exhibits a very low-magnitude oscillation initially and quickly becomes zero for the remainder of the time. On the other hand, the (2,3) coherence, although very small, exhibits oscillations over the time shown. This should be contrasted with the set I ET-PT case, where we see a similar (1,3) coherence profile, but a substantially larger and longer-lived (2,3) coherence (see bottom panel of Fig. 3.8).

3.4.3 Concerted PCET mechanism

3.4.3.1 Potential energy surfaces and nonadiabatic couplings

Finally, we consider the concerted PCET mechanism with coupling constants $C_{sp} = 2 \times 10^{-3}$ and $C_{se} = 2 \times 10^{-3}$, which are the same as those used in Refs. 17 and 90 for studying concerted PCET and are similar to the set I coupling constants used herein for ET-PT and PT-ET. The corresponding PESs are shown in the top panel of Fig. 3.9. In contrast to the sequential mechanisms, the PESs are symmetric about $Q = 0.0$ Å, where both the electron and proton are at the midpoint between the donor and the acceptor (see middle panel of Fig. 3 in Ref. 90). The (1,1) surface has a double-well profile, with very shallow reactant and product wells. The minimum energy gap of 0.46 kcal/mol between the (1,1) and (2,2) surfaces occurs at the ground state barrier top. The (1,2), (2,2), and (3,3) surfaces are parabolic in shape. Over the range of solvent configurations shown, there are no small energy gaps between the (2,2) and (3,3) surfaces. The (1,3) surface is quite flat between −0.5 to 0.5 Å. Due to the large energy gaps between the (2,2) and (3,3) surfaces, the (1,3) surface is not expected to play a facilitating role in promoting population to the second excited state in the concerted PCET case.

An examination of the nonadiabatic coupling matrix elements in the bottom panel of Fig. 3.9 reveals that $|d_{12}|$ has a relatively broad peak centered at $Q = 0.0$ Å and a relatively lower maximum value of 4.3 Å^{-1} (compared to the other mechanisms at similar coupling strengths). $|d_{23}|$ remains small and constant (on average, ∼0.23 Å^{-1}) over the range of

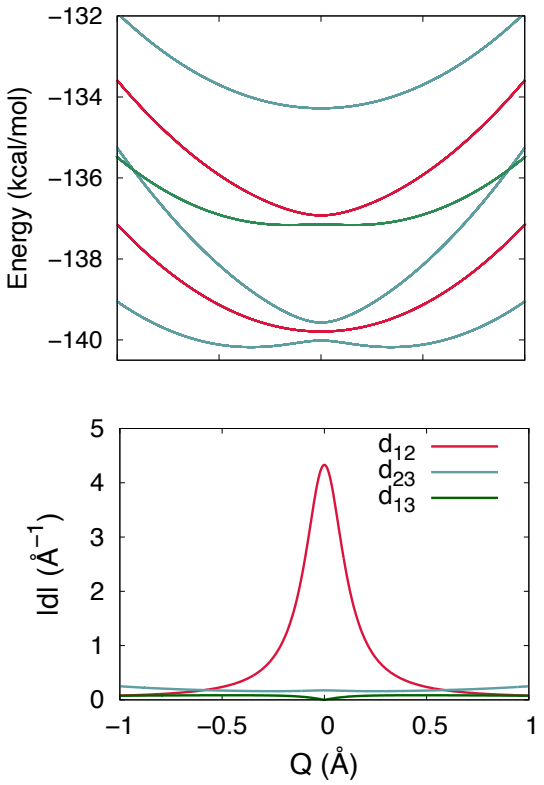

FIGURE 3.9: Top panel: Ground (1,1), first excited (2,2), and second excited (3,3) state adiabatic PESs as a function of the solvent coordinate, Q, for the concerted PCET model. The blue curves correspond to these surfaces, the red curves correspond to the mean surfaces between adjacent surfaces, and the green curve corresponds to the mean surface between the ground and second excited state surfaces. Bottom panel: Absolute values of the nonadiabatic coupling matrix elements, $|d_{12}|$, $|d_{23}|$, and $|d_{13}|$ as a function of the solvent coordinate, Q.

solvent configurations shown, while $|d_{13}|$ is ∼0.1 Å^{-1} for most of the solvent configurations shown and is exactly 0.0 Å^{-1} at $Q = 0.0$ Å.

3.4.3.2 Time-dependent state populations and coherences

The time-dependent populations of the three lowest adiabatic states are shown in the top panel of Fig. 3.10. They were calculated using an ensemble of 2×10^6 trajectories starting from initial conditions sampled from the Wigner distribution in Eq. 3.11 with $Q_o = -0.24$ Å and $P_o = 10$ a.u. As can be seen, the (1,1) population drops to ∼44% in ∼2000 a.u., while the (2,2) population rises to ∼56% in this time. This should be contrasted with the ET-PT (weakest) coupling and PT-ET cases, where we saw almost complete population inversions between the (1,1) and (2,2) states. At ∼2000 a.u., the (1,1)/(2,2) population begins to slowly increase/decrease and continues to do so till 7000 a.u., where the (1,1) and (2,2) populations

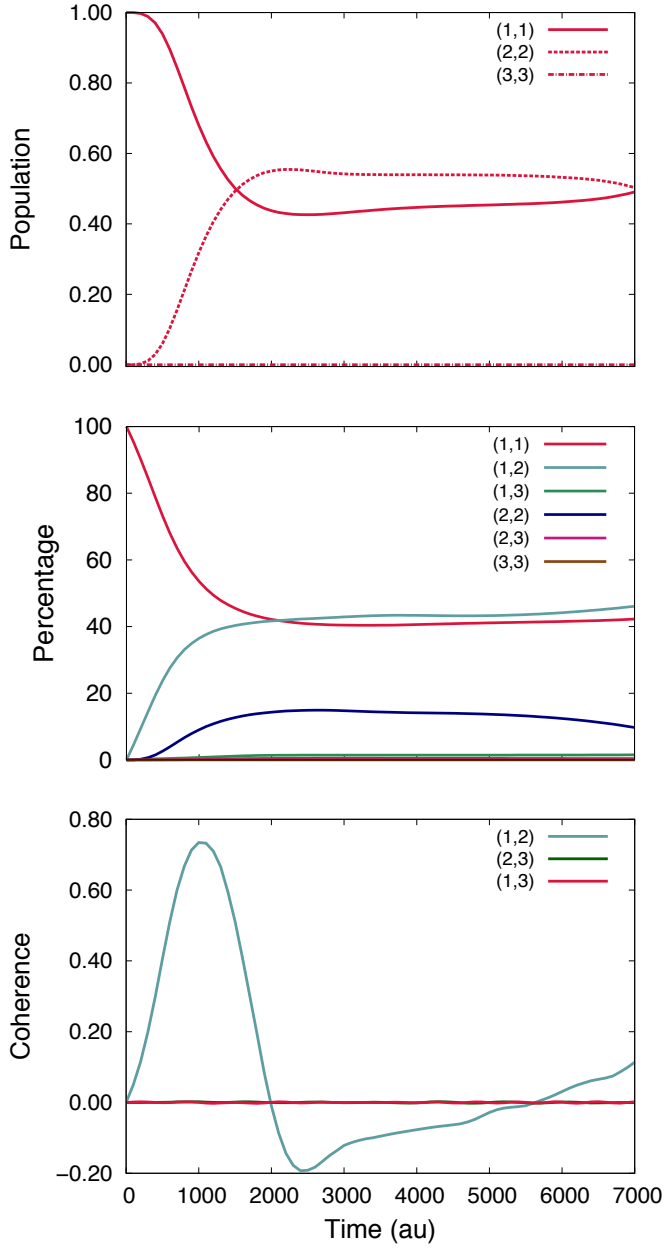

FIGURE 3.10: Top panel: Time evolutions of the populations of the ground (1,1), first excited (2,2), and second excited (3,3) adiabatic states for the concerted PCET model, calculated via MQCL. Middle panel: The percentage of trajectories on each surface as a function of time. Bottom panel: Time evolutions of the (1,2), (2,3), and (1,3) coherences, calculated via MQCL.

become equal at 50%. This should be contrasted with the ET-PT/PT-ET case, whose (1,1) population is substantially less/greater than the (2,2) populations at 7000 a.u. The (3,3) population remains zero over this time, while in the sequential cases the second excited state becomes populated for similar values of the coupling constants. This is consistent with the

fact that there are no regions of strong nonadiabatic coupling between the (2,2) and (3,3) surfaces in the concerted case.

An analysis of the percentage of trajectories in the ensemble on each surface as a function of time (see middle panel of Fig. 3.10) reveals that only the (1,1), (1,2), and (2,2) surfaces play important roles in the dynamics, which explains the fact that the second excited state never becomes populated. Ultimately, the (1,1), (1,2), and (2,2) percentages reach 42%, 45%, and 11%, respectively. The decrease in the percentage of trajectories on the (1,1) surface is almost fully compensated by the increase in the percentages of trajectories that hop to the (1,2) and (2,2) surfaces. The negligible percentage of trajectories on the (1,3) surface clearly distinguishes the nonadiabatic dynamics in the concerted case from that in the sequential cases.

Examining the time-dependent coherences in the bottom panel of Fig. 3.10, we see further evidence of the important dynamical role of the (1,2) mean surface, as the (1,2) coherence rises to 0.75 (c.f. 0.95 in the weakest coupling case of ET-PT) and remains non-zero over the time period considered. As in the PT-ET case, we see that the rise and fall of the (1,2) coherence up to ∼2000 a.u. coincides exactly with the rise in the (2,2) population. However, unlike in the sequential mechanisms, the (1,3) and (2,3) coherences are zero for all times.

3.5 Concluding remarks

In this chapter, we used the MQCL method to simulate the dynamics of the adiabatic state populations in a model PCET reaction. To illustrate the utility and accuracy of the MQCL method, we first calculated the time-dependent populations of the three lowest adiabatic states of a sequential ET-PT model for which fully quantum and FSSH results are available. The MQCL results were found to agree well with the fully quantum results and to be substantially better than the FSSH results. In light of this, we studied the effect of reducing the coupling strength between the proton-electron subsystem and the solvent environment on the population dynamics of the ET-PT model. We found that this leads to a higher population of the (2,2) state, which is due to an increased role of the (1,2) surface at early times. By varying several parameters in the Hamiltonian, we also simulated the time-dependent populations of the sequential PT-ET and concerted PCET models (for which fully quantum

and FSSH results are not available) and contrasted them with those of the weakest coupling case of the ET-PT model.

The good agreement of the MQCL results with the fully quantum ones for the ET-PT model stems from the evolution of the classical DOF not only on single adiabatic PESs, but also on their corresponding mean surfaces. For all mechanisms studied, the percentage of trajectories in the ensemble on each surface at a given time reveals that large fractions of the ensemble reside on the mean surfaces after some initial period of time. In particular, we found that the (1,2) and (1,3) surfaces are the most important mean surfaces in the nonadiabatic dynamics of the sequential mechanisms. Interestingly, our results show that the (1,3) surface can act as a bridge between the (1,2) and (2,3) surfaces (as manifested by the two small energy gaps with the (1,2) surface and one with the (2,3) surface), thereby providing another channel for population transfer to the (3,3) state. Thus, population transfer to the second excited state can occur via a *sequential* population transfer route, e.g. $(1,1) \rightarrow (1,2) \rightarrow (2,2) \rightarrow (2,3) \rightarrow (3,3)$, or can by-pass the (2,2) surface altogether via a *coherence* transfer route, e.g. $(1,1) \rightarrow (1,2) \rightarrow (1,3) \rightarrow (2,3) \rightarrow (3,3)$. Under similar coupling conditions, the percentage of trajectories that hop initially from (1,2) to (1,3) is lower in the PT-ET model than in the ET-PT one, while the percentage of trajectories that hop initially from (1,2) to (2,2) is higher in the PT-ET model than in the ET-PT one. Consequently, the sequential transfer route is likely more prevalent in the PT-ET model, while the coherence transfer route is more prevalent in the ET-PT one. These observations are consistent with the fact that the (1,3) coherence attains a slightly larger magnitude in the ET-PT model than in the PT-ET model, while the (1,2) coherence attains a larger magnitude in the PT-ET model than in the ET-PT model. In both cases, the (2,3) coherence is long-lived, but it attains a substantially larger magnitude in the ET-PT case than in the PT-ET case. In the concerted PCET model, the (3,3) surface is substantially higher in energy than the (2,2) surface and, therefore, the (3,3) state does not become populated. In this case, the (1,3) surface is not involved in the nonadiabatic dynamics, but rather the (1,2) surface facilitates the population of the first excited state via the (1,1)→(1,2)→(2,2) route. This is also reflected in the evolution of the coherences, as the (1,3) and (2,3) coherences are always zero.

Chapter 4

Calculating Proton-Coupled Electron Transfer Rate Constants via the Mixed Quantum-Classical Liouville Approach

4.1 Introduction

The rates of PCET reactions have been the subject of great attention by experimentalists [3, 12, 14, 18, 19, 105]. Electrochemistry has been one of the main tools for revealing the concerted nature of PCET reactions, which were long believed to be stepwise in nature [106, 107]. Thermal PCET reactions have been investigated by means of a combination of cyclic voltammetry and preparative-scale electrolysis [108], stopped-flow techniques [20, 95, 109, 110], and flash-quench methods [96–99]. The oxidation of phenol with a family of pendent bases, for example, has exhibited evidence of concerted PCET based on a primary isotope effect, very high rate constants, and the dependence of the rate constants on the driving force [109]. The relationship between the experimental standard free energy of such reactions and the corresponding rate constant is well captured by the Marcus-Hush-Levich model [111–117].

Theoretical investigations of PCET rates have also been carried out over the years. In the nineties, Cukier derived a PCET rate constant expression, working in a basis of localized initial and final electron/proton states [31, 118, 119]. Assuming a sufficiently small electronic coupling, the transition rate between these two states was obtained via Fermi's Golden Rule. The resulting expression is valid in the nonadiabatic regime of charge transfer, but by modifying the prefactor in this expression, one could also study cases with large electronic couplings (i.e., the adiabatic regime). Over the span of two decades, Hammes-Schiffer and coworkers have used FSSH to calculate PCET rate constants in various limits [25, 32, 120, 121]. Using Fermi's Golden Rule, they described concerted PCET in terms of nonadiabatic transitions between reactant and product electron-proton vibronic states. The total rate constant is then obtained by summing over the rate constants associated with all pairs of reactant and product vibronic states which are weighted by the reactant state Boltzmann probabilities. Over the years, there have been debates over the reliability of the results obtained from FSSH. For example, in a benchmarking study of the spin-boson model, it was shown that FSSH is unable to recover the correct scaling of Marcus' golden-rule rate with diabatic coupling [72, 73]. This was attributed to the inability of FSSH to treat decoherence. Although several schemes have been devised for incorporating decoherence into FSSH, they are ad hoc in nature [70, 71]. In another approach, Miller and co-workers extended the RPMD method to directly simulate condensed phase PCET reactions. Their method, unlike the pre-existing rate theories, does not require prior mechanistic information about a given PCET reaction and can be used in different regimes of electronic and vibrational coupling [122]. In case of

In the last chapters, we have shown the applicability of the MQCL formalism to study the nonadiabatic dynamics of PCET reactions, while accounting for decoherence effects. The objective of the present chapter is to extend this formalism for calculating PCET rate constants, starting from the time integral of the flux-flux correlation function of the reactant and product states [123]. The exact correlation function will be taken as the starting point; then, a quantum-classical approximation will be made to the dynamical part of the expression, and the calculation of the full quantum equilibrium structure is simplified greatly by making a high-temperature approximation involving the classical DOF. This is a very good approximation, since we are particularly interested in thermal PCET reactions.

4.2 PCET model

In Ref. 124, Ananth and Miller developed a way for characterizing reactive pathways in more realistic versions of the PCET models in Ref. 90, in which the solvent polarization coordinate is coupled to a bath of harmonic oscillators. Herein, we develop an MQCL-based formalism for calculating PCET rate constants for systems that can be represented by such models. These models can be described by the following Hamiltonian

$$\hat{H} = \frac{p_p^2}{2m_p} + \sum_j \frac{P_j^2}{2M_j} + \frac{p_s^2}{2m_s} + V_p(q_p) + V_e(q_p, q_s) + V_{ps}(q_p, q_s) + V_b(Q), \tag{4.1}$$

where $\{q_p, p_p, m_p\}$, $\{q_s, p_s, m_s\}$, and $\{Q_j, P_j, M_j\}$ denote the positions, momenta, and masses of the proton, solvent polarization, and bath oscillators, respectively. Within our mixed quantum-classical approach, the proton and electron are treated quantum mechanically, whereas the solvent polarization and bath modes are treated classically. The protonic potential energy, V_p, corresponding to a double well potential, is given by

$$V_p(q_p) \quad = \quad -\frac{m_p\omega_p^2}{2}q_p^2 + \frac{m_p^2\omega_p^4}{16V_0}q_p^4 - \lambda q_p^3, \tag{4.2}$$

where ω_p is the proton vibrational frequency and V_0 is the energy difference between the minimum and maximum points of the potential. The potential energy matrix corresponding to the donor and acceptor electronic states in the diabatic representation, is given by

$$V_e(q_p, q_s) = \begin{pmatrix} V_{11}(q_p) + V_{ep}(q_p) & V_{12}(q_s) \\ V_{12}(q_s) & V_{22}(q_s) - V_{ep}(q_p) \end{pmatrix} \tag{4.3}$$

where the electron–proton coupling is given by $V_{ep}(q_p) = \mu_2 \tanh(\phi q_p)$, the solvent polarization potentials in the donor and acceptor states are given by $V_{11}(q_s) = \frac{1}{2}m_s\omega_s^2(q_s - q_{s_1})^2$ and $V_{22}(q_s) = \frac{1}{2}m_s\omega_s^2(q_s - q_{s_2})^2$, respectively, and $V_{12}(q_s)$ is the diabatic coupling between the donor and acceptor states. The proton–solvent coupling is given by $V_{ps}(q_p, q_s) = -\mu_1 q_s \tanh(\phi q_p)$. The harmonic bath potential, V_b, is given by

$$V_b = \frac{1}{2}M_j\omega_j^2\left(Q_j - \frac{c_j q_s}{M_j\omega_j^2}\right), \tag{4.4}$$

where M_j and ω_j are the mass and frequency of bath oscillator j, respectively. The bath is characterized by an Ohmic spectral density

$$J(\omega) = \eta\omega \exp\left(-\omega/\omega_c\right), \tag{4.5}$$

where η denotes the strength of the coupling between the solvent polarization and bath modes and ω_c is the cut-off frequency. Discretizing this spectral density yields N harmonic oscillators with frequencies [125]

$$\omega_j = -\omega_c \ln\left(\frac{j - 0.5}{N}\right), \tag{4.6}$$

and coupling constants,

$$c_j = \omega_j \left(\frac{2\eta M_j \omega_c}{N\pi}\right)^{\frac{1}{2}}. \tag{4.7}$$

In Ref. 124, the authors used several parameter sets to mimic the different PCET mechanisms (i.e., concerted or sequential), which were based on the parameter sets in Ref. 90. In general, one may parametrize this model Hamiltonian for a system of interest by obtaining the parameters from electronic structure calculations and/or experiments. This form of the Hamiltonian provides the basis for the derivation of a quantum-classical rate coefficient in the following section.

4.3 Derivation of the time-dependent rate coefficient

4.3.1 General quantum-classical expression

The derivation of a mixed quantum-classical time-dependent rate coefficient starts from the quantum mechanical expression for the time integral of a flux-flux correlation function [123]. In this subsection, we provide a brief summary of the theory found in Refs. 126 and 127 (for the complete details of the derivation, please refer to these references). The resulting quantum-classical expression is general and will form the basis for our derivation of a practical expression for calculating rate constants of PCET reactions in the next subsection.

The rate constant for a transformation $A \rightleftharpoons B$ may be calculated from the time integral of the quantum mechanical flux-flux correlation function

$$k_{AB} = \frac{1}{n_A^{eq}} \int_0^\infty dt \langle \hat{j}_A; \hat{j}_B(t) \rangle, \tag{4.8}$$

where n_A^{eq} is the equilibrium density of the reactant species, $\hat{j}_A = \frac{i}{\hbar}[\hat{H}, \hat{A}]$ is the flux of reactant species operator $\hat{A}$, $\hat{j}_B = \frac{i}{\hbar}[\hat{H}, \hat{B}]$ is the flux of product species operator $\hat{B}$, and the flux-flux correlation function is expressed in terms of the Kubo-transformed correlation function,

$$\langle \hat{j}_A; \hat{j}_B(t) \rangle = \frac{1}{\beta} \int_0^\beta d\lambda \left\langle e^{\lambda \hat{H}} (\frac{i}{\hbar}[\hat{H}, \hat{A}]) e^{-\lambda \hat{H}} \hat{j}_B(t) \right\rangle \tag{4.9}$$

where $\beta = 1/kT$. For the purposes of a simulation, it is convenient to consider the time-dependent rate coefficient defined as the finite time integral of the flux-flux correlation function,

$$k_{AB}(t) = \frac{1}{n_A^{eq}} \int_0^t dt' \langle \hat{j}_A; \hat{j}_B(t') \rangle = \frac{1}{\beta n_A^{eq}} \langle \frac{i}{\hbar}[\hat{B}(t), \hat{A}] \rangle. \tag{4.10}$$

To arrive at a mixed quantum-classical version of the time-dependent rate coefficient, one has to first partition the total system into a subsystem of interest and a bath and then perform a partial Wigner transform over the bath variables. One can ultimately show that one form of the quantum-classical time-dependent rate is

$$k_{AB}(t) = \frac{2}{\hbar \beta n_A^{eq}} \sum_{\alpha\alpha'} \int dX \ \mathrm{Im}[B_W^{\alpha\alpha'}(X,t) W_A^{\alpha'\alpha}(X,0)] \tag{4.11}$$

where

$$W_A^{\alpha'\alpha}(X,0) = \sum_{\alpha_1\alpha_1'} \int dX' A_W^{\alpha_1\alpha_1'}(X') W^{\alpha_1'\alpha_1\alpha'\alpha}(X', X, 0). \tag{4.12}$$

In the above equations, $X \equiv (Q, P)$ and the various operators are represented in the basis of adiabatic states, defined by the eigenvalue problem $\hat{H}_W(Q)|\alpha; Q\rangle = E_\alpha(Q)|\alpha; Q\rangle$. In Eq. 4.12, the initial values of the matrix elements of the spectral density $W(X', X, 0)$ are

given by [128]

$$\begin{aligned} W^{\alpha_1'\alpha_1\alpha'\alpha}(X',X,0) &= \frac{1}{(2\pi\hbar)^{2\nu}Z_Q}\int dZdZ' e^{-\frac{i}{\hbar}(P\cdot Z+P'\cdot Z')} \\ &\times \langle\alpha';Q|\langle Q+\frac{Z}{2}|Q'-\frac{Z'}{2}\rangle|\alpha_1;Q'\rangle \\ &\times \langle\alpha_1';Q'|\langle Q'+\frac{Z'}{2}|e^{-\beta\hat{H}}|Q-\frac{Z}{2}\rangle|\alpha;Q\rangle \end{aligned} \tag{4.13}$$

where ν is the coordinate-space dimension and Z_Q is the partition function. Since $\langle Q+\frac{Z}{2}|Q'-\frac{Z'}{2}\rangle = \delta(Q+\frac{Z}{2}-(Q'-\frac{Z'}{2}))$ is a delta function, then $Q+\frac{Z}{2} = Q'-\frac{Z'}{2}$ and $Z' = 2(Q'-Q-\frac{Z}{2})$. Therefore, Eq. 4.13 may be simplified to give,

$$\begin{aligned} W^{\alpha_1'\alpha_1\alpha'\alpha}(X',X,0) &= \frac{1}{(2\pi\hbar)^{2\nu}Z_Q}\int dZ e^{-\frac{i}{\hbar}(P\cdot Z+P'\cdot(2Q'-2Q-Z))} \\ &\times \langle\alpha';Q|\alpha_1;Q'\rangle\langle\alpha_1';Q'|\langle Q'+\frac{1}{2}(2Q'-2Q-Z)|e^{-\beta\hat{H}}|Q-\frac{Z}{2}\rangle|\alpha;Q\rangle \\ &= \frac{1}{(2\pi\hbar)^{2\nu}Z_Q}e^{-\frac{2i}{\hbar}P'\cdot(Q'-Q)}\int dZ e^{-\frac{i}{\hbar}(P-P')\cdot Z} \\ &\times \langle\alpha';Q|\alpha_1;Q'\rangle\langle\alpha_1';Q'|\langle 2Q'-Q-\frac{Z}{2}|e^{-\beta\hat{H}}|Q-\frac{Z}{2}\rangle|\alpha;Q\rangle \end{aligned} \tag{4.14}$$

4.3.2 PCET rate coefficient

For the PCET model studied in this chapter, the matrix element $A_W^{\alpha_1\alpha_1'}(Q')$ is associated with the PCET reactant state and may be defined as

$$A_W^{\alpha_1\alpha_1'}(Q') = (|\phi_e^1\rangle\langle\phi_e^1|h(-q_p))^{\alpha_1\alpha_1'}, \tag{4.15}$$

where $|\phi_e^1\rangle$ is the donor electronic diabatic state and $h(-q_p)$ is the Heaviside step function that depends on the protonic coordinate, q_p. If $q_p > 0$ then $h(q_p) = 1$, whereas if $q_p < 0$ then $h(q_p) = 0$. Similarly, the matrix element associated with the PCET product state is $B_W^{\alpha\alpha'} = (|\phi_e^2\rangle\langle\phi_e^2|h(q_p))^{\alpha_1\alpha_1'}$, where $|\phi_e^2\rangle$ is the acceptor electronic diabatic state. The adiabatic wave function $|\alpha;Q\rangle$ may be expanded in an orthonormal set of two-particle basis functions as

$$|\alpha;Q'\rangle = \sum_{m,n} c_{mn}^{\alpha}(Q')|\phi_p^m\rangle|\phi_e^n\rangle, \tag{4.16}$$

where $|\phi_p^m\rangle$ is chosen to be the m^{th} eigenfunction of the quantum harmonic oscillator for a proton. The index n runs over the electronic diabatic states, i.e., it varies from 1 (donor) to 2 (acceptor). Using this expansion, we may now evaluate Eq. 4.15 to obtain

$$\begin{aligned} A_W^{\alpha_1\alpha_1'}(Q') &= \langle \alpha_1; Q' || \phi_e^1 \rangle \langle \phi_e^1 | h(-q_p) | \alpha_1'; Q' \rangle \\ &= \sum_{i,k} \sum_{j,l=1,2} c_{ij}^{\alpha_1} c_{kl}^{\alpha_1'} \langle \phi_e^j | \langle \phi_p^i || \phi_e^1 \rangle \langle \phi_e^1 | h(-q_p) | \phi_p^k \rangle | \phi_e^l \rangle \end{aligned} \tag{4.17}$$

We may then write $W_A^{\alpha'\alpha}(X,0)$ in Eq. 4.12 as

$$\begin{aligned} W_A^{\alpha'\alpha}(X,0) &= \frac{1}{(2\pi\hbar)^{2\nu} Z_Q} \sum_{\alpha_1\alpha_1'} \int dX' \sum_{i,k} \sum_{j,l=1,2} c_{ij}^{\alpha_1} c_{kl}^{\alpha_1'} \langle \phi_e^j | \langle \phi_p^i || \phi_e^1 \rangle \langle \phi_e^1 | h(-q_p) | \phi_p^k \rangle | \phi_e^l \rangle \\ &\times e^{-\frac{2i}{\hbar} P' \cdot (Q'-Q)} \int dZ e^{-\frac{i}{\hbar}(P-P')\cdot Z} \\ &\times \langle \alpha'; Q | \alpha_1; Q' \rangle \langle \alpha_1'; Q' | \langle 2Q' - Q - \frac{Z}{2} | e^{-\beta \hat{H}} | Q - \frac{Z}{2} \rangle | \alpha; Q \rangle \end{aligned} \tag{4.18}$$

To simplify Eq. 4.18, we first focus on matrix element $\langle 2Q' - Q - \frac{Z}{2} | e^{-\beta\hat{H}} | Q - \frac{Z}{2} \rangle$. The Hamiltonian of the total system, $\hat{H}$, may be partitioned into the kinetic energy of the environment and the remainder, $\hat{h}$. Considering this partitioning, one may factorize $e^{\beta\hat{H}}$ using a symmetric Trotter decomposition [129] as

$$e^{-\beta\hat{H}} = e^{-\beta\frac{\hat{h}}{2}} e^{-\beta\sum_i \frac{P_i^2}{2M_i}} e^{-\beta\frac{\hat{h}}{2}}. \tag{4.19}$$

We may insert this result into the matrix element to obtain

$$\begin{aligned} &\langle 2Q' - Q - \frac{Z}{2} | e^{-\beta\hat{H}} | Q - \frac{Z}{2} \rangle \\ &= \langle 2Q' - Q - \frac{Z}{2} | e^{-\beta\frac{\hat{h}}{2}} e^{-\beta\sum_i \frac{P_i^2}{2M_i}} e^{-\beta\frac{\hat{h}}{2}} | Q - \frac{Z}{2} \rangle \\ &= \int dQ_1 dQ_2 \langle 2Q' - Q - \frac{Z}{2} | e^{-\beta\frac{\hat{h}}{2}} | Q_1 \rangle \langle Q_1 | e^{-\beta\sum_i \frac{P_i^2}{2M_i}} | Q_2 \rangle \langle Q_2 | e^{-\beta\frac{\hat{h}}{2}} | Q - \frac{Z}{2} \rangle \\ &= \int dQ_1 dQ_2 e^{-\beta\frac{\hat{h}}{2}(2Q'-Q-\frac{Z}{2})} \langle 2Q' - Q - \frac{Z}{2} | Q_1 \rangle \langle Q_1 | e^{-\beta\sum_i \frac{P_i^2}{2M_i}} | Q_2 \rangle \langle Q_2 | Q - \frac{Z}{2} \rangle e^{-\beta\frac{\hat{h}}{2}(Q-\frac{Z}{2})} \\ &= e^{-\beta\frac{\hat{h}}{2}(2Q'-Q-\frac{Z}{2})} \langle 2Q' - Q - \frac{Z}{2} | e^{-\beta\sum_i \frac{P_i^2}{2M_i}} | Q - \frac{Z}{2} \rangle e^{-\beta\frac{\hat{h}}{2}(Q-\frac{Z}{2})}. \end{aligned} \tag{4.20}$$

Substituting this expression back into Eq. 4.18 and inserting two completeness relations involving α_2 and α_3, we obtain

$$\begin{aligned}
W_A^{\alpha'\alpha}(X,0) &= \frac{1}{(2\pi\hbar)^{2\nu}Z_Q}\sum_{\alpha_1\alpha_1'\alpha_2\alpha_3}\int dX'\sum_{i,k}\sum_{j,l=1,2}c_{ij}^{\alpha_1}c_{kl}^{\alpha_1'}\langle\phi_e^j|\langle\phi_p^i||\phi_e^1\rangle\langle\phi_e^1|h(-q_p)|\phi_p^k\rangle|\phi_e^l\rangle \\
&\times\ e^{-\frac{2i}{\hbar}P'\cdot(Q'-Q)}\int dZ e^{-\frac{i}{\hbar}(P-P')\cdot Z} \\
&\times\ \langle 2Q'-Q-\frac{Z}{2}|e^{-\beta\sum_i\frac{P_i^2}{2M_i}}|Q-\frac{Z}{2}\rangle\langle\alpha';Q|\alpha_1;Q'\rangle \\
&\times\ \langle\alpha_1';Q'|e^{-\beta\frac{\hat{h}}{2}(2Q'-Q-\frac{Z}{2})}|\alpha_2;2Q'-Q-\frac{Z}{2}\rangle \\
&\times\ \langle\alpha_2;2Q'-Q-\frac{Z}{2}|e^{-\beta\frac{\hat{h}}{2}(Q-\frac{Z}{2})}|\alpha_3;Q-\frac{Z}{2}\rangle\langle\alpha_3;Q-\frac{Z}{2}|\alpha;Q\rangle. \qquad (4.21)
\end{aligned}$$

In order to further simplify $W_A^{\alpha'\alpha}(X,0)$, it is convenient to consider the various components separately. We first consider the $\langle 2Q'-Q-\frac{Z}{2}|e^{-\beta\sum_i\frac{P_i^2}{2M_i}}|Q-\frac{Z}{2}\rangle$ term and rewrite it explicitly in terms of the product of states over all the classical DOFs,

$$\begin{aligned}
&\langle 2Q'-Q-\frac{Z}{2}|e^{-\beta\sum_i\frac{P_i^2}{2M_i}}|Q-\frac{Z}{2}\rangle \\
&= \prod_i\langle 2Q_i'-Q_i-\frac{Z_i}{2}|e^{-\beta\frac{P_i^2}{2M_i}}|Q_i-\frac{Z_i}{2}\rangle \\
&= \prod_i\int dP_i\langle 2Q_i'-Q_i-\frac{Z_i}{2}|e^{-\beta\frac{P_i^2}{2M_i}}|P_i\rangle\langle P_i|Q_i-\frac{Z_i}{2}\rangle \\
&= \prod_i\frac{1}{\sqrt{2\pi\hbar}}\int dP_i\langle 2Q_i'-Q_i-\frac{Z_i}{2}|e^{-\beta\frac{P_i^2}{2M_i}}|P_i\rangle e^{-\frac{i}{\hbar}P_i(Q_i-\frac{Z_i}{2})} \\
&= \prod_i\frac{1}{\sqrt{2\pi\hbar}}\int dP_i e^{-\beta\frac{P_i^2}{2M_i}}\langle 2Q_i'-Q_i-\frac{Z_i}{2}|P_i\rangle e^{-\frac{i}{\hbar}P_i(Q_i-\frac{Z_i}{2})} \\
&= \prod_i\frac{1}{2\pi\hbar}\int dP_i e^{-\beta\frac{P_i^2}{2M_i}}e^{\frac{i}{\hbar}P_i(2Q_i'-Q_i-\frac{Z_i}{2})}e^{-\frac{i}{\hbar}P_i(Q_i-\frac{Z_i}{2})} \\
&= \prod_i\frac{1}{2\pi\hbar}\int dP_i e^{-\beta\frac{P_i^2}{2M_i}}e^{-\frac{i}{\hbar}P_i(2Q_i-2Q_i')} \\
&= \prod_i\frac{1}{2\pi\hbar}\int dP_i e^{-\frac{\beta}{2M_i}[P_i^2+\frac{2iM_iP_i}{\beta\hbar}(2Q_i-2Q_i')]} \\
&= \prod_i\frac{1}{2\pi\hbar}\int dP_i e^{-[\frac{\beta}{2M_i}(P_i+\frac{iM_i}{\beta\hbar}(2Q_i-2Q_i'))^2+\frac{\beta}{2M_i}\frac{M_i^2}{\beta^2\hbar^2}(2Q_i-2Q_i')^2]} \\
&= \prod_i\frac{1}{2\pi\hbar}e^{-\frac{M_i}{2\beta\hbar^2}(2Q_i-2Q_i')^2}\int dP_i e^{-\frac{\beta}{2M_i}(P_i+\frac{iM_i}{\beta\hbar}(2Q_i-2Q_i'))^2}. \qquad (4.22)
\end{aligned}$$

To arrive at the final line of Eq. 4.22, we inserted a complete set of momentum states,

$\int dP_i|P_i\rangle\langle P_i|$, and then used the fact that $\langle Q|P\rangle = \frac{1}{\sqrt{2\pi\hbar}}e^{\frac{i}{\hbar}P\cdot Q}$. By letting $u_i = \sqrt{\frac{\beta}{2M_i}}[P_i + \frac{iM_i}{\beta\hbar}(2Q_i - 2Q_i')]$ and $du_i = \sqrt{\frac{\beta}{2M_i}}dP_i$, the integrals over P_i may be solved to obtain $\sqrt{\frac{2M_i\pi}{\beta}}$. Hence, the above expression simplifies to

$$\langle 2Q' - Q - \frac{Z}{2}|e^{-\beta\sum_i \frac{P_i^2}{2M_i}}|Q - \frac{Z}{2}\rangle \;=\; \prod_i \sqrt{\frac{M_i}{2\beta\pi\hbar^2}}e^{-\frac{M_i}{2\beta\hbar^2}(2Q_i - 2Q_i')^2}. \tag{4.23}$$

Inserting this expression back into Eq. 4.21 results in

$$\begin{aligned} W_A^{\alpha'\alpha}(X,0) \;=\; & \frac{1}{(2\pi\hbar)^{2\nu}Z_Q}\sum_{\alpha_1\alpha_1'\alpha_2\alpha_3}\int dQ'dP'\sum_{i,k}\sum_{j,l=1,2}c_{ij}^{\alpha_1}c_{kl}^{\alpha_1'}\langle\phi_e^j|\langle\phi_p^i||\phi_e^1\rangle\langle\phi_e^1|h(-q_p)|\phi_p^k\rangle|\phi_e^l\rangle \\ & \times\; e^{-\frac{2i}{\hbar}P'\cdot(Q'-Q)}\int dZ e^{-\frac{i}{\hbar}(P-P')\cdot Z}\prod_i\sqrt{\frac{M_i}{2\beta\pi\hbar^2}}e^{-\frac{2M_i}{\beta\hbar^2}(Q_i-Q_i')^2} \\ & \times\; e^{-\frac{\beta}{2}E_{\alpha_2}(2Q'-Q-\frac{Z}{2})}e^{-\frac{\beta}{2}E_{\alpha_3}(Q-\frac{Z}{2})}\langle\alpha';Q|\alpha_1;Q'\rangle\langle\alpha_1';Q'|\alpha_2;2Q'-Q-\frac{Z}{2}\rangle \\ & \times\; \langle\alpha_2;2Q'-Q-\frac{Z}{2}|\alpha_3;Q-\frac{Z}{2}\rangle\langle\alpha_3;Q-\frac{Z}{2}|\alpha;Q\rangle \end{aligned} \tag{4.24}$$

Next, since we are often interested in studying PCET reactions at high temperatures, we make a high temperature approximation on the environmental coordinates, i.e., we assume that $\lim_{\beta\to 0}\sqrt{\frac{M_i}{2\beta\pi\hbar^2}}e^{-\frac{2M_i}{\beta\hbar^2}(Q_i-Q_i')^2} = \delta(Q_i - Q_i')$. Evaluating these delta functions in $W_A^{\alpha'\alpha}(X,0)$ leads to

$$\begin{aligned} W_A^{\alpha'\alpha}(X,0) \;=\; & \frac{1}{(2\pi\hbar)^{2\nu}Z_Q}\sum_{\alpha_1\alpha_1'\alpha_2\alpha_3}\sum_{i,k}\sum_{j,l=1,2}c_{ij}^{\alpha_1}c_{kl}^{\alpha_1'}\langle\phi_e^j|\langle\phi_p^i||\phi_e^1\rangle\langle\phi_e^1|h(-q_p)|\phi_p^k\rangle|\phi_e^l\rangle \\ & \times\; \int dP'\int dZ e^{-\frac{i}{\hbar}(P-P')\cdot Z}e^{-\frac{\beta}{2}E_{\alpha_2}(Q-\frac{Z}{2})}e^{-\frac{\beta}{2}E_{\alpha_3}(Q-\frac{Z}{2})} \\ & \times\; \langle\alpha';Q|\alpha_1;Q\rangle\langle\alpha_1';Q|\alpha_2;Q-\frac{Z}{2}\rangle\langle\alpha_2;Q-\frac{Z}{2}|\alpha_3;Q-\frac{Z}{2}\rangle\langle\alpha_3;Q-\frac{Z}{2}|\alpha;Q\rangle. \end{aligned} \tag{4.25}$$

To carry out the integration over P', we use the definition of the Dirac delta function, $\int dP' e^{\frac{i}{\hbar}P'\cdot Z} = 2\pi\hbar\delta(Z)$. Hence,

$$\begin{aligned} W_A^{\alpha'\alpha}(X,0) &= \frac{1}{(2\pi\hbar)^\nu Z_Q} \sum_{\alpha_1\alpha_1'\alpha_2\alpha_3} \sum_{i,k} \sum_{j,l=1,2} c_{ij}^{\alpha_1} c_{kl}^{\alpha_1'} \langle\phi_e^j|\langle\phi_p^i||\phi_e^1\rangle\langle\phi_e^1|h(-q_p)|\phi_p^k\rangle|\phi_e^l\rangle \\ &\times \int dZ\delta(Z) e^{-\frac{i}{\hbar}P\cdot Z} e^{-\frac{\beta}{2}E_{\alpha_2}(Q-\frac{Z}{2})} e^{-\frac{\beta}{2}E_{\alpha_3}(Q-\frac{Z}{2})} \\ &\times \langle\alpha';Q|\alpha_1;Q\rangle\langle\alpha_1';Q|\alpha_2;Q-\frac{Z}{2}\rangle\langle\alpha_2;Q-\frac{Z}{2}|\alpha_3;Q-\frac{Z}{2}\rangle\langle\alpha_3;Q-\frac{Z}{2}|\alpha;Q\rangle \end{aligned} \tag{4.26}$$

Now, we can carry out the integration over Z using the fact that $\int dZ\delta(Z)f(Z) = f(0)$:

$$\begin{aligned} W_A^{\alpha'\alpha}(X,0) &= \frac{1}{(2\pi\hbar)^\nu Z_Q} \sum_{\alpha_1\alpha_1'\alpha_2\alpha_3} \sum_{i,k} \sum_{j,l=1,2} c_{ij}^{\alpha_1} c_{kl}^{\alpha_1'} \langle\phi_e^j|\langle\phi_p^i||\phi_e^1\rangle\langle\phi_e^1|h(-q_p)|\phi_p^k\rangle|\phi_e^l\rangle \\ &\times e^{-\frac{\beta}{2}E_{\alpha_2}(Q)} e^{-\frac{\beta}{2}E_{\alpha_3}(Q)} \\ &\times \langle\alpha';Q|\alpha_1;Q\rangle\langle\alpha_1';Q|\alpha_2;Q\rangle\langle\alpha_2;Q|\alpha_3;Q\rangle\langle\alpha_3;Q|\alpha;Q\rangle \end{aligned} \tag{4.27}$$

The four Dirac delta functions in this equation tell us that non-zero contributions arise when $\alpha = \alpha_3 = \alpha_2 = \alpha_1'$ and $\alpha_1 = \alpha'$. Finally, $W_A^{\alpha'\alpha}(X,0)$ simplifies to

$$W_A^{\alpha'\alpha}(X,0) = \frac{e^{-\beta E_\alpha(Q)}}{(2\pi\hbar)^\nu Z_Q} \sum_{i,k} \sum_{j,l=1,2} c_{ij}^{\alpha'} c_{kl}^{\alpha} \langle\phi_e^j|\langle\phi_p^i||\phi_e^1\rangle\langle\phi_e^1|h(-q_p)|\phi_p^k\rangle|\phi_e^l\rangle. \tag{4.28}$$

We may now simplify the sums in Eq. 4.28. First, we rewrite the sums as

$$\sum_{i,k} \sum_{j,l=1,2} c_{ij}^{\alpha'} c_{kl}^{\alpha} \langle\phi_e^j|\langle\phi_p^i||\phi_e^1\rangle\langle\phi_e^1|h(-q_p)|\phi_p^k\rangle|\phi_e^l\rangle = \sum_{i,k} \sum_{j,l=1,2} c_{ij}^{\alpha'} c_{kl}^{\alpha} \langle\phi_e^j|\phi_e^1\rangle\langle\phi_p^i|h(-q_p)|\phi_p^k\rangle\langle\phi_e^1|\phi_e^l\rangle. \tag{4.29}$$

Due to the two Dirac delta functions, this expression has a nonzero value if and only if $j = l = 1$. Therefore, we obtain

$$\begin{aligned} \sum_{i,k} c_{i1}^{\alpha'} c_{k1}^{\alpha} \langle\phi_p^i|h(-q_p)|\phi_p^k\rangle &= \sum_{i,k} c_{i1}^{\alpha'} c_{k1}^{\alpha} \int_{-\infty}^{+\infty} dq_p \phi_p^i(q_p) h(-q_p) \phi_p^k(q_p) \\ &= \sum_{i,k} c_{i1}^{\alpha'} c_{k1}^{\alpha} \int_{-\infty}^{0} dq_p \phi_p^i(q_p) \phi_p^k(q_p) \end{aligned} \tag{4.30}$$

Finally, $B_W^{\alpha\alpha'}(X,t)$ in Eq. 4.11 may be evaluated in a similar fashion to $A_W^{\alpha_1\alpha_1'}(X')$, yielding the final expression for the time-dependent rate coefficient

$$\begin{aligned} k_{AB}(t) &= \frac{2}{\hbar\beta n_A^{eq}} \sum_{\alpha\alpha'} \int dX \ \mathrm{Im} \left[\sum_{ik} c_{i2}^{\alpha}(t) c_{k2}^{\alpha'}(t) \int_0^{\infty} dq_p \phi_p^i(q_p) \phi_p^k(q_p) \right. \\ &\times \left. \sum_{lm} c_{l1}^{\alpha'}(0) c_{m1}^{\alpha}(0) \int_{-\infty}^{0} dq_p \phi_p^l(q_p) \phi_p^m(q_p) \right] \frac{e^{-\beta E_\alpha(Q)}}{(2\pi\hbar)^\nu Z_Q}. \end{aligned} \tag{4.31}$$

In the long time limit, the time-dependent rate coefficient, $k_{AB}(t)$, decays to zero. However, if there is a sufficiently large separation between the timescales of the chemical reaction and the transient microscopic dynamics, the rate coefficient first decays to a plateau from which the rate constant, k_{AB}, can be extracted (see Fig. 4.1).

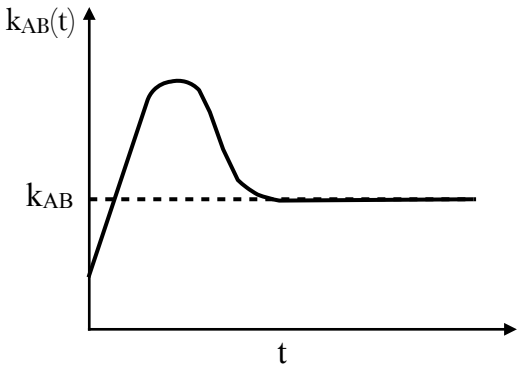

FIGURE 4.1: The rate coefficient, $k_{AB}(t)$, as a function of time. The dotted line indicates the value of the rate constant, k_{AB}.

In summary, the mixed quantum-classical expression for the PCET rate coefficient in Eq. 4.31 was rigorously derived from the quantum mechanical expression for the flux-flux correlation function. Apart from the high temperature approximation made on the classical DOF, it constitutes a general formula for calculating PCET rate constants in systems where the environment of the transferring proton and electron can be treated classically to a good approximation. In contrast to Cukier's expressions, our expression can simultaneously handle adiabatic and nonadiabatic charge transfer. It also improves upon FSSH-based methods, which are ad hoc and do not properly account for decoherence.

4.4 Simulating the time-dependent rate coefficient

In this section, we explain how each component of the time-dependent coefficient in Eq. 4.31 is simulated in practice.

4.4.1 Sampling the thermal equilibrium distributions

In order to generate properly distributed initial conditions for calculating the time-dependent rate coefficient, one must sample the thermal equilibrium distributions $e^{-\beta E_\alpha(Q)}/Z_Q$ for each value of α. We obtain initial values of the classical positions and velocities of the solvent polarization and bath oscillators from Gaussian distributions with standard deviations $\sigma_{v_s} = (\beta m_s)^{-\frac{1}{2}}$ and $\sigma_{q_s} = \omega_s^{-1}(\beta m_s)^{-\frac{1}{2}}$ for the solvent polarization and $\sigma_{V_j} = (\beta M_j)^{-\frac{1}{2}}$ and $\sigma_{Q_j} = \omega_j^{-1}(\beta M_j)^{-\frac{1}{2}}$ for the bath coordinates. For the purposes of the calculation, the mean of q_s is chosen such that the initial values of q_s correspond to reactant configurations.

Now that initial values of the positions and velocities have been selected, one needs to then sample from $e^{-\beta E_\alpha(Q)}/Z_Q$ for each value of α. This can be done by first considering that we are interested in averages of the form

$$\sum_{\alpha\alpha'} \int dX \cdots \frac{e^{-\beta E_\alpha(Q)}}{Z_Q}, \tag{4.32}$$

where $Z_Q = \sum_\alpha \int dX e^{-\beta E_\alpha(Q)}$. For convenience, we illustrate the sampling procedure for the case of a two-state system, although this can be generalized for any number of states. In this case, we may write the average explicitly as

$$\int dX \cdots \frac{e^{-\beta E_1(Q)}}{Z_Q} + \int dX \cdots \frac{e^{-\beta E_1(Q)}}{Z_Q} + \int dX \cdots \frac{e^{-\beta E_2(Q)}}{Z_Q} + \int dX \cdots \frac{e^{-\beta E_2(Q)}}{Z_Q} \tag{4.33}$$

where the first two terms correspond to $\alpha\alpha' = 11$ and $\alpha\alpha' = 12$ and the latter two correspond to $\alpha\alpha' = 21$ and $\alpha\alpha' = 22$. Let us first consider the 11 term. It may be rewritten as follows,

$$\begin{aligned} & \int dX \cdots \frac{e^{-\beta E_1(Q)}}{\int dX (e^{-\beta E_1(Q)} + e^{-\beta E_2(Q)})} \\ = & \int dX \cdots \frac{e^{-\beta E_1(Q)}}{\int dX e^{-\beta E_1(Q)} (1 + e^{-\beta(E_2 - E_1)})} \times \frac{\int dX e^{-\beta E_1(Q)}}{\int dX e^{-\beta E_1(Q)}} \\ = & \left(\frac{\int dX \cdots e^{-\beta E_1(Q)}}{\int dX e^{-\beta E_1(Q)}} \right) \left(\frac{\int dX (1 + e^{-\beta(E_2 - E_1)}) e^{-\beta E_1(Q)}}{\int dX e^{-\beta E_1(Q)}} \right)^{-1} \end{aligned} \tag{4.34}$$

Thus, the 11/12 term may be calculated as follows. One generates an ensemble of initial values of the positions and velocities. For each set of initial positions and velocities, one equilibrates the system on the ground-state surface, $E_1(Q)$, at the desired temperature using a Nosé-Hoover chain thermostat. [130] A Nosé-Hoover chain thermostat is needed, since the dynamics of the classical harmonic oscillators is non-ergodic when a Nosé-Hoover thermostat is used. This generates an ensemble of initial conditions with the proper canonical distribution, from which microcanonical trajectories are run to propagate the time-dependent product species operator. The 11/12 term may be assembled by calculating the ground state average within the first set of brackets in Eq. 4.34 and then reweighting it by the inverse of the ground state average of $(1 + e^{-\beta(E_2 - E_1)})$ within the second set of brackets. One can follow a similar procedure for calculating the 21/22 term, where now the equilibration is performed on the $E_2(Q)$ surface and the first-excited state average is reweighted by the inverse of the first-excited state average of $(1 + e^{-\beta(E_1 - E_2)})$. It should be noted that, as per Eq. 4.31, one must also calculate $\sum_{lm} c_{l1}^{\alpha'}(0) c_{m1}^{\alpha}(0) \int_{-\infty}^{0} dq_p \phi_p^l(q_p) \phi_p^m(q_p)$ at the beginning of each microcanonical trajectory.

4.4.2 Simulating the time evolution of the product species operator

After sampling the initial conditions, one must simulate the time evolution of the product species operator by evaluating $\sum_{ik} c_{i2}^{\alpha'}(t) c_{k2}^{\alpha}(t) \int_{0}^{\infty} dq_p \phi_p^i(q_p) \phi_p^k(q_p)$ in Eq. 4.31. In particular, the time evolutions of $c_{i2}^{\alpha'}(t)$ and $c_{k2}^{\alpha}(t)$ may be simulated using the SSTP algorithm described in Chapter 1.

4.4.3 Calculating the equilibrium density of the reactant species

The equilibrium density of the reactant species is given by

$$n_A^{eq} = \frac{1}{(2\pi\hbar)^\nu Z_Q} \sum_{\alpha\alpha'} \int dX \Theta_A^{\alpha\alpha'} e^{-\beta H_\alpha}, \tag{4.35}$$

where Θ_A is the reactant Heaviside step function. For the PCET reaction, n_A^{eq} may be written explicitly as

$$n_A^{eq} = \frac{1}{(2\pi\hbar)^\nu Z_Q} \sum_{\alpha\alpha'} \int dX (|\phi_e^1\rangle\langle\phi_e^1| h(-q_p))^{\alpha\alpha'} e^{-\beta H_\alpha}, \tag{4.36}$$

where the matrix elements of the reactant Heaviside function are given by Eq. 4.30. Evaluating this expression involves the same considerations as in the first subsection of this section.

4.5 Results for PCET model

In this section, we present results for Model I in Ref. 124. The parameters for this model are included in Table 4.1.

TABLE 4.1: Parameters for the model Hamiltonian in Eq. 4.1. All values are in atomic units except the temperature, T, which is in Kelvin.

$m_s = 22000$	$\omega_s = 3.72 \times 10^{-4}$	$q_s^1 = -2.13$	$q_s^2 = 2.13$
$m_p = 1836.1$	$\omega_p = 1.04 \times 10^{-2}$	$V_0 = 1.2 \times 10^{-2}$	$\mu_2 = 5.84 \times 10^{-3}$
$\mu_1 = 1.1 \times 10^{-3}$	$V_{12} = 2.45 \times 10^{-2}$	$\phi = 8.0$	$\lambda = 0.0$
$N = 12$	$M_j = m_s$	$\eta = m_s\omega_s$	$T = 300$

4.5.1 Solving the time-independent Schrödinger equation

Before presenting the results, we explain how we solved the time-independent Schrödinger equation, $\hat{h}|\alpha;Q\rangle = E_\alpha(Q)|\alpha;Q\rangle$, at each time step of the simulation where $\hat{h}$ is the Hamiltonian in Eq. 4.1 without the purely classical terms. As mentioned earlier, this first involves

expanding the adiabatic wave function $|\alpha; Q\rangle$ in an orthonormal set of two-particle basis functions:

$$|\alpha; Q\rangle = \sum_{m,n} c_{mn}^{\alpha} |\phi_p^m\rangle |\phi_e^n\rangle, \tag{4.37}$$

where $|\phi_p^m\rangle$ is chosen to be the m^{th} eigenfunction of the quantum harmonic oscillator for a proton and $|\phi_e^n\rangle$ is the n^{th} electronic diabatic state, where n varies from 1 (donor) to 2 (acceptor). Thus, for M protonic basis functions, the $2M \times 2M$ Hamiltonian matrix is composed of matrix elements given by $h_{\{ij\}\{kl\}} = \langle \phi_p^i \phi_e^j | \hat{h} | \phi_p^k \phi_e^l \rangle$, where the protonic integrals may be computed numerically using

$$\phi_p^i(q_p) = \langle q_p | \phi_p^i \rangle = (2^i i! \sqrt{\pi})^{-1/2} \alpha_p^{1/2} e^{-\alpha_p^2 (q_p - q_p^o)/2} H_i(\alpha_p (q_p - q_p^o)). \tag{4.38}$$

Here, $H_i(q)$ is the i^{th} Hermite polynomial, $\alpha_p = 3.97$ Å^{-1}, and $q_p^o = 0$ Å. The integrals are calculated using the trapezoid rule with 300 points evenly spaced over the range $-0.79 < q_p < 0.79$ Å. It was determined that $M = 20$ protonic states was sufficient for converging the eigenvalues. After constructing the Hamiltonian matrix, the eigenvalue problem, $hc = Ec$, is solved at each step of the simulation to obtain $\{c_{mn}^{\alpha}\}$ and $\{E_{\alpha}\}$.

4.5.2 Results

In our calculations of $k_{AB}(t)$, we considered the participation of the two lowest adiabatic potential energy surfaces (PESs). In the upper panel of Fig. 4.2, we show the ground and first-excited state PESs as a function of the solvent polarization coordinate, q_s, for this model. We see that the reactant/product energy barrier on the ground PES is 1.0 kcal/mol=1.68 kT. A minimum energy gap of 0.5 kcal/mol at $q_s = 0$ Å separates the ground and first excited state PESs. The absolute value of the nonadiabatic coupling between these two surfaces, $|d_{12}|$, as a function of q_s is depicted in the lower panel of the Fig. 4.2. As expected, it is peaked at $q_s = 0$ Å, indicating that nonadiabatic transitions are most probable in the barrier-top region.

Next, we present the results of the time-dependent rate coefficient, $k_{AB}(t)$ in Eq. 4.31 for Model 1, calculated using the SSTP algorithm. We first calculated the adiabatic rate coefficient, which involves propagating the product species operator using adiabatic dynamics.

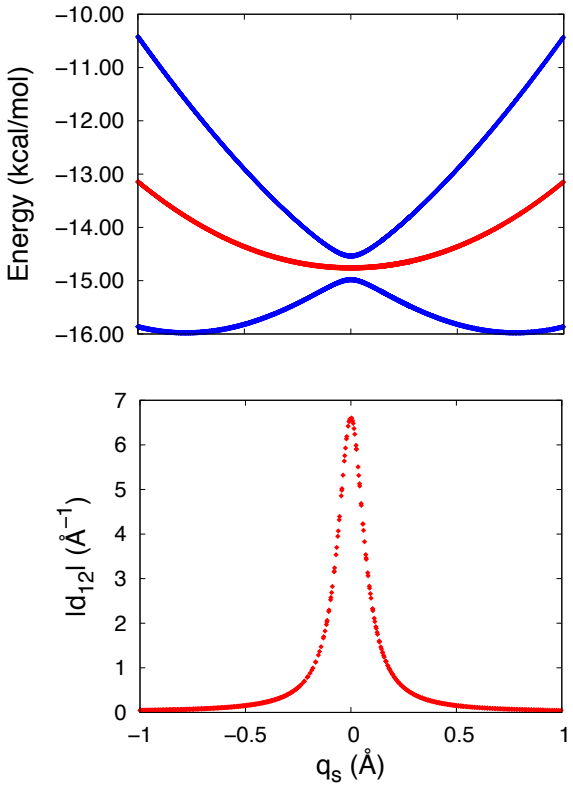

FIGURE 4.2: Upper panel: The ground and first-excited state PESs as a function of q_s for Model 1. Lower panel: The absolute value of the nonadiabatic coupling between these two surfaces, $|d_{12}|$, as a function of q_s.

This calculation involved 5×10^5 trajectories with a time step of 20 a.u. As can be seen in the left panel of Fig. 4.3, the rate coefficient first increases to its transition state theory value, followed by a decrease to a plateau of $k_{AB}(t \sim 9000 \text{ a.u.}) = 0$ a.u. (depicted by the red line). Thus, our adiabatic calculation yields a rate constant of 0 a.u., indicating that our form of the rate coefficient is not suitable for calculating the adiabatic contribution to the rate constant. (N.B.: This occurs due to the form of the rate coefficient.) For the calculation of the nonadiabatic rate coefficient, we used 50×10^6 trajectories with a time step of 100 a.u. We also applied an observable-cutting filter [84] to reduce the statistical fluctuations. As can be seen, the nonadiabatic rate coefficient exhibits a similar behaviour to the adiabatic one, but plateaus to a non-zero value of 1.47×10^{-6} a.u., yielding a rate constant of $k_{AB} = 1.47 \times 10^{-6}$ a.u. (see right panel of Fig. 4.3). Comparing the value of our rate constant to the exact value of 1.71×10^{-6} a.u. reported in Ref. 124, we see that our mixed quantum-classical approach performs well, attesting to the reliability and applicability of our approach for calculating PCET rate constants. There are several possible reasons for

the discrepancy between our average and the exact result, including the approximations that are inherent to the MQCL approach and SSTP algorithm, the use of only two states in the calculation, and an insufficient number of trajectories.

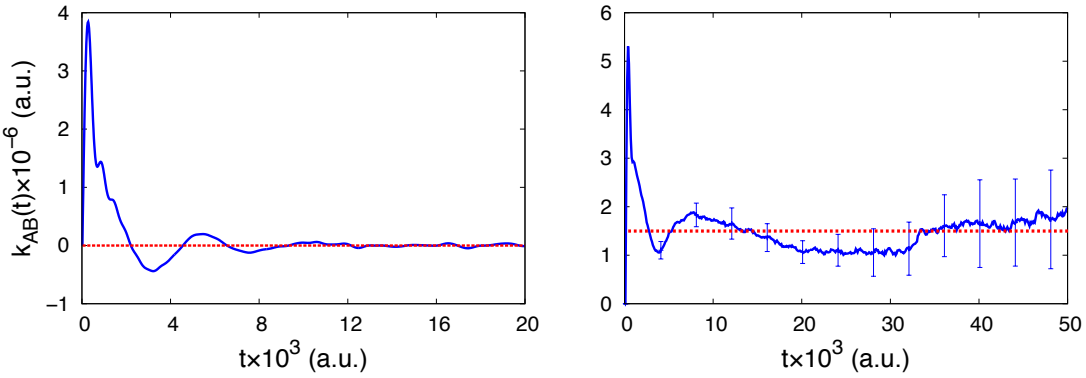

FIGURE 4.3: The adiabatic (left) and nonadiabatic (right) rate coefficients as a function of time, $k_{AB}(t)$. The dotted red lines indicate the plateau values.

4.6 Conclusion

We derived a novel formula for computing the rate constant of a PCET reaction. The derivation of the time-dependent rate coefficient starts from a general mixed quantum-classical expression for a reaction $A \rightleftharpoons B$ [126–128], which originates from the time integral of the quantum mechanical flux-flux correlation function. By introducing species operators that are suitable for monitoring a PCET reaction, we carry out a derivation of the time-dependent rate coefficient for a PCET reaction. The resulting rate coefficient has a dynamical part involving the time evolution of the product species operator and an equilibrium part. This formula is general, not requiring any prior assumptions about the parameters of the system. Furthermore, since MQCL dynamics is used to evolve the product species operator, this approach treats decoherence on a more solid footing than the FSSH-based methods. We then show how to simulate this rate coefficient in practice, paying special attention to the equilibrium sampling part due to its non-trivial nature. This approach was then applied to a more realistic version of the PCET model studied in the last two chapters, where now the solvent polarization coordinate, q_s, is coupled to a dissipative bath of harmonic oscillators. Our result for the rate constant for this model was in good agreement with the exact result.

Chapter 5

Conclusion

5.1 Concluding remarks

This thesis presents the first-ever application of MQCL dynamics to the study of PCET reactions. As it is the first study of its kind, it has been first conducted on a reduced model of a condensed phase PCET reaction consisting of a proton, an electron, and a solvent polarization coordinate and then on an extended version of the model in which a dissipative bath is also coupled to the solvent coordinate. The results in this thesis are compared and contrasted with available FSSH and exact quantum results whenever possible [90, 92, 124]. By varying the parameters in the model Hamiltonians, we were able to study both concerted and sequential PCET reactions.

The nonadiabatic dynamics of the various mechanisms in a two-level version of the model PCET reaction was first probed via a trajectory analysis, whereby ensembles of 1000 trajectories were generated using the same initial configuration but different momenta in each case. The percentages of successful PCET reactions were calculated, where a successful reaction was defined as one that started on the ground state reactant site and ended up on either the ground or the first excited state product site. To gain a better idea of the nonadiabatic transitions between the adiabatic states, the corresponding nonadiabatic coupling vectors were also calculated for each mechanism, all of which were peaked at the solvent configurations corresponding to the minimum energy gaps between the (1,1) and (2,2) states. One of the main features differentiating MQCL from FSSH is the presence of the mean surfaces between

adiabatic states that can facilitate nonadiabatic transitions. In this case, for example, the transitions between (1,1) and (2,2) occurs via $(1,1) \rightarrow (1,2)/(2,1) \rightarrow (2,2)$ (since in any transition only one of the indices is allowed to change). Thus, in contrast to the adiabatic dynamics results, the nonadiabatic results are expected to be different than the FSSH ones. Indeed, the percentages of successful PCET reactions for all three mechanisms were drastically different from FSSH. Further examination revealed that the majority of the time spent by trajectories in the ensembles was on the mean surfaces (1,2) or (2,1) and not on the (1,1) and (2,2) surfaces. These results underscore the importance of taking into account the mean surfaces in the calculations of observables.

This trajectory analysis demonstrated the differences between MQCL and FSSH trajectories, but there was still the question of how different would the expectation values of observables be and how closely would the MQCL results agree with exact quantum ones. Hence, we next calculated the time-dependent adiabatic state populations for the ET-PT mechanism in a three-level version of the same model, since both FSSH and exact quantum results were available to compare with. To accomplish this, our MQCL code had to be generalized for the treatment of an n-level system and modified to calculate an observable, viz., state populations in this case. The agreement between the MQCL and fully quantum populations is very good for the most part, while the FSSH populations show deviations from the fully quantum results starting at early times. In light of this good agreement, we also calculated the populations for the PT-ET and concerted PCET mechanisms. To gain insight into the role of the various surfaces in populating the adiabatic states, the percentages of trajectories in the ensembles on each surface at a given time were also calculated. For all mechanisms studied, we found that large fractions of the ensemble reside on the mean surfaces after some initial period of time. In particular, it was found that the (1,2) and (1,3) surfaces were the most important mean surfaces in the nonadiabatic dynamics of the sequential mechanisms for this model. In fact, the (1,3) surface acts as a bridge between the (1,2) and (2,3) surfaces, thereby providing another channel for population transfer to the (3,3) state. Overall, we found that population transfer to the second-excited state can occur via a *sequential* population transfer route, e.g. $(1,1) \rightarrow (1,2) \rightarrow (2,2) \rightarrow (2,3) \rightarrow (3,3)$, or can by-pass the (2,2) surface altogether via a *coherence* transfer route, e.g. $(1,1) \rightarrow (1,2) \rightarrow (1,3) \rightarrow (2,3) \rightarrow (3,3)$.

The role of decoherence in the nonadiabatic dynamics of these model PCET reactions was

explored by calculating the phase factor and time-dependent coherences between adiabatic states. When the classical DOF are on the mean surface, the observable in question gains a phase, $\mathcal{W}_{\alpha_{j-1}\alpha'_{j-1}}(t_{j-1}, t_j) = e^{-i\omega_{\alpha_{j-1}\alpha'_{j-1}}\Delta t_j}$. Fluctuations of the classical coordinates can cause this phase factor to oscillate in time differently for each trajectory and, therefore, averaging over an ensemble of trajectories can lead to destructive interference in the expectation value of an observable. In Chapter 2, we calculated the real part of phase factor, $\langle \mathrm{Re}[\mathcal{W}(t)] \rangle$, averaged over 1000 trajectories for the various mechanisms. Interestingly, they exhibited a decay profile which was different for each PCET mechanism. These results allowed us to gauge the importance of quantum decoherence in PCET reactions. In Chapter 3, we directly calculated the time-dependent (1,2), (1,3), and (2,3) coherences between the corresponding adiabatic states. In the case of the ET-PT mechanism, the (1,2) coherence exhibited the largest magnitude and was the most long-lived, while the smaller (1,3) and (2,3) coherences decay to zero much earlier. The most interesting result was the non-zero (1,3) coherence, which confirmed the importance of the (1,3) mean surface in nonradiatively populating the excited states. In the case of the PT-ET mechanism, the (1,2) coherence becomes more important, which is consistent with the large percentage of trajectories on (1,2) in this case. The (1,3) coherence exhibits a very low-magnitude oscillation initially and quickly becomes zero for the remainder of the time, which is consistent with the lower (3,3) population in PT-ET than ET-PT. In the concerted PCET case, the only important coherence is the (1,2) coherence and along with the zero (1,3) and (2,3) coherences, we also see that the (3,3) state never gets populated. These results underscore the importance of coherent dynamics in the calculations of observables on sub-picosecond timescales.

In Chapters 2 and 3, we also investigated the effects of varying the coupling strengths between the proton/electron and the solvent on the nonadiabatic PCET dynamics. Increasing the coupling strength stabilizes the minima on the ground and excited adiabatic surfaces, which leads to a higher ground state energy barrier and thereby lower percentage of successful PCET reactions. On the other hand, it decreases the minimum energy gap between the ground and first excited state surfaces and, as a result, $|d_{12}|$ values becomes narrower and grows in height. This leads to a higher probability of nonadiabatic transitions at the barrier top which can help trajectories to overcome the energy barrier. These phenomena significantly affect the nonadiabatic dynamics in all three mechanisms but not necessarily in the same way, which is apparent in the percentages of successful PCET trajectories. The

behaviour of these percentages is case-specific, however, in all cases, this percentage suddenly drops to zero at high coupling strengths due to the emergence of very high reaction barriers. An increase in the coupling strength also affects the phase factor, as it leads to a faster decay of $\langle \mathrm{Re}[\mathcal{W}(t)] \rangle$. Furthermore, given the drastic changes in the shapes of the surfaces at different coupling strengths, a drastic change in the time-dependent state population dynamics was expected. The results of this study for the ET-PT mechanism were presented in Chapter 3. It was found that, in going from the strongest to the intermediate coupling, there is a drastic increase in the (2,2) population at the expense of the (1,1) population. However, after some time, the (2,2) population begins to decrease at the expense of an increasing (1,1) population, decreasing more than in the strongest coupling case due to the wider $|d_{12}|$ profile. In the lowest coupling case, there is an almost complete population reversal between the ground and first-excited state populations at early times. Despite the major differences in the (1,1) and (2,2) populations, the differences between the (3,3) populations in the three cases are quite minor.

Since the MQCL formalism was found to be capable of successfully calculating an observable such as a state population, we then proceeded to derive a novel formula for calculating the time-dependent rate coefficient for a PCET reaction, from which one can extract the PCET rate constant. This derivation started from the fully quantum expression for the time integral of the flux-flux correlation function, followed by various mixed quantum-classical approximations. The resulting rate coefficient has a dynamical part involving MQCL time evolution of the product species operator and a tractable equilibrium sampling part, which was obtained by invoking a high-temperature approximation on the environmental DOF. This formula is general, not requiring any prior assumptions about the parameters of the system. Furthermore, since MQCL dynamics is used to evolve the product species operator, this approach treats decoherence on a more solid footing than FSSH. The resulting algorithm was implemented into a code and, to confirm its reliability, we applied it to a PCET model for which an exact rate constant is available. This model is based on the model studied in Chapters 2 and 3, but now a harmonic bath is also coupled to the solvent coordinate. We extracted the rate constant for the concerted PCET mechanism studied from the plateau value of the time-dependent rate coefficient. The calculated rate constant was in good agreement with the exact result, thereby confirming the reliability of our MQCL-based rate coefficient formula.

Given the (i) more rigorous basis of the MQCL surface-hopping approach, (ii) the fact that it yielded significantly different results than the FSSH approach for the reduced model considered in this study, and (iii) the good agreement between the MQCL results and exact quantum ones, we believe that the MQCL method could provide new insight into the nonadiabatic dynamics of a wide range of PCET reactions. Insights gained by studying reduced models can also facilitate the understanding of factors which control PCET rates in more complex systems. MQCL will be especially useful for treating cases in which FSSH struggles, i.e., cases that exhibit complex coherence dynamics.

5.2 Future plans

A great deal of research has focused on thermal PCET reactions due to their critical role in biological systems. However, the fact that PCET reactions occur at the heart of solar-energy-harvesting systems underscores the importance of photo-induced PCET as well. Compared to thermal PCET reactions, little is known about PCET reactions of electronically excited molecules. The results of our studies over the past few years revealed new aspects of the nonadiabatic dynamics of PCET reactions. More specifically, the MQCL method has proven to be appropriate for calculating population of adiabatic states, which would be an observable of interest in studies of photo-induced PCET. In such cases, the classical DOF in the system would need to be initialized on excited electronic states and not on the ground state. Carrying out the dynamics on excited-state potentials may require including more states in our calculations than what we have considered till now. The presence of mean surfaces in the MQCL method generates an enormous number of possibilities for nonadiabatic pathways between the states and hence may provide a more accurate picture of the photo-induced PCET dynamics.

Moreover, studying PCET in real, complex systems will bring us closer to designing more efficient energy conversion systems. Studying PCET reactions in such systems may be made more feasible with the aid of quantum mechanics/molecular mechanics (QM/MM), so I would like to expand the territory of my MQCL studies to incorporate QM/MM methods as well. In this case, the choice of QM method is crucial, namely, the electronic structure method should be sufficiently accurate for the system of interest as well as computationally efficient.

The MM force field also should be chosen such that it accurately describes the part of the system outside the QM subsystem and its interactions with the QM region. For example, in the case of photosynthetic systems, the "right" QM/MM approach could provide an efficient yet accurate way to study the mechanisms and rates of each oxidation step of the Kok cycle and the roles of the nearby tyrosine and water molecules.

Bibliography

[1] Galstyan, A.; Robertazzi, A.; Knapp, E. W. *J. Am. Chem. Soc.* **2012**, *134*, 7442.

[2] Ames, W.; Pantazis, D. A.; Krewald, V.; Cox, N.; Messinger, J.; Lubitz, W.; Neese, F. *J. Am. Chem. Soc.* **2011**, *133*, 19743.

[3] Weinberg, D.; Gagliardi, C.; Hull, J.; Fecenko Murphy, C.; Kent, C.; Westlake, B.; Paul, A.; Ess, D.; Granville McCafferty, D.; Meyer, T. *Chem. Rev.* **2012**, *112*, 4016.

[4] Guskov, A.; Kern, J.; Gabdulkhakov, A.; Broser, M.; Zouni, A.; Saenger, W. *Nat. Struct. Mol. Biol.* **2009**, *16*, 334.

[5] Nugent, J. *Biochim. Biophys. Acta* **2001**, *1503*, 1.

[6] Debus, R. *Biochim. Biophys. Acta* **1992**, *1102*, 269.

[7] Diner, B.; Rappaport, F. *Annu. Rev. Plant Biol.* **2002**, *53*, 551.

[8] Barber, J. *Quart. Rev. Biophys.* **2003**, *36*, 71.

[9] McEvoy, J.; Brudvig, G. *Chem. Rev.* **2006**, *106*, 4455.

[10] Iordanova, N.; Hammes-Schiffer, S. *J. Am. Chem. Soc.* **2002**, *124*, 4848.

[11] Binstead, R.; Meyer, T. *J. Am. Chem. Soc.* **1987**, *109*, 3287.

[12] Huynh, M.; Meyer, T. *Chem. Rev.* **2007**, *107*, 5004.

[13] Biczok, L.; Linschitz, H. *J. Phys. Chem.* **1995**, *99*, 1843.

[14] Costentin, C. *Chem. Rev.* **2008**, *108*, 2145.

[15] Cukier, R. I.; Nocera, D. G. *Annu. Rev. Phys. Chem.* **1998**, *49*, 337.

[16] Sjödin, M.; Styring, S.; Wolpher, H.; Xu, Y.; Sun, L.; Hammarström, L. *J. Am. Chem. Soc.* **2005**, *127*, 3855.

[17] Shakib, F.; Hanna, G. *J. Chem. Phys.* **2014**, *141*, 044122.

[18] Petek, H.; Zhao, J. *Chem. Rev.* **2010**, *110*, 7082.

[19] Warren, J.; Tronic, T.; Mayer, J. *Chem. Rev.* **2010**, *110*, 6961.

[20] Song, N.; Gagliardi, C. J.; Binstead, R. A.; Zhang, M.-T.; Thorp, H.; Meyer, T. J. *J. Am. Chem. Soc.* **2012**, *134*, 18538.

[21] Roubelakis, M. M.; Bediako, D. K.; Dogutan, D. K.; Nocera, D. G. *Energy Environ. Sci.* **2012**, *5*, 7737.

[22] Schrauben, J. N.; Hayoun, R.; Valdez, C. N.; Braten, M.; Fridley, L.; Mayer, J. M. *Science* **2012**, *336*, 1298.

[23] Pizano, A. A.; Yang, J. L.; Nocera, D. G. *Chem. Sci.* **2012**, *3*, 2457.

[24] Cukier, R.; Nocera, D. *Annu. Rev. Phys. Chem.* **1998**, *49*, 337.

[25] Soudackov, A.; Hammes-Schiffer, S. *J. Chem. Phys.* **2000**, *113*, 2385.

[26] Rostov, I.; Hammes-Schiffer, S. *J. Chem. Phys.* **2001**, *115*, 285.

[27] Kobrak, M.; Hammes-Schiffer, S. *J. Phys. Chem. B* **2001**, *105*, 10435.

[28] Hammes-Schiffer, S.; Soudackov, A. *J. Chem. Phys.* **2008**, *112*, 14108.

[29] Hammes-Schiffer, S.; Stuchebrukhov, A. *Chem. Rev.* **2010**, *110*, 6939.

[30] Siegbahn, P. E.; Blomberg, M. *Chem. Rev.* **2010**, *110*, 7040.

[31] Cukier, R. *J. Phys. Chem.* **1996**, *100*, 15428.

[32] Soudackov, A.; Hammes-Schiffer, S. *J. Chem. Phys.* **1999**, *111*, 4672.

[33] Georgievskii, Y.; Stuchebrukhov, A. A. *J. Chem. Phys.* **2000**, *113*, 10438.

[34] Hammes-Schiffer, S. *J. Phys. Chem. Lett.* **2011**, *2*, 1410.

[35] Tully, J. C.; Preston, R. K. *J. Chem. Phys.* **1971**, *55*, 562.

[36] Preston, R. K.; Tully, J. C. *jnp* **1971**, *55*, 562.

[37] Tully, J.; Preston, R. *J. Chem. Phys.* **1990**, *93*, 1061.

[38] Tully, J. C. *Int. J. Quantum Chem.* **1991**, *25*, 299.

[39] Akimov, A. V.; Prezhdo, O. V. *Phys. Rev. Lett.* **2014**, *113*, 153003.

[40] Wang, L. J.; Trivedi, D.; Prezhdo, O. V. *J. Chem. Theory Comput.* **2014**, *10*, 3598.

[41] Sifain, A. E.; Wang, L. J.; Prezhdo, O. V. *J. Chem. Phys.* **2015**, *142*, 224102.

[42] Poulsen, J. A.; Nyman, G.; Rossky, P. J. *J. Chem. Phys.* **2003**, *119*, 12179.

[43] Wang, H.; Sun, X.; Miller, W. H. *J. Chem. Phys.* **1998**, *108*, 9726.

[44] Heller, E. J. *J. Chem. Phys.* **1976**, *75*, 1289.

[45] Jang, S.; Voth, G. A. *J. Chem. Phys.* **1999**, *111*, 2371.

[46] Craig, I. R.; Manolopoulos, D. E. *J. Chem. Phys.* **2004**, *121*, 3368.

[47] Warshel, A.; Levitt, M. *J. Mol. Biol.* **1976**, *103*, 227.

[48] Field, M. J.; Bash, P. A.; Karplus, M. *J. Comput. Chem.* **1990**, *11*, 700.

[49] Gao, J. L. *Acc. Chem. Res.* **1992**, *29*, 298.

[50] Bakowies, D.; Thiel, W. *J. Phys. Chem.* **1996**, *100*, 10580.

[51] Monard, G.; Merz, K. M. *Acc. Chem. Res.* **1999**, *32*, 904.

[52] Jono, R.; Watanabe, Y.; Shimizu, K.; Terada, T. *J. Comput. Chem.* **2010**, *31*, 1168.

[53] Li, H. Z.; Yang, W. *J. Chem. Phys.* **2007**, *126*, 114104.

[54] Seabra, G. D.; Walker, R. C.; Roitberg, A. E. *J. Phys. Chem. A* **2009**, *113*, 11938–11948.

[55] Li, H. Z.; Fajer, M.; Yang, W. *J. Chem. Phys.* **2007**, *126*, 024106.

[56] Kapral, R.; Ciccotti, G. *J. Chem. Phys.* **1999**, *110*, 8919.

[57] Shi, Q.; Geva, E. *J. Chem. Phys.* **2004**, *121*, 3393.

[58] Kapral, R. *Annu. Rev. Phys. Chem.* **2006**, *57*, 129.

[59] Gindensperger, E.; Meier, C.; Beswick, J. A. *J. Chem. Phys.* **2000**, *113*, 9369.

[60] Gindensperger, E.; Meier, C.; Beswick, J. A. *Adv. Quantum Chem.* **2004**, *47*, 331.

[61] Garaschuk, S.; Volkov, M. V. *J. Chem. Phys.* **2012**, *137*, 074115.

[62] Hazra, A.; Soudackov, A.; Hammes-Schiffer, S. *J. Phys. Chem. B* **2010**, *114*, 12319.

[63] Nachtigallova, D.; Aquino, A. J. A.; Szymczak, J. J.; Barbatti, M.; Hobza, P.; Lischka, H. *J. Phys. Chem. A* **2011**, *115*, 5247.

[64] Jiang, R.; Sibert, E. *J. Chem. Phys.* **2012**, *136*, 224104.

[65] Soudackov, A.; Hammes-Schiffer, S. *J. Phys. Chem. Lett.* **2014**, *5*, 3274.

[66] Topaler, M. S.; Allison, T. C.; Schwenke, D. W.; Truhlar, D. G. *J. Phys. Chem. A* **1998**, *102*, 1666.

[67] Hack, M. D.; Wensmann, A. M.; Truhlar, D. G.; Ben-Nun, M.; Martinez, T. J. *J. Chem. Phys.* **2001**, *115*, 1172.

[68] Fang, J. Y.; Hammes-Schiffer, S. *J. Phys. Chem. A* **1999**, *103*, 9399.

[69] Subotnik, J. E.; Shenvi, N. *J. Chem. Phys.* **2011**, *134*, 244114.

[70] Bedard-Hearn, M. J.; Larsen, R. E.; Schwartz, B. J. *J. Chem. Phys.* **2005**, *123*, 234106.

[71] Landry, B. R.; Subotnik, J. E. *J. Chem. Phys.* **2012**, *137*, 22A513.

[72] Landry, B. R.; Subotnik, J. E. *J. Chem. Phys.* **2011**, *135*, 191101.

[73] Falk, M.; Landry, B.; Subotnik, J. *J. Phys. Chem. B* **2014**, *118*, 8108.

[74] Martens, C. C.; Fang, J. *J. Chem. Phys.* **1997**, *106*, 4918.

[75] Donoso, A.; Martens, C. C. *J. Chem. Phys.* **1998**, *102*, 4291.

[76] Donoso, A.; Martens, C. C. *J. Chem. Phys.* **2000**, *112*, 3980.

[77] Donoso, A.; Kohen, D.; Martens, C. C. *J. Chem. Phys.* **2000**, *112*, 7345.

[78] Santer, M.; Manthe, U.; Stock, G. *J. Chem. Phys.* **2001**, *114*, 2001.

[79] Kapral, R.; Ciccotti, G. *J. Chem. Phys.* **1999**, *110*, 8919.

[80] Nielsen, S.; Kapral, R.; Ciccotti, G. *J. Stat. Phys.* **2000**, *101*, 225.

[81] Wan, C.; Schofield, J. *J. Chem. Phys.* **2000**, *113*, 7047.

[82] Wan, C.; Schofield, J. *J. Chem. Phys.* **2000**, *112*, 4447.

[83] MacKernan, D.; Kapral, R.; Ciccotti, G. *J. Phys.: Condens. Matter* **2002**, *14*, 9069.

[84] Hanna, G.; Kapral, R. *J. Chem. Phys.* **2005**, *122*, 244505.

[85] MacKernan, D.; Ciccotti, G.; Kapral, R. *J. Phys. Chem. B* **2008**, *112*, 424.

[86] Azzouz, H.; Borgis, D. *J. Chem. Phys.* **1993**, *98*, 7361.

[87] Hanna, G.; Kapral, R. *J. Chem. Phys.* **2008**, *128*, 164520.

[88] Hammes-Schiffer, S.; Tully, J. *J. Chem. Phys.* **1994**, *101*, 4657.

[89] Wigner, E. *Phys. Rev.* **1932**, *40*, 749.

[90] Fang, J.-Y.; Hammes-Schiffer, S. *J. Chem. Phys.* **1997**, *106*, 8442.

[91] Fang, J.-Y.; Hammes-Schiffer, S. *J. Chem. Phys.* **1997**, *107*, 8933.

[92] Fang, J.-Y.; Hammes-Schiffer, S. *J. Chem. Phys.* **1997**, *107*, 5727.

[93] Shin, S.; Metiu, H. *J. Chem. Phys.* **1995**, *102*, 9285.

[94] Moyer, B.; Meyer, T. *J. Am. Chem. Soc.* **1978**, *100*, 3601.

[95] Binstead, R.; Moyer, B.; Samuels, G.; Meyer, T. *J. Am. Chem. Soc.* **1981**, *103*, 2897.

[96] Chang, I.; Gray, H.; Winkler, J. *J. Am. Chem. Soc.* **1991**, *113*, 7056.

[97] Magnuson, A.; Berglund, H.; Korall, P.; Hammarström, L.; Åkermark, B.; Styring, S.; Sun, L. *J. Am. Chem. Soc.* **1997**, *119*, 10720.

[98] Meyer, T.; Huynh, M. *Inorg. Chem.* **2003**, *42*, 8140.

[99] Sjödin, M.; Irebo, T.; Utas, J.; Lind, J.; Merényi, G.; Åkermark, B.; Hammarström, L. *J. Am. Chem. Soc.* **2006**, *128*, 13076.

[100] Tully, J. C. *J. Chem. Phys.* **1990**, *93*, 1061.

[101] Kelly, A.; Markland, T. E. *J. Chem. Phys* **2013**, *139*, 014104.

[102] Schwartz, B. J.; Bittner, E. R.; Prezhdo, O. V.; Rossky, P. J. *J. Chem. Phys.* **1996**, *104*, 5942.

[103] Jasper, A. W.; Stechmann, S. N.; Truhlar, D. G. *J. Chem. Phys.* **2002**, *116*, 5424.

[104] Jaeger, H. M.; Fischer, S.; Prezhdo, O. V. *J. Chem. Phys.* **2012**, *137*, 22A545–1.

[105] Savéant, J.-M. *Annu. Rev. Anal. Chem.* **2014**, *7*, 537.

[106] Costentin, C.; Robert, M.; Savéant, J.-M.; Teillout, A.-L. *chem. phys. chem.* **2009**, *10*, 191.

[107] Costentin, C.; Robert, M.; Savéant, J.-M.; Teillout, A.-L. *Proc. Natl. Acad. Sci. USA* **2009**, *107*, 3367.

[108] Savéant, J.-M. *Elements of Molecular and Biomolecular Electrochemistry: An Electrochemical Approach to Electron Transfer Chemistry.*; Hoboken, NJ: Wiley., 2006.

[109] Rhile, I.; Mayer, J. *J. Am. Chem. Soc.* **2004**, *126*, 12718.

[110] Markle, T.; Mayer, J. *Angew. Chem. Int. Ed.* **2008**, *47*, 564.

[111] Marcus, R. *J. Chem. Phys* **1956**, *24*, 966.

[112] Marcus, R. *Can. J. Chem.* **1959**, *37*, 155.

[113] Marcus, R. *J. Chem. Phys* **1965**, *43*, 679.

[114] Hush, N. *J. Chem. Phys.* **1958**, *28*, 962.

[115] Hush, N. *Electrochim. Acta* **1968**, *13*, 1005.

[116] Hush, N. *J. Electroanal. Chem.* **1999**, *460*, 5.

[117] Levich, V. *Annu. Rev. Phys. Chem.* **1967**, *18*, 153.

[118] Cukier, R. *J. Phys. Chem.* **1994**, *98*, 2377.

[119] Cukier, R. *J. Phys. Chem. A* **1999**, *103*, 5989.

[120] Soudackov, A.; Hatcher, E.; Hammes-Schiffer, S. *J. Chem. Phys.* **2005**, *122*, 014505.

[121] Hammes-Schiffer, S.; Soudackov, A. *J. Phys. Chem. B* **2008**, *112*, 14108.

[122] Kretchmer, J.; Miller III, T. F. *J. Chem. Phys.* **2013**, *138*, 134109.

[123] Yamamoto, T. *J. Chem. Phys.* **1960**, *33*, 281.

[124] Ananth, N.; Miller III, T. F. *Mol. Phys.* **2012**, *110*, 1009.

[125] Craig, I. R.; Manolopoulos, D. E. *J. Chem. Phys.* **2005**, *122*.

[126] Kim, H.; Kapral, R. *J. Chem. Phys.* **2005**, *123*, 194108.

[127] Hanna, G.; Kim, H.; Kapral, R. In *Quantum Dynamics of Complex Molecular Systems*; Micha, D. A., Burghardt, I., Eds.; Springer-Verlag: Berlin, 2006.

[128] Kim, H.; Kapral, R. *J. Chem. Phys.* **2005**, *122*, 214105.

[129] Trotter, H. F. *Proc. Am. Math. Soc.* **1959**, *10*, 545.

[130] Tuckerman, M. *Statistical Mechanics: Theory and Molecular Simulation*; Oxford Graduate Texts. Oxford University Press: Oxford, 2010.